# Role of Water in Formic Acid Decomposition

**Naoko Akiya and Phillip E. Savage**
Dept. of Chemical Engineering, The University of Michigan, Ann Arbor, MI 48109

*Formic acid decomposes primarily to CO and $H_2O$ in the gas phase, but to $CO_2$ and $H_2$ in the aqueous phase. Ab-initio quantum chemical calculations were performed, using Hartree-Fock and density functional methods, to seek an explanation for this behavior. The effect of water on the two decomposition pathways and on the isomerization of formic acid was determined. The transition state structures were fully optimized and include up to two water molecules. In the absence of water, dehydration is more favorable than decarboxylation. The presence of water reduces the activation barriers for both decomposition pathways, but decarboxylation is consistently more favorable than dehydration. The water molecules actively participate in the bond-breaking and bond-forming processes in the transition state. The reduction in the activation barriers with the addition of water indicates that water acts as a homogeneous catalyst for both dehydration and decarboxylation, whereas isomerization of formic acid occurs independently of water. Water has a strong effect on the relative stability of the formic acid isomers, acid–water complexes, and transition states. The relative stability of the transition states plays an important role in determining the faster decomposition pathway.*

## Introduction

Carboxylic acids are important elements in the preparation of various commercial products, resulting in appreciable quantities of carboxylic acids in waste streams (Mishra et al., 1995). In addition, carboxylic acids are frequently observed intermediate products from the oxidation of organic wastes in both gas and aqueous phases (Thornton and Savage, 1990). Hence understanding the decomposition kinetics and mechanisms for these organic acids is important.

Decomposition of formic acid, the simplest carboxylic acid, has been studied both experimentally and theoretically. Although many mechanisms have been suggested in the literature, including free-radical chemistry, ionic chemistry, and surface catalysis, molecular elimination is considered the most important mechanism in both the gas phase (Blake and Hinshelwood, 1960; Hsu et al., 1982; Saito et al., 1984; Goddard et al., 1992; Francisco, 1992) and in the presence of water (Ruelle et al., 1986; Melius et al., 1990). It is generally agreed that the reaction network consists of two parallel pathways:

$$HCOOH \rightarrow CO_2 + H_2 \quad \text{decarboxylation} \quad (1)$$

$$HCOOH \rightarrow CO + H_2O \quad \text{dehydration.} \quad (2)$$

Several experiments on formic acid decomposition have been reported for both the gas phase (Blake and Hinshelwood, 1960; Blake et al., 1971; Hsu et al., 1982; Saito et al., 1984) and the aqueous phase (Bjerre and Sørensen, 1992; Brill et al., 1996; Yu and Savage, 1998). The gas-phase experiments show that the CO yield is substantially greater than the $CO_2$ yield, which indicates that dehydration is the primary pathway. On the other hand, the aqueous-phase experiments point to decarboxylation as the main pathway.

This difference in the selectivity in the gas phase and the aqueous phase could possibly be explained by water being a homogeneous catalyst for the decarboxylation pathway (Ruelle et al., 1986). One way to address this issue of water's potential catalytic role is theoretical investigation. Several *ab initio* quantum chemical calculations for formic acid and its decomposition have been reported (Ruelle et al., 1986; Ruelle, 1987; Melius et al., 1990; Goddard et al., 1992; Francisco, 1992; Kumaresan and Kolandaivel, 1995). Francisco (1992) and Goddard et al. (1992) studied the gas-phase reaction in the absence of water and showed that the activation energy for decarboxylation was slightly higher than that for dehydration, which is consistent with the higher yield of CO observed in gas-phase experiments.

Ruelle et al. (1986) also studied the gas-phase reaction and suggested that the decarboxylation step in the gas phase is catalyzed by water produced in the dehydration step. They showed that including a single water molecule in the decarboxylation transition-state structure substantially reduced the

Correspondence concerning this article should be addressed to P. E. Savage.

activation barrier for decarboxylation. The quantitative reliability of their calculation has been questioned, however, since some of the transition states they found for formic acid decomposition may be flawed (Francisco, 1992).

Melius et al. (1990) studied the effect of water at high density as a solvating agent and catalyst for the water gas shift reaction ($CO + H_2O = CO_2 + H_2$), which they took to proceed through a formic acid intermediate. They included up to two water molecules in the transition states for dehydration and decarboxylation and demonstrated that both pathways are catalyzed by water. They found that decarboxylation is the favored pathway for all cases considered, even in the absence of water, which is inconsistent with the data obtained from gas-phase experiments (Blake and Hinshelwood, 1960; Blake et al., 1971; Hsu et al., 1982; Saito et al., 1984) and the calculations by Francisco (1992) and Goddard et al. (1992). Since their focus was on the water gas shift reaction rather than the formic acid intermediate, Melius et al. (1990) did not make any distinction between the different isomers of formic acid. Accounting for the relative stability of the *cis* and *trans* isomers could affect the activation barriers and hence the selectivity. Furthermore, Melius et al. did not optimize the structure of formic acid stabilized by water molecules to calculate the energy of the hydrated formic acid molecules. Instead, they determined the total energy of the hydrated formic acid as the sum of the energies calculated separately for formic acid and water molecules. Since formic acid and water interact by forming hydrogen bonds, it is unlikely that the total energy of the hydrated formic acid would simply be the sum of the energies of its individual components.

The recent appearance of new experimental data for formic acid decomposition in an aqueous phase (Brill et al., 1996; Yu and Savage, 1998) and the inability of any of the previous theoretical studies to explain fully all of the available experimental data for formic acid decomposition motivated the present study of the effect of water on formic acid decomposition. We considered three scenarios: formic acid and the decomposition transition states stabilized with (1) zero, (2) one, and (3) two water molecules. Case (1) represents the gas-phase decomposition, and cases (2) and (3) the hydrothermal decomposition. The present work differs from previous theoretical studies in that the formic acid isomers are treated as distinct species, the effect of their relative stability on the activation barriers is considered, and hydrated formic acid isomers are optimized individually to calculate their energies more accurately.

## Computational Methods

*Ab-initio* calculations were performed with Gaussian 94 revision B.3 (Frisch et al., 1995). The equilibrium geometries of reactants and products were fully optimized with the Berny optimization method (Schlegel, 1982). We used the synchronous transit-guided quasi-Newton method (Peng et al., 1996; Peng and Schlegel, 1993) to locate the transition state structures. Frequency calculations using the analytic second derivatives were performed to compute various thermodynamic quantities as well as the thermal energy corrections to the total electronic energy. We performed the frequency calculations at a temperature ($T$) and pressures ($p$) representative of the experimental reaction conditions: $T = 700$ K, $p = 1$ atm (gas phase)/300 atm (hydrothermal).

Geometry optimizations and frequency calculations were performed with Hartree-Fock theory and the 3-21G(d,p) basis set. We performed single-point energy calculations on the optimized geometry, using Becke's three-parameter hybrid method (Miehlich et al., 1989; Becke, 1993) with the Lee, Yang, and Parr correlation functional (Lee et al., 1988) and the 6-311 + G(2d,p) basis set. This combination of the theory and basis set was chosen based on the results from a study conducted by Foresman and Frisch (1996), which compared various model chemistries with experimental data. Although all the structures are singlets, bond dissociations occur at transition states, which suggests that the unrestricted method may be required to describe them properly. We conducted several test calculations using both the restricted and unrestricted methods. The results were identical for both methods, even when the HOMO and LUMO were mixed to destroy the spin symmetry for the initial guess of the Hartree-Fock wavefunction. Therefore, all the results reported in this article are based on calculations using the restricted method. All of the calculations were conducted for molecules in a medium of zero dielectric constant. The dielectric constant of water at 700 K and 300 atm is about 3.9 (Haar et al., 1984), however, so we performed several calculations using the self-consistent reaction field methods for reactions in solution and observed no significant change in the numerical results.

## Results and Discussion

### *Molecular structures*

Tables 1 and 2 summarize the optimized and experimental ground-state geometries of the *trans* and *cis* formic acid iso-

**Table 1 Optimized and Experimental Ground-State Geometries for Formic Acid Isomers in the Absence of Water ($H_1CO_1O_2H_2$) (Å, deg)**

| Coordinate | *Trans* (Calc.) | *Trans* (Exp.)* | *Cis* (Calc.) | *Cis* (Exp.)** |
|---|---|---|---|---|
| $r(O_1 = C)$ | 1.198 | $1.202 \pm 0.010$ | 1.192 | $1.1945 \pm 0.0031$ |
| $r(C - H_1)$ | 1.074 | $1.097 \pm 0.005$ | 1.081 | $1.1050 \pm 0.0043$ |
| $r(C - O_2)$ | 1.354 | $1.343 \pm 0.010$ | 1.358 | $1.3520 \pm 0.0028$ |
| $r(O_2 - H_2)$ | 0.945 | $0.972 \pm 0.005$ | 0.940 | $0.9555 \pm 0.0053$ |
| $\angle(O_1 = C - O_2)$ | 124.6 | $124.9 \pm 1$ | 122.3 | $122.12 \pm 0.37$ |
| $\angle(H_1 - C - O_2)$ | 109.4 | $111.0 \pm 2^{\dagger}$ | 113.8 | $114.64 \pm 0.56$ |
| $\angle(H_1 - C = O_1)$ | 126.0 | $124.1 \pm 2$ | 123.9 | $123.23 \pm 0.58$ |
| $\angle(C - O_2 - H_2)$ | 111.8 | $106.2 \pm 1$ | 113.3 | $109.68 \pm 0.44$ |
| $\angle(H_1 - C - O_2 - H_2)$ | 180.0 | 180.0 | 0.0 | 0.0 |

*Kwei and Curl (1960).
**Bjarnov and Hocking (1978).
†Estimated uncertainty. This angle was not given in the original reference.

Table 2. Optimized and Experimental Ground-State Geometries for Decomposition Products (Å, deg)

| Species | Coordinate | Calc. | Exp. |
|---|---|---|---|
| CO | $r$(C-O) | 1.129 | 1.128* |
| $CO_2$ | $r$(C-O) | 1.156 | 1.160** |
| $H_2$ | $r$(H-H) | 0.737 | 0.739† |
| $H_2O$ | $r$(O-H) | 0.941 | 0.958* |
| | ∠(H-O-H) | 105.8 | 104.5* |

*Francisco (1992).
**Graner et al. (1986).
†Jeppesen (1933).

mers and their decomposition products. Experimental uncertainties are given where they are available. Despite the low level of theory and small basis set used for optimization, Tables 1 and 2 show that the predicted and experimental geometries are consistent.

Visualization of the molecular structures provides helpful insight into the reaction mechanism. Figures 1 and 2 show the structures of the formic acid isomers and the transition states for the two decomposition pathways in the absence of water. These and all the molecular structures were constructed using the visualization program Xmol, developed by the Minnesota Supercomputer Center (Xmol, 1993). Xmol displays small solid rectangles between atoms that it considers to be close enough to be chemically bonded. We added dashed lines between some atoms to enhance the clarity of the transition-state structures. It is apparent in Figures 1 and 2 that formic acid must be in the appropriate configuration for each decomposition pathway to proceed. In other words, it is the *trans* isomer of formic acid (Figure 1a), in which the two hydrogen atoms are on opposite sides of the CO bond, which leads to the dehydration transition-state structure (Figure 1b). In this transition state, formic acid is distorted such that the hydrogen atom bonded to the carbon atom approaches the hydroxyl group, which foreshadows the eventual cleavage of the CH bond and formation of water and carbon monoxide molecules. Similarly, the *cis* isomer (Figure 2a), in which the two hydrogen atoms are on the same side of the

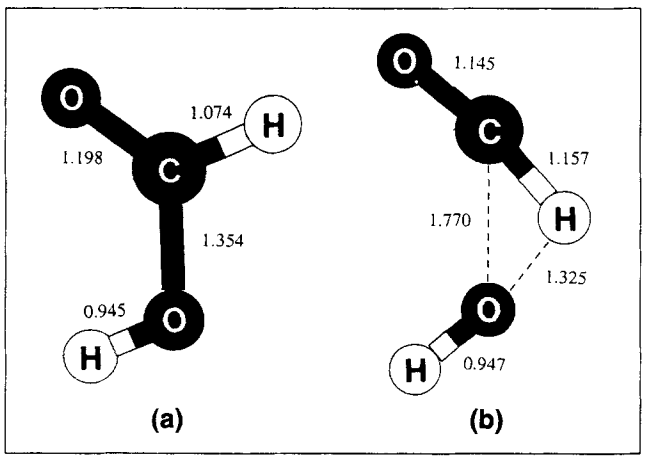


**Figure 1. Predicted structure for: (a) *trans* formic acid in the absence of water; (b) dehydration transition state connecting *trans* formic acid with $CO+H_2O$.**

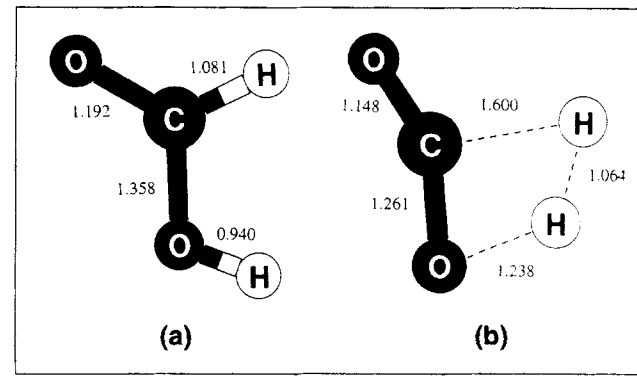


**Figure 2. Predicted structure for: (a) *cis* formic acid in the absence of water; (b) decarboxylation transition state connecting *cis* formic acid with $CO_2+H_2$.**

CO bond, is the precursor for the decarboxylation transition state structure (Figure 2b). In this case, the two hydrogen atoms approach each other, suggesting the formation of carbon dioxide and hydrogen molecules.

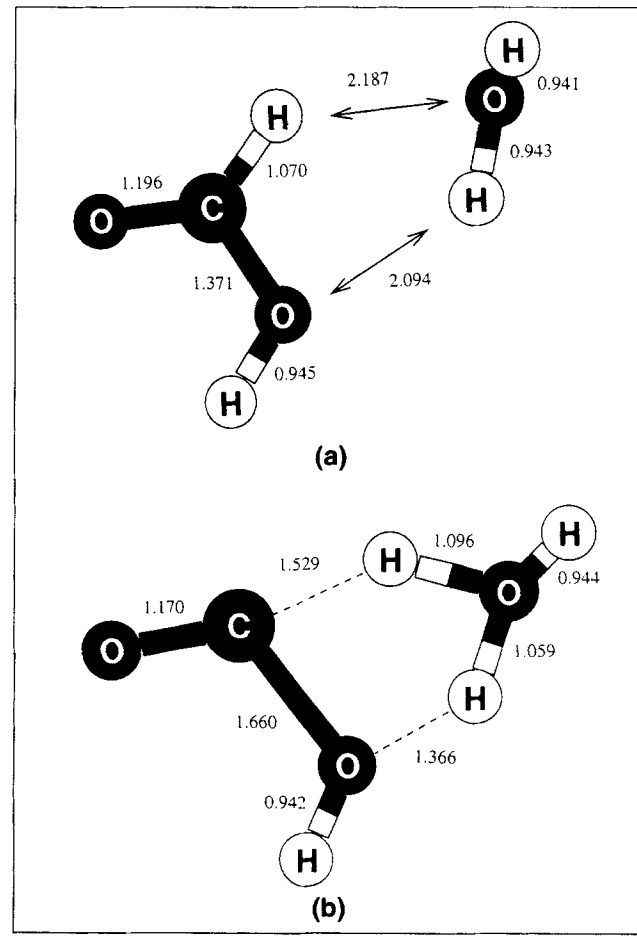


**Figure 3. Predicted structure for: (a) *trans* formic acid with one water molecule (Configuration A); (b) dehydration transition state connecting the *trans* formic acid plus $H_2O$ with $CO+2H_2O$.**

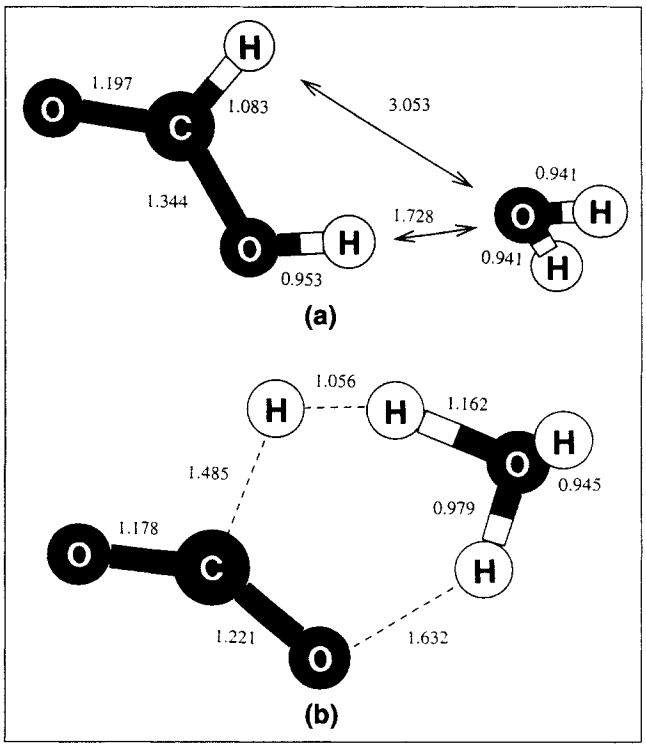


**Figure 4. Predicted structure for: (a) *cis* formic acid with one water molecule (Configuration A); (b) decarboxylation transition state connecting the *cis* formic acid plus $H_2O$ with $CO_2 + H_2 + H_2O$.**

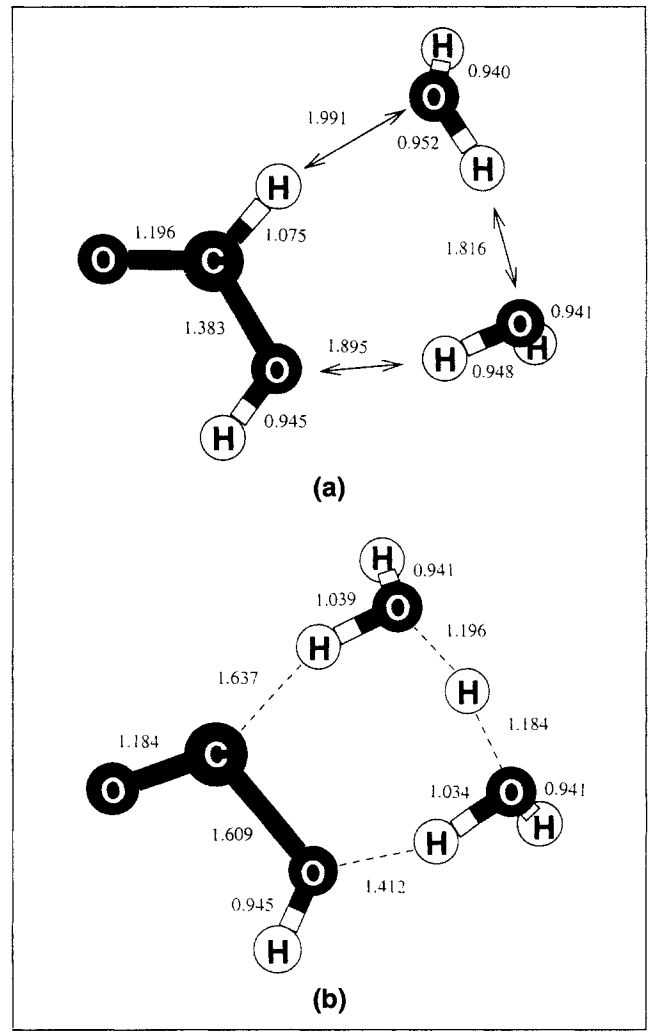


**Figure 5. Predicted structure for: (a) *trans* formic acid with two water molecules (Configuration A); (b) dehydration transition state connecting the *trans* formic acid plus $2H_2O$ with $CO + 3H_2O$.**

This type of isomer-specific selectivity for different decomposition pathways seen in absence of water is also observed for water-assisted decomposition. Figures 3 and 4 show the optimized formic acid isomers and transition-state structures stabilized with one water molecule, which was initially placed on the side of formic acid opposite the carbonyl oxygen atom. Although the net consumption of water molecules in these reactions is zero, the identity of the atoms in that water molecule is not conserved as a result of water's participation in the bond-breaking and bond-forming processes. In the case of dehydration (Figure 3), one hydrogen atom in the water molecule joins the hydroxyl group in the *trans* formic acid to form a new water molecule, while the hydrogen bonded to carbon in the acid breaks off to regenerate a water molecule. Similarly, in the case of decarboxylation (Figure 4), one hydrogen atom from the water molecule joins the hydrogen atom bonded to the carbon atom to form a hydrogen molecule, while the hydrogen atom from the acid hydroxyl group regenerates the water molecule. Figures 5 and 6 show that the decomposition reactions are assisted by two water molecules in a manner similar to that when only one water molecule is present.

### *Relative energies for the decomposition pathways*

Table 3 presents the total energies of reactants, products, and transition states involved in formic acid decomposition. The total energy is the sum of the electronic energy and the thermal energy correction, which accounts for the energy arising from nuclear motion at a specified temperature and pressure. Based on this information, the heats of reaction and activation energies were calculated for formic acid decomposition. Since the total energy is temperature dependent, the activation energies are also temperature dependent, that is, they are not Arrhenius activation energies. The relative energies are presented in Figures 7 through 9. Figure 7 is the energy diagram for the gas-phase reactions, constructed with the *trans* formic acid isomer as the reference point. Figures 8 and 9 are the energy diagrams for the water-assisted pathways, with the *cis* formic acid isomer as the reference point.

If the activation energies were to be calculated as the difference between the total energies of the transition state and the formic acid isomer that directly transforms to that transition state structure (i.e., the decarboxylation transition state and the *cis* isomer), decarboxylation would have a lower activation barrier than dehydration in all cases. Such a result, however, would be inconsistent with the experimental observation that dehydration is the favored pathway in the absence of water. This potential inconsistency is circumvented, however, by recognizing that the relative stability of the two formic

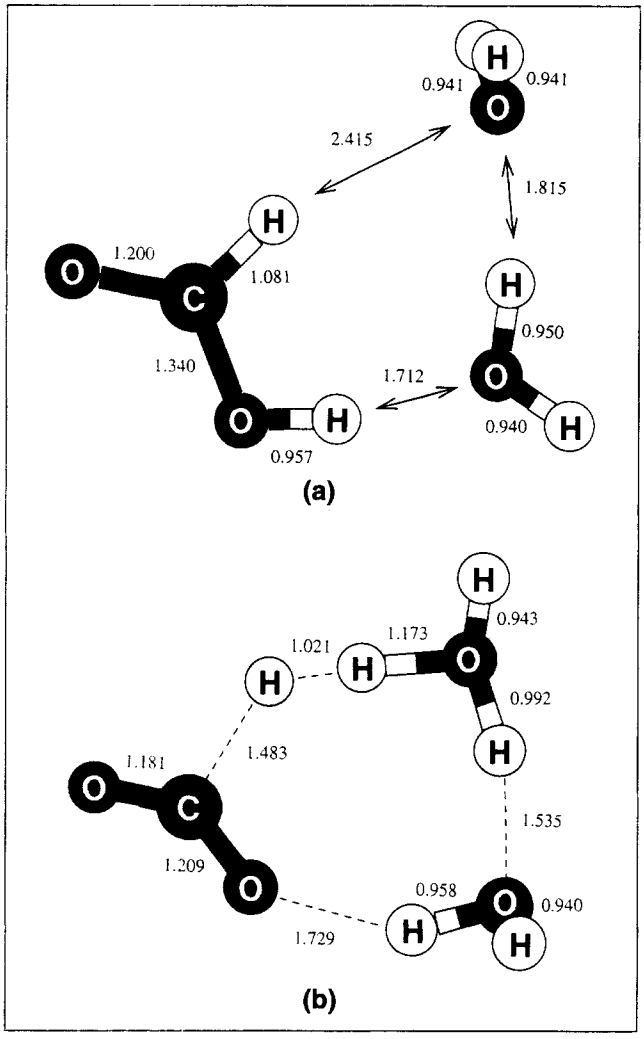


**Figure 6. Predicted structure for: (a) *cis* formic acid with two water molecules (Configuration A); (b) decarboxylation transition state connecting the *cis* formic acid plus $2H_2O$ with $CO_2 + H_2 + 2H_2O$.**

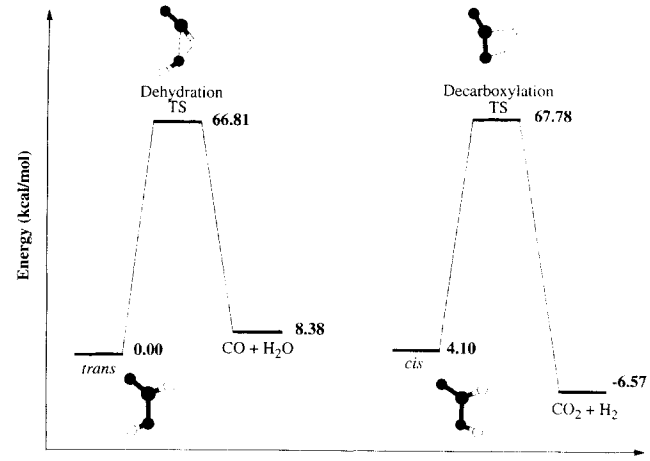


**Figure 7. Energy diagram for formic acid decomposition and isomerization in the absence of water.**

acid isomers becomes an important factor in determining which decomposition pathway is more favorable. For example, Figure 7 shows that the *trans* isomer is 4.1 kcal/mol more stable than the *cis* isomer in the absence of water. This energy difference is within 0.1 kcal/mol of previous experimental determinations (Lide, 1966; Hocking, 1976) and electronic structure calculations (Francisco, 1992; Goddard et al., 1992).

**Table 3. Total Energies (Hartrees) for Reactants, Products, and Transition-State Structures for Formic Acid Decomposition**

| Structure | $n=0$ | $n=1$ | $n=2$ |
|---|---|---|---|
| $CO+(n+1)H_2O$ | −189.77140 | −266.20147 | −342.63152 |
| Dehydration TS | −189.67828 | −266.13479 | −342.58408 |
| *trans*-$HCOOH-nH_2O$ | −189.78475 | −266.20980 | −342.64486 |
| *cis*-$HCOOH-nH_2O$ | −189.77822 | −266.21426 | −342.64665 |
| Decarboxylation TS | −189.67674 | −266.14677 | −342.59139 |
| $CO_2+H_2+nH_2O$ | −189.79522 | −266.22528 | −342.65533 |

Since the *trans* isomer is more stable, most of the formic acid will be in that form. For decarboxylation to take place, *trans* formic acid must first isomerize to *cis* formic acid before the appropriate transition-state structure can be formed. Thus, in the absence of water, the effective activation energy for decarboxylation is 67.8 kcal/mol (63.68 + 4.10), which exceeds the activation energy for dehydration (66.8 kcal/mol). This result is consistent with the experimental observation that dehydration is the favored pathway in the absence of water. Note that the result of the *ab-initio* calculations agree with the selectivity observed experimentally only when one accounts for the relative stability of the formic acid isomers.

The addition of one and two water molecules to formic acid and the transition-state structure lowers the activation barriers for both dehydration and decarboxylation, as shown in Figures 8 and 9. Water acts as a catalyst for both decomposition pathways by altering the transition states, as shown in the b sections of Figures 3–6. Note, however, that the decarboxylation transition state is lower in energy than the de-

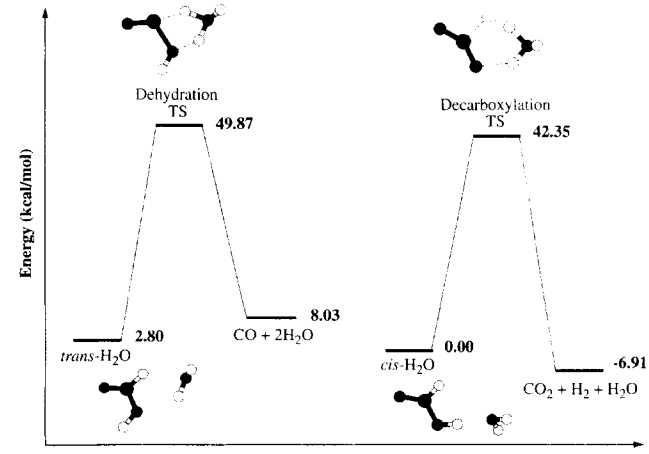


**Figure 8. Energy diagram for formic acid decomposition assisted with one water molecule.**

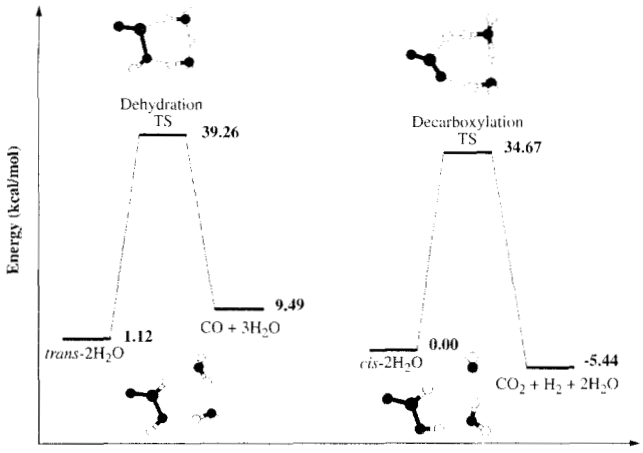


**Figure 9. Energy diagram for formic acid decomposition assisted with two water molecules.**

hydration transition state for both water-assisted scenarios, which indicates that decarboxylation is the preferred decomposition path in the presence of water. This trend is consistent with the experimental observation that decarboxylation is the main pathway for hydrothermal decomposition of formic acid (Brill et al., 1996; Yu and Savage, 1998).

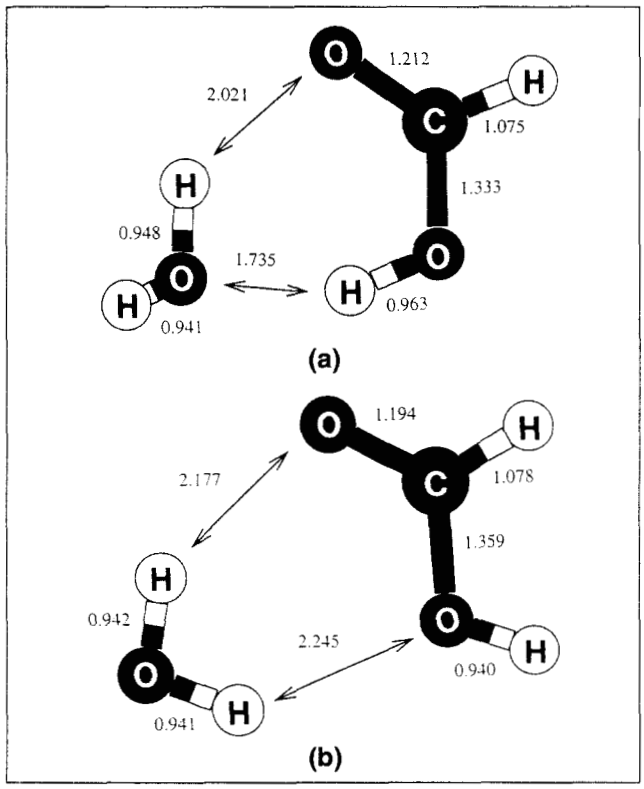


**Figure 10. Predicted structure for: (a) *trans* formic acid with one water molecule (Configuration B); (b) *cis* formic acid with one water molecule (Configuration B).**

The only configurations of formic acid–water complexes considered thus far are those in the a sections of Figures 3–6, which give rise to the transition states that lead to the dehydration and decarboxylation products. We refer to these reactive configurations as Configuration A in this section. We recognize, of course, that a formic acid molecule can interact with water molecules in a variety of ways in addition to the configurations considered up to this point. It is possible that some other formic acid–water configuration has a lower energy, in which case the effective activation energies for formic acid decomposition need to be calculated with respect to this lower energy complex. Therefore, alternative formic acid–water complexes that include one and two water molecules were optimized, and they appear in Figures 10 and 11. In these complexes, termed Configuration B, the water molecules are placed facing the CO bond of formic acid, whereas in Configuration A the water molecules are positioned away from the CO bond.

The energies of all the configurations of mono- and dihydrated formic acid isomers considered in this study are shown

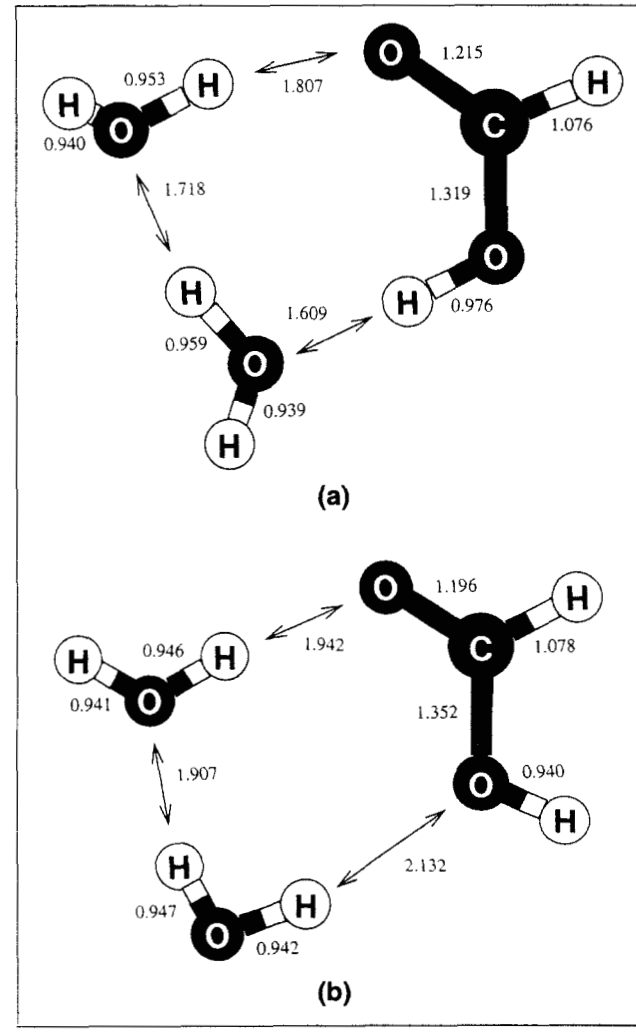


**Figure 11. Predicted structure for: (a) *trans* formic acid with two water molecules (Configuration B); (b) *cis* formic acid with two water molecules (Configuration B).**

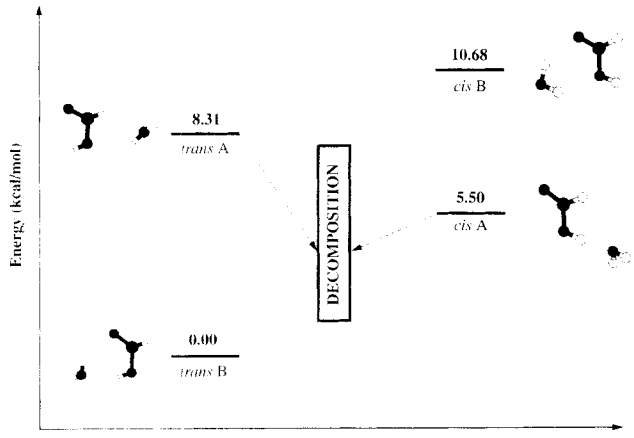


**Figure 12. Energy diagram of all the configurations of the monohydrated formic acid isomers considered in this study.**

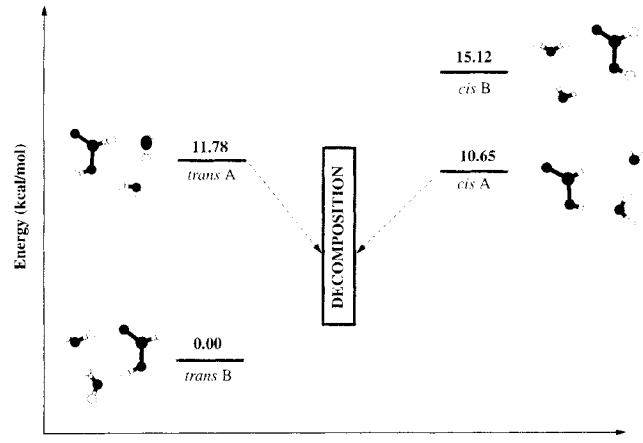


**Figure 13. Energy diagram of all the configurations of the dihydrated formic acid isomers considered in this study.**

in Figures 12 and 13, respectively. Note that in the presence of both one and two water molecules, the most stable formic acid–water complex is the *trans* (B) configuration. Since the majority of the formic acid molecules in water will be in the *trans* (B) configuration, we must account for the energy difference that arises when the *trans* (B) formic acid–water complex converts to either of the reactive formic acid–water complexes (the *trans* (A) or *cis* (A)) when calculating the effective activation energies.

Table 4 summarizes the activation energies for the decomposition pathways calculated relative to the most stable reactant, *trans* formic acid in the gas phase ($n = 0$) and *trans* (B) formic acid–water complex for the water-assisted pathways ($n = 1,2$), and compares them with the activation energies from previous studies. Experimental uncertainty is available only for the activation energy reported by Yu and Savage (1998). The gas-phase activation energies determined in this study are in good agreement with both experimental data and other theoretical studies. The activation energies for water-assisted decomposition obtained in this study are roughly 10 to 20 kcal/mol higher than those reported by Melius et al. (1990). This difference is attributed in part to our accounting for the hydrogen bonding that stabilizes the hydrated formic acid complexes and leads to the lower energy formic acid–water configurations. For their energy calculations, Melius et al. used the formic acid and water molecule(s) at infinite separation as the reference state, which corresponds to a dilute gas-phase mixture. Since the transition states cal-

**Table 4. Comparison of Activation Energies with Previous Studies (kcal/mol)**

| Reaction | This Study | Previous Study | Source |
|---|---|---|---|
| Dehydration ($n = 0$) | 66.8 | 60.5 | Experimental; Blake et al. (1971) |
| | | 62–65 | RRKM calculations; Hsu et al. (1982) |
| | | 67.1 | *Ab-initio* calculations; Ruelle et al. (1986) |
| | | 70.1 | *Ab-initio* calculations; Melius et al. (1990) |
| | | 63.0 | *Ab-initio* calculations; Francisco (1992) |
| | | 68 | *Ab-initio* calculations; Goddard et al. (1992) |
| Decarboxylation ($n = 0$) | 67.8 | 65–68 | RRKM calculations; Hsu et al. (1982) |
| | | 64.9 | *Ab-initio* calculations; Melius et al. (1990) |
| | | 65.2 | *Ab-initio* calculations; Francisco (1992) |
| | | 71 | *Ab-initio* calculations; Goddard et al. (1992) |
| Dehydration ($n = 1$) | 55.4 | 44.0 | *Ab-initio* calculations; Melius et al. (1990) |
| Decarboxylation ($n = ?$) | | 25.3 | Experimental; Brill et al. (1996) |
| | | $33.6 \pm 17.2$ | Experimental; Yu and Savage (1998) |
| Decarboxylation ($n = 1$) | 47.9 | 48.7 | *Ab-initio* calculations; Ruelle et al. (1986) |
| | | 37.3 | *Ab-initio* calculations; Melius et al. (1990) |
| Dehydration ($n = 2$) | 49.9 | 27.7 | *Ab-initio* calculations; Melius et al. (1990) |
| Decarboxylation ($n = 2$) | 45.3 | 21.5 | *Ab-initio* calculations; Melius et al. (1990) |
| Isomerization ($n = 0$) | 10.9 | 10.9 | Experimental; Miyazawa and Pitzer (1959) |
| | | 13.8 | Experimental; Hocking (1976) |
| | | 11.7 | *Ab-initio* calculations; Francisco (1992) |
| | | 12 | *Ab-initio* calculations; Goddard et al. (1992) |
| Isomerization ($n = 1$) | 12.0 | | |

culated in this study and by Melius et al. (1990) appear to be comparable, the activation barriers become greater when we account for the greater stability of the formic acid–water complexes.

### *Isomerization*

This change in relative stability of the isomers with the position of the water molecule formed the basis for investigating the possibility of isomerization, in the presence of one water molecule, occurring between the most stable forms of the hydrated formic acid isomers, namely *cis* (A) and *trans* (B) acid–water dimers. In the absence of water, formic acid isomerization occurs by internal rotation of the hydroxyl group about the CO bond. Formic acid stabilized by water could possibly isomerize by a different mechanism, since the water molecules surrounding formic acid may hinder the internal rotation. Figure 14 shows the transition state structures for isomerization both in the absence and in the presence of one water molecule. The similarity in the formic acid portion of the two structures suggests that even in the presence of water, isomerization occurs via internal rotation of the hydroxyl group about the CO bond and that the water molecule merely responds to that rotational movement. Indeed, further analysis showed that as the OH bond rotates, the oxygen atom of the water molecule diligently follows the hydrogen atom of the hydroxyl group. The activation energies for isomerization from *trans* to *cis* formic acid in the absence of water (10.9 kcal/mol) and in the presence of one water molecule (12.0 kcal/mol) appear in Table 4 along with those reported in previous studies. The similarity in these activation energies confirms that formic acid isomerization is neither catalyzed nor hindered by the presence of a water molecule. The predicted activation energy relative to the *trans* isomer in the absence of water is in agreement with both the experimental data and other theoretical studies.

### *Rate constants*

Rate constants for elementary reactions can be determined from transition-state theory (Laidler, 1987). We will treat all reactions in this study as being nominally unimolecular. This approach is reasonable because the optimized formic acid–water complexes are lower in energy than the sum of the energies of their individual components and they can be viewed as single molecular entities. For a unimolecular reaction, the transition-state theory rate constant, $k$, is expressed as

$$k = \left(\frac{k_B T}{h}\right)\left(\frac{q_{TS}}{q_r}\right)\exp\left(-\frac{E_0}{RT}\right), \tag{3}$$

where $k_B$ is Boltzmann's constant, $h$ is Planck's constant, $q_{TS}$ and $q_r$ are the partition functions for the transition state and the reactant, respectively, and $E_0$ is the threshold energy. The threshold energy is a hypothetical activation energy at absolute zero (Laidler, 1987) and is calculated by taking the difference between the total electronic energies of the reactant and the transition-state species, corrected with the zero-point vibrational energy. The values of the partition functions are determined as part of the frequency calculation in Gaussian 94, from statistical mechanical expressions for an ideal gas in the canonical ensemble. All the calculations were done at the temperature of 700 K.

Since formic acid decomposition, with or without water, involves proton transfer, quantum mechanical tunneling may have a significant effect on the rate constants. Tunneling corrections were estimated for each reaction using the high-temperature asymptotic form (Shavitt, 1959) of the tunneling correction factor derived for the Eckart barrier (Johnston, 1966). The range of the estimated correction factors was between 1.3 and 2.5. The presence of water reduced the effect of tunneling. In addition, the effect of tunneling was consistently greater for decarboxylation than dehydration, with or without water.

Since transition-state theory applies strictly to elementary reaction steps, each step in the decomposition pathways must be considered explicitly. Therefore, we calculated the rate constants for decarboxylation and dehydration by taking the reactants to be the configurations of formic acid isomers, with or without water, that lead directly to decarboxylation and dehydration transition states, respectively. Note that this configuration is not necessarily the most stable configuration. Table 5 shows the preexponential factors, which include the tunneling corrections. Table 6 shows the threshold energies. The rate constants are calculated from the preexponential factors and the threshold energies, and they are listed in Table 7.

Table 5 shows that in the absence of water ($n = 0$) all the preexponential terms are nearly $10^{13}$ $s^{-1}$, as expected for a unimolecular reaction. For the water-assisted decomposition pathways ($n = 1, 2$) the preexponential factors are one to two orders of magnitude smaller, which is consistent with the in-

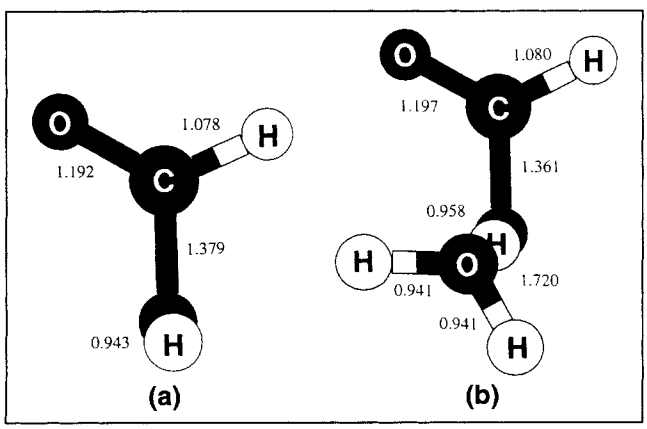


**Figure 14. Predicted structure for: (a) isomerization transition state connecting *trans* and *cis* formic acids; (b) isomerization transition state connecting *trans* formic acid + $H_2O$ (B) and *cis* formic acid + $H_2O$ (A).**

**Table 5. $Log_{10}$ of Preexponential Term at 700 K ($s^{-1}$)**

| Reaction | $n = 0$ | $n = 1$ | $n = 2$ |
|---|---|---|---|
| *trans*-HCOOH $- n H_2O \rightarrow CO + (n+1)H_2O$ | 13.8 | 12.0 | 11.6 |
| *cis*-HCOOH $- n H_2O \rightarrow CO_2 + H_2 + n H_2O$ | 13.6 | 11.4 | 12.1 |
| *trans*-HCOOH $- n H_2O \rightarrow$ *cis*-HCOOH $- n H_2O$ | 13.1 | 14.1 | — |
| *cis*-HCOOH $- n H_2O \rightarrow$ *trans*-HCOOH $- n H_2O$ | 13.0 | 12.9 | — |

**Table 6. Threshold Energies (kcal/mol)**

| Reaction | $n=0$ | $n=1$ | $n=2$ |
|---|---|---|---|
| *trans*-HCOOH $- n\mathrm{H_2O} \rightarrow \mathrm{CO} + (n+1)\mathrm{H_2O}$ | 65.9 | 48.5 | 40.0 |
| *cis*-HCOOH $- n\mathrm{H_2O} \rightarrow \mathrm{CO_2} + \mathrm{H_2} + n\mathrm{H_2O}$ | 63.5 | 44.2 | 36.3 |
| *trans*-HCOOH $- n\mathrm{H_2O} \rightarrow$ *cis*-HCOOH $- n\mathrm{H_2O}$ | 11.5 | 11.9 | — |
| *cis*-HCOOH $- n\mathrm{H_2O} \rightarrow$ *trans*-HCOOH $- n\mathrm{H_2O}$ | 7.5 | 7.5 | — |

creasing complexity of the reactions. On the other hand, both the preexponential factors and the threshold energies for isomerization in the presence and absence of water are all about the same, which is consistent with water being largely a spectator during formic acid isomerization.

The rate constants reported in Table 7 agree with the experimentally measured rate constants. The high-temperature rate expression for unimolecular dehydration in the gas phase reported by Blake et al. (1971) gives $3.25\times10^{-7}$ s$^{-1}$ at 700 K, which is similar to the dehydration rate constant of $2.03\times10^{-7}$ s$^{-1}$ calculated in this study. The first-order rate constants at 700 K of 0.894 s$^{-1}$ and 0.630 s$^{-1}$ can be calculated from experimental results reported by Brill et al. (1996) and Yu and Savage (1998), respectively, for hydrothermal decomposition of formic acid. These experimental first-order rate constants for hydrothermal decomposition fall between the predicted rate constants of 0.00438 s$^{-1}$ and 5.27 s$^{-1}$ for decarboxylation assisted with one and two water molecules, respectively.

### *Product ratios*

Having determined the kinetics of the decomposition and isomerization paths, we can now calculate the ratio of product yields as a ratio of reaction rates. The gas-phase decomposition pathways are given below:

$$\begin{array}{ccc} \textit{cis}\text{-HCOOH} & \xrightarrow{k_a} & \mathrm{CO_2} + \mathrm{H_2} \\ k_b \;\updownarrow & & \updownarrow\; k_{-b} \\ \textit{trans}\text{-HCOOH} & \xrightarrow{k_c} & \mathrm{CO} + \mathrm{H_2O} \end{array}$$

The ratio of the yield of CO relative to the yield of $CO_2$ is given by

$$\frac{\mathrm{CO}}{\mathrm{CO_2}} = \frac{r_{\mathrm{CO}}}{r_{\mathrm{CO_2}}} = \frac{k_c[trans]}{k_a[cis]}. \tag{4}$$

Table 7 shows that the forward and reverse rate constants for isomerization are much larger than those for decomposition. Thus, we can take the isomerization step to be in a quasi-equilibrium state and thereby equate the ratio of the concentrations of *cis* and *trans* formic acid with the isomerization equilibrium constant:

$$\frac{\mathrm{CO}}{\mathrm{CO_2}} \cong \frac{k_c}{k_a K_b} \tag{5}$$

where $K_b$ is the equilibrium constant for isomerization, $k_b/k_{-b}$. Substituting the numerical values of the rate constants reported in Table 7 for $n=0$ into Eq. 5 gives CO:$CO_2$ $\cong$ 5:1. The order of magnitude of this ratio is consistent with the ratio of 10:1 measured experimentally by Blake et al. (1971) for the gas-phase decomposition of formic acid.

The elementary processes involved in formic acid decomposition in the presence of water are outlined below:

$$\begin{array}{ccc} \textit{cis}\text{-HCOOH (A)} & \xrightarrow{k_a} & \mathrm{CO_2} + \mathrm{H_2} + \mathrm{H_2O} \\ K_b \;\updownarrow & & \\ \textit{trans}\text{-HCOOH (B)} & & \\ K_c \;\updownarrow & & \\ \textit{trans}\text{-HCOOH (A)} & \xrightarrow{k_d} & \mathrm{CO} + 2\mathrm{H_2O} \end{array}$$

The situation is more complex when a water molecule is present because isomerization is now modeled as a two-step process that involves a change in the position of the water molecule relative to *trans* formic acid, in addition to the isomerization itself. Recognizing that interconversion of the different formic acid–water dimers is rapid relative to decomposition, and using the same approach outlined for the gas-phase reactions, we calculate the $CO_2$/CO ratio by the following expression:

$$\frac{\mathrm{CO_2}}{\mathrm{CO}} = \frac{k_a K_b}{K_c k_d}, \tag{6}$$

where $K_b$ is the equilibrium constant for isomerization, and $K_c$ is the equilibrium constant for the interconversion of the two *trans* formic acid–water dimers, A and B. The $n=1$ column in Table 7 provides the values of $k_a$, $k_d$, and $K_b$, which is the ratio of the forward and reverse rate constants for isomerization. Rate constants are not available to calculate $K_c$, however, since the interconversion of the *trans* formic acid–water dimers is not a true chemical reaction. Rather, the process involves movement of the water molecule from one side of formic acid to the other side. We determined $K_c$ from the difference between the Gibbs free energies of *trans*

**Table 7. Rate Constants at 700 K (s$^{-1}$)**

| Reaction | $n=0$ | $n=1$ | $n=2$ |
|---|---|---|---|
| *trans*-HCOOH $- n\mathrm{H_2O} \rightarrow \mathrm{CO} + (n+1)\mathrm{H_2O}$ | $2.03\times10^{-7}$ | $7.57\times10^{-4}$ | $1.44\times10^{-1}$ |
| *cis*-HCOOH $- n\mathrm{H_2O} \rightarrow \mathrm{CO_2} + \mathrm{H_2} + n\mathrm{H_2O}$ | $5.63\times10^{-7}$ | $4.38\times10^{-3}$ | $5.27\times10^{0}$ |
| *trans*-HCOOH $- n\mathrm{H_2O} \rightarrow$ *cis*-HCOOH $- n\mathrm{H_2O}$ | $3.10\times10^{9}$ | $2.39\times10^{10}$ | — |
| *cis*-HCOOH $- n\mathrm{H_2O} \rightarrow$ *trans*-HCOOH $- n\mathrm{H_2O}$ | $4.35\times10^{10}$ | $3.43\times10^{10}$ | — |

(A) and *trans* (B) formic acid–water dimers, whose values are determined from frequency calculations at 700 K and 300 atm:

$$K = \exp\left(-\frac{\Delta G}{RT}\right). \tag{7}$$

The change in free energy for interconversion of the *trans* formic acid–water dimers is 6.48 kcal/mol, so the value of $K_c$ is $9.47\times10^{-3}$. Based on this equilibrium constant and the rate constants in Table 7, Eq. 6 gives $CO_2$:CO $\cong$ 425:1. The order of magnitude of this result is consistent with the average $CO_2$/CO ratio of 121:1 measured experimentally by Yu and Savage (1998) for hydrothermal decomposition at a temperature of 380°C and pressures ranging from 178 to 303 atm.

## Conclusions

The two decomposition pathways, decarboxylation and dehydration, and the isomerization of formic acid in the presence of water were studied by means of *ab initio* quantum chemical calculations. The predicted activation energies for dehydration and decarboxylation in the absence of water are 66.8 and 67.8 kcal/mol, respectively. These values are in agreement with both the data from gas-phase experiments and the values reported in previous *ab-initio* studies. The activation energies for dehydration and decarboxylation with one water molecule are 55.4 and 47.9 kcal/mol, respectively, and with two molecules are 49.9 and 45.3 kcal/mol, respectively.

The reduction in the activation energies with the addition of water suggests that water behaves as a homogeneous catalyst for both dehydration and decarboxylation, whereas isomerization occurs independently of water. Although both decomposition pathways are water-assisted, decarboxylation is the favored pathway in the presence of water. The optimized transition-state structures for the decomposition pathways show that water molecules facilitate the bond-breaking and bond-forming processes that lead to product formation. Water also has a strong effect on the relative stability of the transition states, which determines which decomposition pathway is favored energetically.

This study has demonstrated the utility of *ab-initio* methods in gaining insights into how a solvent may influence the reaction kinetics and mechanisms. There are, however, some limitations inherent to these methods. All the calculations presented in this study involve only up to two solvent molecules. Although such calculations provide some information about the reaction kinetics and valuable insights into the reaction mechanisms on a molecular level, they cannot accurately and completely describe the effect of water as a solvent on the reaction kinetics. In addition, only two types of configurations of hydrated formic acid were considered in this study. There are, however, numerous other possible ways in which a formic acid molecule can interact with surrounding water molecules, some of which could be lower in energy than the configurations considered in this study. For these reasons, the kinetic parameters reported in this study may not correspond exactly to experimentally accessible values.

Further efforts must be made to address the solvent effect completely. To obtain a more detailed picture of the role of water in the reaction, it is necessary to include more than just two water molecules in the formic acid–water cluster. It is computationally infeasible, however, to use *ab-initio* methods to explicitly consider all possible configurations of hydrated formic acid with multiple water molecules. A more tractable way of approaching this problem is to study the reaction by molecular simulations, either Monte Carlo or molecular dynamics. Molecular simulations allow one to study the averaged effect of a solvent on a reaction. For example, molecular simulations can determine the structure of solvent molecules surrounding the reactive solute, which provides insights into the nature of the solute–solvent interactions and the reaction environment at a molecular level. In addition, molecular simulations can calculate the potential of mean force, from which a reaction profile can be constructed.

## Acknowledgments

This material is based upon work supported under a National Science Foundation Graduate Fellowship. This work was also supported by NSF grant CTS-9521698.

## Literature Cited

Becke, A. D., "Density-Functional Thermochemistry. III. The Role of Exact Exchange," *J. Chem. Phys.*, **98**, 5648 (1993).

Bjarnov, E., and W. H. Hocking, "The Structure of the Other Rotamer of Formic Acid, *cis*-HCOOH," *Z. Naturforsch. Teil A*, **33**, 610 (1978).

Bjerre, A. B., and E. Sørensen, "Thermal Decomposition of Dilute Aqueous Formic Acid Solutions," *Ind. Eng. Chem. Res.*, **31**, 1574 (1992).

Blake, P. G., H. H. Davies, and G. E. Jackson, "Dehydration Mechanisms in the Thermal Decomposition of Gaseous Formic Acid," *J. Chem. Soc. (B)*, 1923 (1971).

Blake, P. G., and C. Hinshelwood, "The Homogeneous Decomposition Reactions of Gaseous Formic Acid," *Proc. Roy. Soc. (A)*, **255**, 444 (1960).

Brill, T. B., J. W. Schoppelrei, P. G. Maiella, and A. Belsky, "Spectrokinetics of Solvo-Thermal Reactions," *Proc. Int. Conf. Solvothermal Reactions*, Committee of Solvothermal Technol. Res., Takamatsu, Kagawa, Japan, p. 5 (1996).

Foresman, J. B., and Æ. Frisch, *Exploring Chemistry with Electronic Structure Methods*, 2nd ed., Gaussian, Inc., Pittsburgh (1996).

Francisco, J. S., "A Comprehensive Theoretical Examination of Primary Dissociation Pathways of Formic Acid," *J. Chem. Phys.*, **96**, 1167 (1992).

Frisch, M. J., G. W. Trucks, H.B. Schlegel, P. M. W. Gill, B. G. Johnson, M. A. Robb, J. R. Cheeseman, T. Keith, G. A. Petersson, J. A. Montgomery, K. Raghavachari, M. A. Al-Laham, V. G. Zakrzewski, J. V.Ortiz, J. B. Foresman, C. Y. Peng, P. Y. Ayala, W. Chen, M. W. Wong, J. L. Andres, E. S. Replogle, R. Gomperts, R. L. Martin, D. J. Fox, J. S. Binkley, D. J. Defrees, J. Baker, J. P. Stewart, M. Head-Gordon, C. Gonzalez, and J. A. Pople, *Gaussian 94*, Rev. B.3, Gaussian, Inc., Pittsburgh (1995).

Goddard, J. D., Y. Yamaguchi, and H. F. Schaefer, "The Decarboxylation and Dehydration Reactions of Monomeric Formic Acid," *J. Chem. Phys.*, **96**, 1158 (1992).

Graner, G., C. Rossetti, and D. Bailly, "The Carbon Dioxide Molecule: A Test Case for the $r_0$, $r_e$, and $r_m$ Structures," *Mol. Phys.*, **58**, 627 (1986).

Haar, L., J. S. Gallagher, and G. S. Kell, *NBS/NRC Steam Tables*, Hemisphere, Washington, DC (1984).

Hocking, W. H., "The Other Rotamer of Formic Acid, *cis*-HCOOH," *Z. Naturforsch. Teil A*, **31**, 1113 (1976).

Hsu, D.S., W. M. Shaub, M. Blackburn, and M. C. Lin, "Thermal Decomposition of Formic Acid at High Temperatures in Shock Waves," *Proc. Int. Symp. on Combustion*, Combust. Inst., Pittsburgh, PA, p. 89 (1982).

Jeppesen, C. R., "The Emission Spectrum of Molecular Hydrogen in the Extreme Ultraviolet," *Phys. Rev.*, **44**, 165 (1933).

Johnston, H. S., *Gas Phase Reaction Rate Theory*, Ronald Press, New York (1966).
Kumaresan, R., and P. Kolandaivel, "Structure and Stability of the Formic Acid Monomer and the Formic Acid-Water Complex. An *ab initio* Study," *Z. Phys. Chem.* **192**, 191 (1995).
Kwei, G. H., and R. F. Curl, Jr., "Microwave Spectrum of $O^{18}$ Formic Acid and Structure of Formic Acid," *J. Chem. Phys.*, **32**, 1592 (1960).
Laidler, K. J., *Chemical Kinetics*, 3rd ed., Harper Collins, New York (1987).
Lee, C., W. Yang, and R. G. Parr, "Development of the Colle-Salvetti Correlation-Energy Formula into a Functional of the Electron Density," *Phys. Rev. (B)*, **37**, 785 (1988).
Lide, D. R., Jr., "Microwave Studies of Rotational Isomerism," *Trans. Amer. Crystallogr. Assoc.*, **2**, 106 (1966).
Melius, C. F., N. E. Bergan, and J. E. Shepherd, "Effects of Water on Combustion Kinetics at High Pressure," *Proc. Int. Symp. on Combustion*, Combust. Inst., Pittsburgh, PA, p. 217 (1990).
Miehlich, B., A. Savin, H. Stoll, and H. Preuss, "Results Obtained with the Correlation Energy Density Functionals of Becke and Lee, Yang and Parr," *Chem. Phys. Lett.*, **157**, 200 (1989).
Mishra, V. S., V. V. Mahajuni, and J. B. Joshi, "Wet Air Oxidation," *Ind. Eng. Chem. Res.*, **34**, 2 (1995).
Miyazawa, T., and K. S. Pitzer, "Internal Rotation and Infrared Spectra of Formic Acid Monomer and Normal Coordinate Treatment of Out-of-Plane Vibrations of Monomer, Dimer, and Polymer," *J. Chem. Phys.*, **30**, 1076 (1959).
Peng, C., P. Y. Alaya, H. B. Schlegel, and M. J. Frisch, "Using Redundant Internal Coordinates to Optimize Geometries and Transition States," *J. Comp. Chem.*, **17**, 49 (1996).
Peng, C., and H. B. Schlegel, "Combining Synchronous Transit and Quasi-Newton Methods for Finding Transition States," *Isr. J. Chem.*, **33**, 449 (1993).
Ruelle, P., "*Ab Initio* Study of the Unimolecular Pyrolysis Mechanisms of Formic Acid: Additional Comments Based on Refined Calculations," *J. Amer. Chem. Soc.*, **109**, 1722 (1987).
Ruelle, P., U. W. Kesselring, and H. Nam-Tran, "*Ab Initio* Quantum-Chemical Study of the Unimolecular Pyrolysis Mechanisms of Formic Acid," *J. Amer. Chem. Soc.*, **108**, 371 (1986).
Saito, K., T. Kakumoto, H. Kuroda, S. Torii, and A. Imamura, "Thermal Unimolecular Decomposition of Formic Acid," *J. Chem. Phys.*, **80**, 4989 (1984).
Schlegel, H. B., "Optimization of Equilibrium Geometries and Transition Structures," *J. Comp. Chem.*, **3**, 214 (1982).
Shavitt, I., "A Calculation of the Rates of the Ortho-Para Conversions and Isotope Exchanges in Hydrogen," *J. Chem. Phys.*, **31**, 1359 (1959).
Thornton, T. D., and P. E. Savage, "Phenol Oxidation in Supercritical Water," *J. Supercrit. Fluids*, **3**, 240 (1990).
XMol, version 1.3.1, Minnesota Supercomputer Center, Inc., Minneapolis, MN (1993).
Yu, J., and P. E. Savage, "Decomposition of Formic Acid under Hydrothermal Conditions," *Ind. Eng. Chem. Res.*, in press (1998).

*Manuscript received Aug. 13, 1997, and revision received Nov. 17, 1997.*

ELSEVIER

Fuel Processing Technology 42 (1995) 109–127

FUEL PROCESSING TECHNOLOGY

# Catalytic partial oxidation of natural gas to syngas☆

S.S. Bharadwaj, L.D. Schmidt*

*Department of Chemical Engineering and Materials Science, University of Minnesota, Minneapolis, MN 55455-0132, USA*

Received 21 January 1994; accepted in revised form 12 July 1994

**Abstract**

We trace the development of catalytic partial oxidation technology for the conversion of natural gas to synthesis gas ($CO + H_2$) from steam reforming to autothermal reforming to direct oxidation. Synthesis gas which has applications in methanol, ammonia and Fischer–Tropsch synthesis has been conventionally produced by endothermic steam reforming processes in fired tube furnaces. Catalytic partial oxidation is much faster, highly selective in a single reactor, and much more energy efficient. It could thus significantly decrease capital and operating costs of syngas production. In this review, we consider catalysts as well as reactors. Processes, issues and practical difficulties are discussed with academic and industrial efforts presented in parallel. New millisecond contact time direct oxidation processes which eliminate the use of steam and use autothermal reactors orders of magnitude smaller than those used for conventional steam reforming hold promise for commercialization.

## 1. Introduction

Large portions of the world's reserves of natural gas remain virtually untouched and need to be effectively utilized. The need for synthetic fuels is also increasing as the recovery of petroleum becomes more difficult and expensive. Remote locations of much of the discovered gas reserves make it desirable to convert the gas on-site to liquid products which are economically transportable. Almost all options for methane utilization involve its initial conversion to synthesis gas ($CO + H_2$). Synthesis gas can then be converted to paraffinic liquid fuels through Fischer–Tropsch reactions [1] on Fe, Co, Ru and similar metals,

$$n\mathrm{CO} + 2n\mathrm{H_2} \rightarrow (-\mathrm{CH_2}-)_n + n\mathrm{H_2O},$$

☆ This research was supported by DOE under Grant DE-F02-88ER13878-AO2.

* Corresponding author. Fax.: + 612 6267246. Tel.: + 1 612 6251313.


*SSDI* 0378-3820(94)00098-0

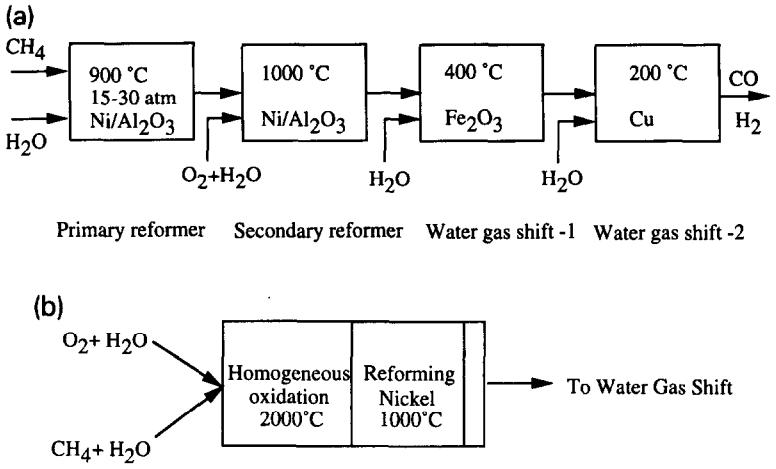


Fig. 1. (a) *Block diagram for conventional steam reforming*: $CH_4$ and excess $H_2O$ are reacted in a primary reformer over $Ni/Al_2O_3$ at 900°C. The unconverted $CH_4$ (8–10%) is reacted with $O_2$ and more $H_2O$ in a secondary reformer to give equilibrium CO and $H_2$. The product $H_2/CO$ ratio is then modified in two water gas shift stages [1, 3]. (b) *Schematic representation of autothermal reforming*: $CH_4$ is reacted with $O_2$ in a flame and the products of homogeneous partial oxidation are then reformed by $H_2O$ in the feed over a Ni catalyst bed. The product synthesis gas composition is then adjusted in water gas shift stages as shown in Fig. 1(a).

or first to methanol over Cu/ZnO and then to gasolene by the MTG [1] process over zeolite catalysts.

$$CO + 2H_2 \rightleftarrows CH_3OH, \quad \Delta H = -21.75 \text{ kcal/mol}.$$

Synthesis gas is also used for the production of oxoalcohols and acetic acid. The hydrogen produced after water gas shift (WGS) is used for ammonia synthesis, hydrotreating processes and reduction in metallurgical operations.

It has been estimated that in most applications of synthesis gas such as methanol, Fischer–Tropsch synthesis and ammonia about 60–70% of the cost of the overall process is associated with syngas generation [2]. Reduction in syngas generation costs would have a large and direct influence on the overall economics of these downstream processes.

## 2. Steam reforming

Synthesis gas is currently produced by catalytic steam reforming [3] of natural gas or naphtha. We shall emphasize natural gas ($CH_4$) here although heavier feedstocks can be processed with similar technologies and conditions. Steam reforming has been used for many decades since first developed in 1926 [1] and over the years there have been many advances in reforming technology. As sketched in Fig. 1(a) [1, 3], in

a typical process, natural gas is partially reacted with steam over a $Ni/\alpha\text{-}Al_2O_3$ catalyst in a *primary reformer* to produce syngas at an $H_2:CO$ ratio of 3:1,

$$CH_4 + H_2O \rightarrow CO + 3H_2 \quad \Delta H = +49.2 \text{ kcal/mol.}$$

The reaction is highly endothermic and is carried out in a fired tube furnace at 900°C at pressures of 15–30 atm. The superficial contact time (based on feed gases at STP) is 0.5–1.5 s which corresponds to residence times of several seconds. Excess steam is used to prevent carbon formation on the catalyst, and the feed $H_2O/CH_4$ mol ratios are typically 2–6, depending on the syngas end use. Potassium compounds or other bases (CaO and MgO) are typically used to accelerate carbon removal reactions. The $CH_4$ conversion at the exit of the primary reformer is typically 90–92% and the product mixture contains $CO_2$ and $H_2O$ along with CO and $H_2$. This mixture composition is close to that predicted by equilibrium for a 1:3 $CH_4:H_2O$ feed shown in Fig. 2(a).[1]

The primary reformer is followed by a secondary autothermal reforming stage in which the unconverted $CH_4$ is reacted with $O_2$ at the top of a refractory lined vessel. The product mixture is then equilibrated over a packed bed of Ni catalyst below the oxidation zone. The exothermicity of the oxidation reactions is used to produce high pressure steam to drive the turbines for the syngas compressor. In newer configurations, better energy integration allows heat evolved in the secondary reformer to be used for the primary reformer in which the fired tube furnace is replaced by a heat exchange reformer. Over the years the steam reforming process has been optimized with the design of better burners for the furnaces, highly creep resistant materials for the reformer tubes, and new sulfur passivated catalysts which inhibit carbon formation [4].

Depending on the end use, the secondary reformer is usually followed by two water gas shift (WGS) reactors to adjust the $H_2/CO$ ratio of the reformer product gases, as sketched in Fig. 1(a).

$$CO + H_2O \rightleftarrows CO_2 + H_2, \quad \Delta H = -9.8 \text{ kcal/mol.}$$

A high temperature shift over iron oxide/chromia catalysts at 400°C is followed by a low temperature shift at 200°C on a copper-based catalyst to attain favorable equilibrium in WGS. Both WGS stages have superficial contact times greater than 1 s. The syngas is then exported after subsequent purification stages.

## 3. Autothermal reforming

This process, sketched in Fig. 1(b), is a combination of homogeneous partial oxidation and steam reforming and was first developed in the late 1970s with the aim of carrying out reforming in a single reactor [5]. The autothermal reformer is

[1] All thermodynamic calculations for Fig. 2 were performed using STANJAN which uses a free energy minimization technique and thermodynamic data from the JANAF tables.

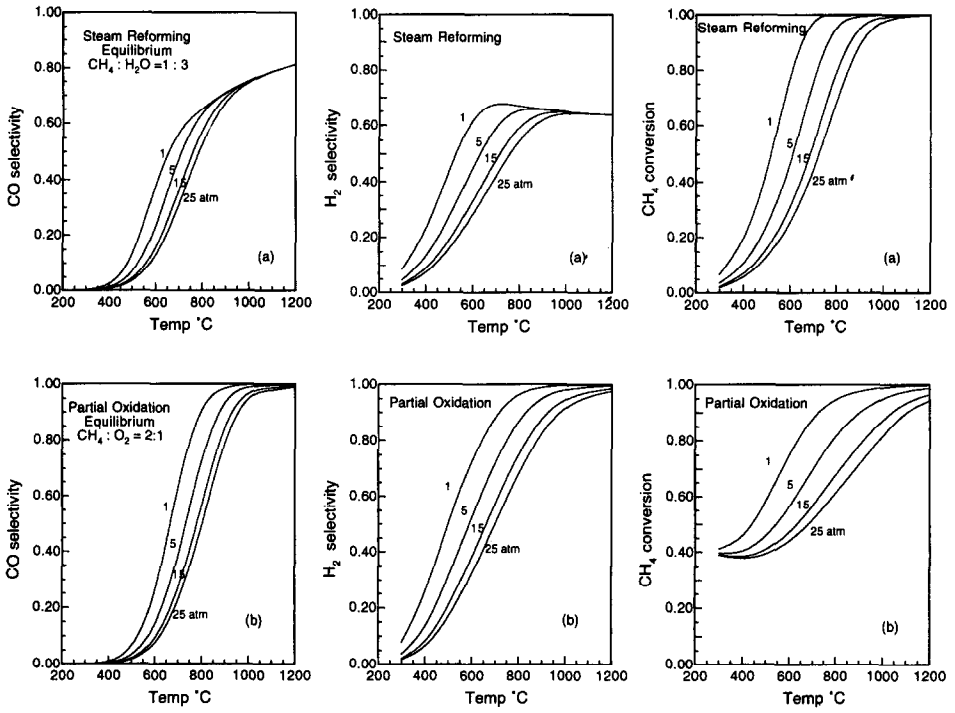


Fig. 2. (a) *Steam reforming equilibrium*: Plot of calculated equilibrium CO selectivity, $H_2$ selectivity and fractional $CH_4$ conversion for steam methane reforming vs. temperature (°C) and pressure (atm) for a 1:3 $CH_4$:$H_2O$ molar feed. (Note: $H_2$ selectivity is defined as $H_2/(H_2 + H_2O)$ although $H_2O$ is present in feed). (b) *Partial oxidation equilibrium*: Plot of calculated equilibrium CO selectivity, $H_2$ selectivity and fractional $CH_4$ conversion for partial oxidation vs. temperature (°C) and pressure (atm) for a 2:1 $CH_4$:$O_2$ molar feed. (Note: C(s) formation is accounted for in CO selectivity calculation).

a ceramic lined furnace similar to the $O_2$ fired secondary reformer used in conventional steam reforming. The preheated feed streams ($H_2O + CH_4$ and $H_2O + O_2$) are mixed in a burner located at the top where the partial oxidation reactions take place. $H_2O$ is added to the feed streams to prevent carbon formation and allow premixing of $CH_4$ and $O_2$. The final steam reforming and equilibration take place in the catalyst bed below the burner. At normal operation, the autothermal reforming operates at high temperatures around 2000°C in the combustion zone and 1000–1200°C in the catalytic zone. The product gas composition can be adjusted by varying the $H_2O/CH_4$ or $CO_2/CH_4$ in the feed.

This process requires an inexpensive source of $O_2$. An undesired side reaction in the combustion zone is the formation of carbon or soot which leads to solid carbon deposition on the catalysts and subsequent coking and deactivation. Gas phase carbon forms soot on downstream surfaces thereby causing equipment damage and heat transfer problems. Excessive local temperatures also lead to burner damage. This

also calls for a catalyst of high thermal stability and mechanical strength. In newer configurations catalytic burners have been tested.

In another process the combustion and reforming may be carried out in separate reactors. A $CH_4/O_2/H_2O$ mixture is ignited in a burner to produce partial oxidation products which are then catalytically steam reformed in a second reactor to give equilibrated products.

Recently, Exxon patented a process for the *autothermal steam reforming* of methane with oxygen in a fluidized bed reactor [6]. Pilot plant studies were carried out in which methane is converted to synthesis gas at elevated temperatures and pressures in the presence of a particulate catalyst, e.g. $Ni/Al_2O_3$. $H_2O$ is used to suppress coke formation. The conversion of the feed to syngas is preserved by rapidly cooling the reaction production to a temperature below that which favors the back reaction of carbon monoxide and hydrogen to form methane.

## 4. Direct oxidation

Over the years the emphasis has been on minimizing the use of steam whose disadvantages are (1) endothermic reactions, (2) product at a 3/1 $H_2/CO$ ratio, (3) steam corrosion problems, and (4) costs in handling excess $H_2O$. The process has therefore moved steadily from steam reforming to 'wet' oxidation, and in recent years research has been devoted to direct 'dry' oxidation of $CH_4/O_2$ mixtures.

$$CH_4 + \tfrac{1}{2}O_2 \rightarrow CO + 2H_2, \quad \Delta H = -8.5 \text{ kcal/mol.}$$

With minimum steam such a process directly gives the desired 2:1 ratio required for methanol or Fischer-Tropsch synthesis. While this reaction and these species are favored thermodynamically at $T > 900°C$ in excess methane as shown in Fig. 2(b),[2] the selectivities are affected by the formation of $H_2O$ and somewhat by $CO_2$ in total oxidation reactions which are much more exothermic,

$$CH_4 + \tfrac{3}{2}O_2 \rightarrow CO + 2H_2O, \quad \Delta H = -124.1 \text{ kcal/mol,}$$

$$CH_4 + 2O_2 \rightarrow CO_2 + 2H_2O, \quad \Delta H = -191.8 \text{ kcal/mol.}$$

Since the direct oxidation reaction is slightly exothermic, a reactor based on this reaction would be much more energy efficient than the energy intensive steam reforming process. Oxidation reactions are also much *faster* than reforming reactions, suggesting that a *single stage process* for syngas generation would be a viable alternative to steam reforming and also result in *smaller reactors and higher throughput.*

A recent study [7] showed that there are significant economic incentives for on-site methanol plants based on the catalytic partial oxidation of natural gas. An estimated

[2] All thermodynamic calculations for Fig. 2 were performed using STANJAN which uses a free energy minimization technique and thermodynamic data from the JANAF tables.

10–15% reduction in the energy requirement and 25–30% lower capital investment is expected for catalytic partial oxidation compared to the typical steam reforming processes.

However, the direct oxidation process has not yet been used commercially, and it is difficult to study fundamentally because it involves premixing of $CH_4/O_2$ mixtures which can be *flammable* or even *explosive*. Homogeneous reactions in a highly reducing environment can lead to soot formation and carbon deposition on the catalyst. In addition, flames in the reaction zone can also lead to very high local temperatures which can destroy catalysts. However, recent discovery of highly selective direct oxidation catalysts have renewed interest in the direct oxidation process [12–22, 27, 28, 33, 35, 36]. These catalysts overcome the problem of carbon deposition without any steam input (totally dry oxidation). The absence of homogeneous reactions also prevent the formation of unwanted oxidation products or flames which can lead to soot formation.

### *4.1. Early research on direct oxidation*

Work on the partial oxidation of $CH_4$ to synthesis gas began as early as 1946. Prettre et al. [8] studied catalytic conversion of $CH_4/O_2$ mixtures employing a reduced 10% refractory-supported Ni catalyst in the temperature range 725–900°C and 1 atm total pressure. Experiments were performed using 20–40 $cm^3$ of catalyst at bed depths of $\sim$ 12 cm and superficial contact times of 6–42 s. Temperature excursions in the catalyst bed under $O_2$-deficient conditions ($CH_4:O_2 = 2:1$), suggested that an initial exothermic reaction was followed by an endothermic stage. The exothermic behavior near the beginning of the catalyst bed was attributed to the total combustion of 25% of the $CH_4$ feed, which resulted in complete consumption of the stoichiometrically limited $O_2$ reactant,

$$CH_4 + 2O_2 \rightarrow CO_2 + 2H_2O.$$

The subsequent endothermic effect was ascribed to reforming of the remaining unreacted $CH_4$ by the $H_2O$ and/or $CO_2$ produced:

$$CH_4 + H_2O \rightarrow CO + 3H_2,$$

$$CH_4 + CO_2 \rightarrow 2CO + 2H_2.$$

Compositions of the final reaction mixtures agreed with thermodynamic predictions based on the catalyst bed exit temperatures. They found that to obtain almost complete conversion of $CH_4$, temperatures in excess of 850°C were required.

Over the next 25 years while the field of steam reforming matured, not much was done on partial oxidation reaction systems. In 1970, Huszar et al. [9] examined the importance of diffusion effects during methane partial oxidation by studying the reaction of 25% $CH_4$ : air mixtures over a single grain of Ni/mullite catalyst in the temperature range 760–900°C. They saw ignition and extinction characteristic of catalytic systems. An interesting phenomenon they observed was that the Ni catalyst

would deactivate in an oxidizing environment but could be recovered on reduction (with some loss of activity). The same effect has also been observed in recent experiments in fixed [19] and fluidized beds [36] and is attributed to the formation of $NiAl_2O_4$ which is inactive for oxidation. Huszar et al. concluded that the formation of $H_2/CO$ product required the presence of reduced metallic Ni, achieved by using $O_2$ deficient conditions, and that the kinetics of the overall process were limited by the rate of diffusion of $O_2$ through the gas film surrounding the grain into the catalyst pores. The effective concentration of $O_2$ at the catalyst surface was essentially zero, allowing the Ni to be maintained in the zero valent state.

In 1984, Gavalas et al. [10] studied the effects of calcination temperature, prereduction and feed ratio on the catalytic behavior of $NiO/\alpha\text{-}Al_2O_3$ for conversion of $CH_4/O_2$ mixtures at 570–760°C. For $CH_4/O_2$ feed ratios of 1.3–1.7, they observed a decrease in initial activity with increasing calcination temperature, which they attributed to changes in the $Ni^{3+}$ surface concentration. They also observed a decline in activity with increasing time on stream. The principal products in all cases under these conditions were $CO_2$ and $H_2O$. Prereduction in $H_2$ at 650–760°C caused the initial activity to increase by one to three orders of magnitude, depending upon prior calcination temperature. The authors believed that the zero valent nickel produced by prereduction reverted to NiO under the reaction conditions employed, resulting again in a decline in activity with increasing time on stream. At a reaction temperature of 710°C, $CO_2$ remained the only carbon containing product until the $CH_4/O_2$ feed ratio was increased to $> 8$, at which point CO and $CO_2$ were produced in comparable amounts.

We note here that only Ni catalysts (which are typically used for steam reforming) were the subject of most early investigations.

### 4.2. Recent research

In the past few years, efforts at producing cheaper synthetic fuels have renewed interest in partial oxidation and both catalytic (CPOX) and non-catalytic (POX) oxidation have been studied extensively by industry and by several groups in academia. Non-catalytic partial oxidation has been recently used industrially, but several problems are encountered. Although catalytic partial oxidation has never been used commercially it is most promising because it offers the advantages of (1) heterogeneous reactions, (2) lower temperatures than in a non-catalytic process, and (3) no formation of soot or unwanted by-products. This review focuses on the status of current research on the catalytic partial oxidation of natural gas to synthesis gas.

Most laboratory studies on CPOX have been conducted in fixed bed microreactors as shown in Fig. 3(a). Very recently, monolith reactors (Fig. 3(b)) and fluidized beds (Fig. 3(c)) have also been used with success.

#### 4.2.1. Fixed bed reactors

Most experiments examining partial oxidation of $CH_4$ with oxygen in fixed beds have been carried out in quartz microreactors $\sim$ 1–4 mm in diameter with 20–50 mg

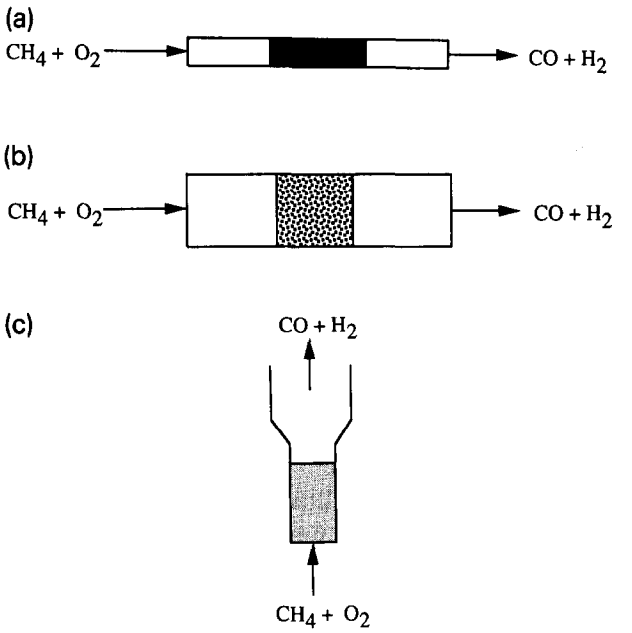


Fig. 3. *Direct oxidation reactors.* (a) Fixed bed microreactor: These are typically quartz tubes 2–4 mm in diameter with 20–50 mg powder catalyst beds externally heated with wall tube furnaces. (b) Monolith reactor: These consist of a quartz tube ~ 2 cm in diameter with the metal catalyst in the form of a gauze or supported on foam or extruded monoliths made of alumina or cordierite. These reactors operate autothermally. (c) Fluidized bed reactor: These are quartz tubes ~ 3 cm in diameter and 15–20 cm tall with an expansion for catalyst disengagement. The catalyst is typically 0.5–2.0 wt% metal supported on 75–150 μm $\alpha$-$Al_2O_3$ particles. These reactors can also operate autothermally.

of powder catalysts [11–28] with reactor tubes placed in a furnace or heater to thermostatically control temperatures.

Blanks et al. [11] studied direct oxidation in a reactor using natural gas and air at atmospheric pressure and 800–1000°C over a $Ni/Al_2O_3$ catalyst. This reactor operated adiabatically, implementing an unsteady-state mode of operation in which the flow direction was periodically reversed to maintain high temperatures. At the entrance to the reaction zone, the combustion reactions occurred, resulting in a peak temperature of 950°C. Downstream from this zone, steam reforming and $CO_2$ reforming converted most of the remaining $CH_4$ to syngas. Residence times of about 0.25 s were required to give $H_2$ and CO selectivities of 75–85% and 75–95% respectively, with 85–97% conversion of the methane feed.

A significant contribution to this field has been made by Ashcroft and coworkers [12–16] in a series of five papers in which they report evaluation of a large number of catalysts for syngas production. They first studied methane oxidation to syngas over a number of rare earth ruthenium oxides of the pyrochlore type ($(\text{rare earth})_2Ru_2O_7$) and then on several transition metals (Pt, Rh, Ru, Ni, Ir) supported on $Al_2O_3$. With a 2:1:4 $CH_4:O_2:N_2$ feed, $T > 750$°C and superficial contact times of ~ 0.1 s, they

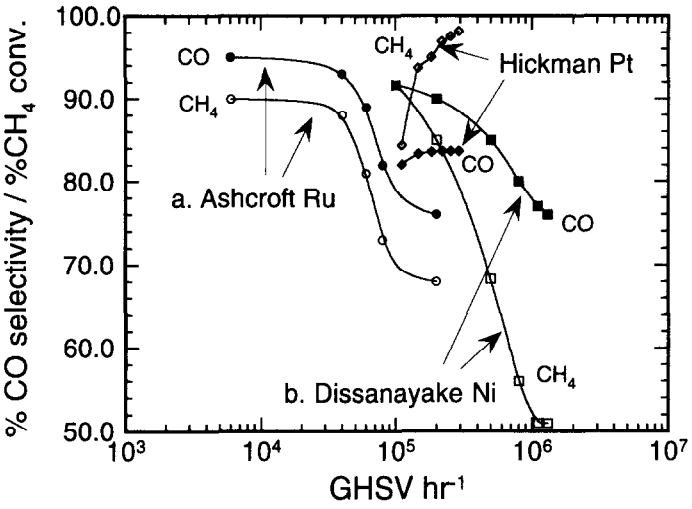


Fig. 4. Plot of the effect of contact time on CO selectivity (bold symbols) and $CH_4$ conversion (open symbols). The contact time is represented by gas hourly space velocity (GHSV $h^{-1}$) and is calculated at STP conditions. This plot was constructed using data from: (a) Ashcroft et al. [14], $CH_4/O_2 = 2$, 777°C, $Pr_2Ru_2O_7$ catalyst. (b) Dissanayake et al. [19] $CH_4/O_2 = 1.78$, 800°C, $Ni/Al_2O_3$ catalyst. The very high space velocities were achieved by dilution with He. (c) Hickman et al. [31] $CH_4/O_2 = 0.9$, ~ 1227°C, 10 layer Pt-10% Rh gauze pack.

found $CH_4$ conversions in excess of 90% with selectivities in the range of 94–99% for all catalysts, suggesting that all were nearly equal and that the active catalyst was the supported metal. This was confirmed by Poirier et al. [17] in their studies on the partial oxidation of methane on $Pr_2Ru_2O_7$ by microreactor experiments and thermal analysis (TG/DTA). Their results show that $Pr_2Ru_2O_7$ has to be reduced to ruthenium metal and to praseodymium oxide to be active for methane conversion and that ruthenium metal is the active site for synthesis gas formation.

Ashcroft et al. also showed that under similar conditions of temperature and pressure catalysts such as $Ir/Al_2O_3$ were also active for the combined partial oxidation and $CO_2$ reforming reaction giving synthesis gas in similarly high yield [15]. They studied the effect of contact time and found that with a decrease in contact time the conversions and selectivities decrease as shown in Fig. 4. They also studied the effect of pressure up to 20 atm and found a significant decrease in reaction conversion and selectivities. For a $Dy_2Ru_2O_7$ catalyst, the $CH_4$ conversion, CO selectivity and $H_2$ selectivity which were 56%, 99% and 100%, respectively, at 1 atm fell to 30%, 85% and 88% at 20 atm. This is an important observation because scaleup would require operation at the high pressures required for methanol synthesis and Fischer–Tropsch synthesis (typically 30–60 atm).

They suggested that the reaction pathway may involve initial conversion of some $CH_4$ to $CO_2$ and $H_2O$, followed by a sequence of steam reforming and reverse water gas shift reactions to give equilibrium product yields. Ashcroft and coworkers,

however, did not comment upon the thermal gradients in the catalyst bed and their effect on results. The effect of heat transfer could be significant because total oxidation reactions are highly exothermic.

The problem of hot spots in a microreactor bed has been well demonstrated by Vermeiren et al. [18]. They show that methane–oxygen mixtures can be converted to synthesis gas with high yields (> 90%) using Ni-based catalysts. Carefully measuring the temperature gradients in the catalyst bed for a fixed furnace temperature they found a pronounced exotherm near the inlet of the catalyst bed indicating the occurrence of exothermic reactions near the inlet and endothermic reactions in the latter half of the bed. The 'hot spot' temperature was ~100°C above the temperature of the catalyst in absence of any reaction. They also found that while at a furnace temperature of 800°C the $CH_4$ conversion and CO selectivity are almost invariant with space time, at 600°C both *increase* with *decreasing* space time. They suggested that this behavior could only be explained by a sequential reaction mechanism. They call this process 'oxyreforming' and by comparing experimental data with thermodynamic predictions for various reaction models they also suggest that catalytic oxyreforming consists of a combination of combustion, steam reforming and water gas shift reactions.

Dissanayake et al. [19] examined the oxidation state and phase composition of a 25 wt% $Ni/Al_2O_3$ catalyst for $CH_4$ oxidation under $O_2$ deficient conditions as a function of axial position in the catalyst bed at atmospheric pressure and at temperatures between 450 and 900°C. With a feed mixture of $CH_4:O_2:He = 1.78:1:25$, contact times of about 0.1s were required to give equilibrium yields of CO and $H_2$. CO selectivities approaching 95% and virtually complete conversion of $CH_4$ feed could be achieved at temperatures above 700°C. Higher space velocities were achieved by increasing the flow rate of He while maintaining the $CH_4$ and $O_2$ flows constant. Just as Ashcroft and coworkers, they also observed deviations from thermodynamic equilibrium at shorter contact times accompanied by decreasing conversions and selectivities (also shown in Fig. 4).

X-ray photoelectron spectroscopy and X-ray powder diffraction revealed that under operating conditions, the previously calcined catalyst bed consisted of three different regions. The first of these contacting the initial $CH_4/O_2/He$ feed mixture was $NiAl_2O_4$ which had moderate activity for complete oxidation of $CH_4$ to $CO_2$ and $H_2O$. The second region was $NiO + Al_2O_3$, over which *complete oxidation* of $CH_4$ to $CO_2$ and $H_2O$ occurred, resulting in a strong exotherm in this section. The temperature in this section was found to be 50°C higher than the rest of the bed. As a result of complete consumption of $O_2$ in the second region, the third portion of the catalyst bed consisted of a reduced $Ni/Al_2O_3$ phase. Formation of the CO and $H_2$ products corresponding to thermodynamic equilibrium at the catalyst bed temperature occurred in this final region via reforming reactions of the remaining $CH_4$ with the $CO_2$ and $H_2O$ produced.

They also found that if the contact time was sufficiently decreased, *breakthrough* of unreacted $O_2$ occurred, causing all of the reduced nickel on the surface to reoxidize to the inactive $NiAl_2O_4$ phase. Reattainment of thermodynamic equilibrium could be achieved by regenerating the reduced Ni by raising the temperature above 750°C or by reducing the catalyst in $H_2$.

In contrast, Choudhary et al. [20–22] recently reported successful operation of a similar reactor at very high space velocities on supported Ni catalysts at lower temperatures ( < 700°C). They found that at short contact times ( ~ 7 ms) the reaction is far from equilibrium and CO and $H_2$ selectivities *higher* than those predicted by equilibrium are obtained. They attributed this to a change in reaction path, although they were not sure of the reaction mechanism.

However, Dissanayake et al. [23] have recently pointed out that the apparent deviations of $CH_4/O_2$ reaction mixture products from thermodynamic equilibrium at high space velocities, as described by Choudhary et al. may have resulted due to a small undetected *hot zone* in their reactor and consequent incorrect determination of the true reaction temperature.

In another recent publication, Bhattacharya et al. [24] studied the partial oxidation of $CH_4$ with $O_2$ on a number of supported Pd catalysts in the temperature range of 100–750°C at gas hourly space velocities (GHSV) ranging 5000–20 000 $h^{-1}$ and with $CH_4:O_2$ ratios ranging from 4:1 to 8:1. The supports studied included oxides of metals belonging to Group IIIa and IVa of the Periodic Table, oxides of representative metals belonging to the lanthanide series, $\gamma$-$Al_2O_3$ and $SiO_2$. CO, $CO_2$, $H_2O$ and $H_2$ were the only detectable reaction products on all the catalysts. The CO selectivity on all the catalysts increased with an increase in reaction temperature, a decrease in GHSV and an increase in the $CH_4:O_2$ ratio. They found that as the temperature was increased beyond about 500°C, the amount of $CO_2$ decreased and carbon monoxide rapidly increased. At 750°C, CO was produced with 99.6% selectivity.

They suggested that $CH_4$ adsorbs on the catalyst surface to form a surface $CH_3$ species which desorbs to form $CO_2$ in the gas phase. The $CH_3$ species in parallel undergoes a surface reaction probably via formation of other $CH_x$ intermediate species to form CO. At higher temperatures the surface reaction rate exceeds desorption rate of the $CH_3$ species. Thus at temperatures of 750°C or above only carbon monoxide is produced. It is also possible that at temperatures above 650°C, the $CO_2$ initially produced reacts with the surface $CH_x$ species to form carbon monoxide and $H_2$. They also observed that CO is formed with > 90% selectivity on Pd supported on all the oxides, excepting $SiO_2$.

Mouaddib et al. [25] also report $Pd/Al_2O_3$ to be active for the partial oxidation and steam reforming of methane. At 498°C and $CH_4/O_2$ ratio of 1.5, they obtain 80% conversion of the methane with 57% selectivity to CO. Marti et al. [26] studied methane oxidation over $Pd/ZrO_2$ prepared from amorphous $Pd_1Zr_3$ alloy. At 600°C and $CH_4/O_2$ ratio of 8, they observe CO and $H_2$ selectivities in excess of 90%. However, the conversions were rather low ( ~ 24%) which was due to the high $CH_4/O_2$ ratio. At high temperatures, the reaction was influenced by the formation of carbonaceous deposits.

Another group from Japan, that of Nakamura et al. [27] has studied $CH_4$ oxidation on $SiO_2$ supported group VIII metal catalysts in a conventional fixed bed flow reactor at superficial contact times of ~ 0.15 s. They found that above 627°C, the conversion of $CH_4$ to CO and $H_2$ was about 90% over Rh, Ru, and Ni catalysts. They also subscribe to the theory of total oxidation followed by reforming and shift reactions to explain the observed results. As earlier observed by Huszar et al. and Dissanayake

et al. they also saw that, if the Ni surface was oxidized, it would become completely inactive for syngas formation. They attributed this to a retardation of the $CO_2$ and $H_2O$ reforming reactions in the absence of reduced metallic Ni. Pt also showed activity for syngas formation at 627°C. Pd showed lower activity for CO and $H_2$ formation and had a tendency to coke at higher temperatures. Only $CO_2$ and $H_2O$ were produced on Fe and CO.

Recently, Lapszewicz et al. [28] have pointed out that CO could be a primary product of $CH_4$ oxidation. They studied $CH_4$ oxidation with the objective of identifying the reaction pathway and to provide the information necessary for the development of catalysts suitable for the industrial application. They identified several catalysts (undisclosed) capable of producing CO with yields higher than the maximum predicted by equilibrium. In tests performed at different space velocities they found that while on some catalysts the CO selectivity increased, on others it decreased with a decrease in contact time. This provided evidence that either CO or $CO_2$ could be a primary product.

They further demonstrated this by performing experiments with two different feeds one consisting of a 2/1 $CH_4/O_2$ mixture and the other consisting of a 3/2/1 $CH_4/H_2O/CO_2$ mixture corresponding to the mixture remaining after the total oxidation step of the mechanism proposed by Prettre et al. They found substantial differences in the rates of $CH_4$ consumption and CO formation between the two feeds. While one catalyst was found to be good for both partial oxidation and reforming reactions, another was almost inactive for reforming but very good for the partial oxidation reaction. Also for $CH_4/O_2$ feeds they saw a sudden change in reaction rates once the temperature rose above a certain level. Based on these observations they suggested a free radical reaction mechanism on the catalyst surface. Following adsorption on the catalyst surface, they assumed that $CH_4$ and $O_2$ undergo homolytic dissociation

$$CH_4 \rightarrow (4 - x)[\cdot H]_{ads} + [\cdot CH_x]_{ads},$$

$$O_2 \rightarrow 2[\cdot O]_{ads}.$$

They postulated that either CO or $CO_2$ could be primary products formed from the surface intermediates $[\cdot CH_x]_{ads}$ and $[\cdot O]_{ads}$. The secondary reactions included reforming of $CH_4$ with $H_2O$ and $CO_2$, water gas shift and oxidation of $H_2$ and CO. The nearly complete $O_2$ conversions suggested that the rate limiting step was the activation of $CH_4$. This was confirmed by the observed increase in $CH_4$ conversion and CO formation rates with an increase in the metal loading.

An important point to be noted here is that most fixed bed processes described in this literature use heated *wall tube furnaces* to control the temperature rather than *autothermal reactors.*

### *4.2.2. Monolith reactors*

Monoliths were first used early on in this century in the form of gauzes for the oxidation of $NH_3$ to NO in $HNO_3$ synthesis and in the 1940s for HCN in similar

reactors [1]. However, the most extensive use of monoliths as catalyst supports in recent times has been in the automotive catalytic converter for the removal by complete oxidation of pollutants such as NO, CO, and unburnt hydrocarbons from automobile exhaust. In the automotive exhaust noble metals (Pt, Rh, Pd) are supported on wash coated cordierite. Catalytic oxidation on noble metal coated monoliths is also used in pollution control applications such as stack gas cleanup and $NO_x$ removal as in the *selective catalytic reduction* (SCR) process. In recent years there has been renewed interest in the possibility of using monolith supports instead of pellets for partial oxidation reactions in fixed beds.

Korchnak et al. [29] proposed a direct oxidation reactor which consisted of catalytic metals supported by an alumina washcoat on several cordierite extruded monoliths about 1 m in diameter stacked in series to give a total reactor length of about 2 m. This reactor required residence times of $\sim 40$ ms to obtain essentially complete conversion of $CH_4$. Recently Hochmuth [30] reported experimental results for a laboratory scale reactor based on this design. For these experiments, monoliths containing 300 cells per square inch were coated with a washcoat consisting of a 1/1 weight ratio of Pt and Pd deposited on a ceria-stabilized $\gamma$-$Al_2O_3$ powder. Product compositions approaching equilibrium values were achieved for feeds of $CH_4$, $O_2$, and $H_2O$ at superficial contact times of 10–30 ms. Detailed analysis of the composition and temperature profiles versus axial position indicated that all of the $O_2$ was converted to CO, $CO_2$, and $H_2O$ early in the reactor, with the reforming and shift reactions occurring downstream to give the final products.

The production of CO and $H_2$ by the catalytic partial oxidation of $CH_4$ in air at atmospheric pressure was recently examined in this laboratory over Pt-coated and Rh-coated monolith catalysts in *autothermal reactors* at residence times between $10^{-4}$ and $10^{-2}$ s [31, 32, 33].

They contrasted the performance of these two catalysts (Pt and Rh) at conditions approaching adiabatic reactor operation. Rh was found to be a much better catalyst than Pt. Using $O_2$, CO selectivities above 95% and $H_2$ selectivities above 90% with $> 90\%$ $CH_4$ conversion were reported for Rh catalysts (Fig. 5). By examining several catalyst configurations, including Pt-10% Rh woven gauzes and Pt or Rh coated ceramic foam and extruded monoliths, several reaction and reactor variables in producing CO and $H_2$ were examined. These experiments showed that the selectivity is improved by operating at higher gas and catalyst temperatures and by maintaining high rates of mass transfer through the boundary layer at the catalyst surface. At flow rates high enough to minimize mass transfer limitations, the Pt-10% Rh gauze, foam monoliths, and extruded monoliths all give similar selectivities and conversions, but with important differences resulting from different catalyst geometries and thermal conductivities.

These results provide several insights into the partial oxidation of $CH_4$ to synthesis gas. It is evident that this reaction system is governed by a combination of kinetic and transport effects. The reaction kinetics depend on the nature of the catalyst and the surface temperature, while transport of the gas species to the catalytic surface is a function of the catalyst geometry and flow velocities.

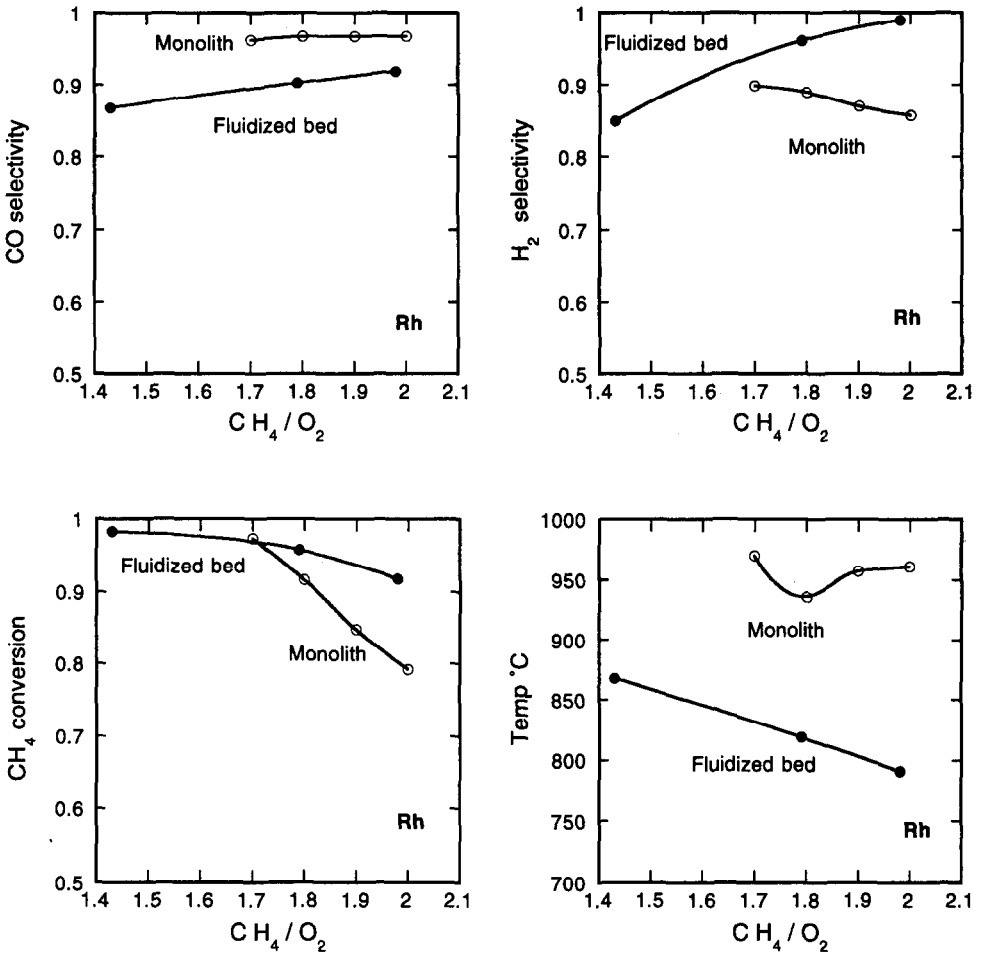


Fig. 5. Plot of CO selectivity, $H_2$ selectivity, $CH_4$ conversion and Temperature (°C) on a monolith (9.8 wt % Rh, 300°C preheat, 4 slpm) and in a fluidized bed (0.5 wt % $Rh/Al_2O_3$, 1.2 slpm).

An interesting observation is the increase in conversion and selectivities observed with a *decrease* in contact time in contrast to earlier observations of Ashcroft and coworkers and Dissanayake et al. This is shown in Fig. 4 which was constructed using data presented in references [14, 19, 31] to facilitate an easy comparison. As previously noted, an increase in conversion and selectivities with a decrease in contact time was also observed by Vermeiren et al. [18] at conditions of lower temperatures (600°C).

Hickman et al. suggested that the mechanism involved direct formation of $H_2$ initiated by $CH_4$ pyrolysis on the surface to give surface C and H species. The H adatoms dimerize and desorb as $H_2$ while the surface C atoms react with O adatoms and desorb as CO. However, any OH forming reactions on the surface

would inevitably give $H_2O$. $CO_2$ would be formed by the reaction of adsorbed CO and O species. To explain the superiority of Rh over Pt for $H_2$ generation, they showed that since the activation energy for OH formation on Rh (20 kcal/mol) was higher than on Pt (2.5 kcal/mol), H adatoms were more likely to combine and desorb as $H_2$ on Rh than on Pt, on which the $O + H \rightarrow OH \rightarrow H_2O$ reaction was much faster.

They observed that almost all conversion took place in the first few millimeters of the monolith (contact times < 1 ms) with complete $O_2$ conversion to give $H_2$ and CO. In contrast to previous attribution of the syngas generation to a *sequence* of total oxidation followed by reforming, they demonstrated that $H_2$ and CO are *primary products* of the *direct* oxidation of methane at such short contact times.

Hickman et al. [34] also modeled $CH_4$ oxidation using the $CH_4$ pyrolysis mechanism for an atmospheric pressure plug flow reactor model with reaction parameters from literature. Their model agreed well with the experiments, confirming that *direct oxidation* was the mechanism for oxidation on the monolith.

In ongoing experiments in this laboratory, Torniainen and Schmidt [35] studied methane oxidation on other metals supported on monoliths. Ni was found to give similar conversions and selectivities as Rh but exhibited deactivation via oxide and aluminate formation. Pt and Ir showed consistently lower conversions and selectivities although they were both stable. Ru and Fe were found to be inactive for the syngas reaction. Re was found to deactivate quickly by volatilization. Very low conversions and selectivities accompanied by deactivation were observed on the Co catalyst which formed an aluminate.

Pd coked heavily and deactivated, and the conversion decreased from 52% to 28% and $H_2$ selectivity decreased from 53% to 41% over 2.5 h. After running for 10 h, the catalyst and tube wall downstream of the catalyst were coated with coke. Migration of Pd to the back end of the monolith was also observed just as on Ru and Fe.

*4.2.3. Fluidized beds*

The option of using a fluidized bed reactor for syngas generation by direct oxidation has not been investigated until recently. There is renewed interest in fluidized beds for partial oxidation reactions because of several inherent advantages. Partial oxidation reactions are highly exothermic and their control and safe operation in fixed bed reactors can be difficult. Extreme precautions must be taken to avoid hydrocarbon/oxidant compositions inside flammable and explosive limits. In fluidized beds the heat transfer is good because of backmixing which ensures uniform temperature and safer operation. In addition, the pressure drop in a fluidized bed is lower than for a fixed bed of the same size for the same superficial gas velocity.

British Petroleum [37, 38] has developed processes for synthesis gas generation in spouted bed reactors, both catalytic (using supported Group VIII metal catalysts) as well as non-catalytic (using inert solids and refractory material). According to their patents, a rich $CH_4/O_2$ mixture is introduced with or without $H_2$ into a bed of particulate material with upward flow rate sufficient to cause a spouting action of the bed material. Steam may also be injected into the bed along with the reactant gases and/or into the product gas as a quench. This is particularly desirable when operating at pressures greater than 1 bar. The quenching reduces the temperature of the product

gases and stops or reduces further reaction to less useful products and soot. A gas burner located at the outlet of the reactor was used to ignite and maintain a stable flame on the spouted bed. Several inert refractory materials such as crushed firebrick, alumina and zirconia were used for the particulate material. With $Al_2O_3$ spheres, at a GHSV of 26400 $h^{-1}$ and $CH_4/O_2$ ratio of 1.78, $CH_4$ conversion of 68% was obtained with selectivities of 56.7%, 26.5% and 3% to CO, $C_2^+$ hydrocarbons (chiefly acetylene and ethylene) and soot respectively. In the catalytic version, the bed material comprised catalysts active for partial oxidation and/or steam reforming reactions. Typically, Group VIII metals optionally containing alkali metal on suitable supports were employed. With a conventional steam reforming catalyst, at 777°C and $CH_4/O_2$ of 1.62, a $CH_4$ conversion of 91.2% with CO selectivity of 90.4% was observed. With Pt catalysts, CO selectivities as high as 94.3% could be achieved at 87% $CH_4$ conversion. Operation at high pressures was also possible without significant loss in selectivities. At 24.8 bar, $CH_4$ conversions in excess of 90% and CO selectivities greater than 88% could be obtained with steam reforming catalysts at a $CH_4/O_2$ ratio of 1.7 and temperature of $\sim$ 1000°C.

The production of synthesis gas by the catalytic partial oxidation of $CH_4$ in air or $O_2$ in static fluidized beds at atmospheric pressure has recently been examined in this laboratory over Pt, Rh and Ni catalysts coated on 100 μm $\alpha$-$Al_2O_3$ beads [36]. With $CH_4$/air feeds, CO and $H_2$ selectivities as high as 95% with $>$ 90% $CH_4$ conversion were obtained on Rh and Ni catalysts. Pt catalysts were found to have significantly lower selectivities and conversions which may be due to more $H_2O$ forming reactions or the slow steam reforming behavior of Pt. The optimal selectivities for all the three catalysts were improved by heating the reaction mixture above the autothermal reactor temperature and using $O_2$ instead of air. The selectivities and conversions were fairly constant over the range of contact times between 0.1 and 0.5 s (calculated at reaction conditions). Experiments were also performed to study the effect of steam in the feed. With increasing steam in the feed an increase in $CH_4$ conversion and decrease in CO selectivity were observed indicating an approach to water gas shift equilibrium.

Fig. 5 allows a direct comparison between the selectivities, conversion and temperature for a fluidized bed [36] with those for a monolith [32], both using Rh catalysts and pure $O_2$ in the feed. Optimum selectivities and conversions are obtained at a $CH_4/O_2$ ratio of 2.0 in the fluidized bed and 1.7 on the monolith. Also the fluidized bed runs significantly cooler than the monolith.

Just as in fixed beds, there are two possible reaction pathways for $CH_4$ oxidation in the fluidized bed, (1) direct oxidation to CO and $H_2$ or (2) total oxidation followed by reforming. Longer times compared to monoliths may allow more reforming while increased backmixing in the fluidized bed compared to plug flow reactors may create more $H_2O$ initially.

The first pathway is direct oxidation via methane pyrolysis as proposed by Hickman et al. [32, 33] for experiments with monolith catalysts at shorter contact times. The low $H_2$ selectivities for Pt compared to Rh observed here conform very well with this mechanism.

The other reaction pathway may involve total oxidation of a part of the methane feed to $CO_2$ and $H_2O$ followed by steam reforming, $CO_2$ reforming and water gas

shift reactions as proposed to explain microreactor syngas experiments [8, 12–19, 27 30]. Because of the significant backmixing of gases along with solids circulation, $O_2$ and $H_2$ will be present simultaneously which should lead to more $H_2O$ formation. Also, the contact times (0.2–0.3 s) are sufficiently long for subsequent reforming and shift reactions to occur and give equilibrium CO and $H_2$ products. Rh and Ni also have a higher activity for steam reforming and methanation than Pt [39, 40] which would explain the lower CO and $H_2$ selectivities for Pt if reforming reactions play an important role.

We believe that homogeneous reactions involving free radicals do not play an important role in the reaction path in either monoliths or fluidized beds because no flames were observed. Also $C_2$ hydrocarbons, the formation of which involves free radical chemistry along with surface reactions were not detected in the product gases.

## 5. Summary

We have described how processes for syngas generation have evolved from endothermic steam reforming to direct catalytic autothermal partial oxidation. Over the years the transition has been from (1) 'wet' to 'dry', (2) endothermic to exothermic, (3) contact times of several seconds to milliseconds, and (4) large complex reactor configurations to simple small reactors.

For direct oxidation, Rh seems to be the catalyst of choice in either monolith or fluidized bed reactor configurations to achieve 95% + selectivities with 90% + conversion. One of the major engineering challenges is to ensure safe operation with premixed $CH_4/O_2$ mixtures. The reaction pathway seems to involve direct oxidation via $CH_4$ pyrolysis at short contact times ( $< 0.1$ s) while at longer times reforming and shift reactions may also play a role.

The short contact time direct oxidation process in autothermal reactors has promise of reducing reactor size by several orders of magnitude thereby reducing investment and operating costs. With renewed interest in inexpensive routes to liquid fuels from natural gas, direct catalytic oxidation is almost certainly the process of choice for future natural gas utilization.

## References

[1] Satterfield, C.N., 1991. Heterogeneous Catalysis in Industrial Practice. McGraw-Hill, New York.
[2] Haggin, J., 1992. Chem. Eng. News, 70(17): 33–35.
[3] Twigg, M.V. (Ed.), 1989. Catalyst Handbook. Wolfe Publishing Ltd., London.
[4] Dibbern, H.C., Olesen, P., Rostrup-Nielsen, J.R., Tottrup, P.B. and Udengaard, N.R., 1986. Hydrocarbon Process., 65(1); 71–74.
[5] Haldor Topsoe A/S and Soc. Belge de l'Azote, 1988. Hydrocarbon Process., 67(4): 77.
[6] Eberly, Jr. P.E., Goetsch, D.A., Say, G.R. and Vargas, J.M., 1988. Exxon Research and Engineering Company, Eur. Pat. Appl. EP 335, 668 (cl. COPB3/44), 04 October 1989, US Appl. 174, 174, March 28 1988.
[7] Korchnak, J.D. and Dunster, M., 1986. Reduced methanol production costs. Methane Conversion Conference, South Africa.

[8] Prettre, M., Eichner, C. and Perrin, M., 1946. The catalytic oxidation of methane to carbon monoxide and hydrogen. Trans. Faraday Soc., 43: 335–340.

[9] Huszar, K., Racz, G. and Szekely, G., 1971. Investigation of the partial catalytic oxidation of methane, I. conversion rates in a single-grain reactor. Acta Chim. Acad. Sci. Hungar., 70: 287–299.

[10] Gavalas, G.R., Phichitcul, C. and Voecks, G.E., 1984. Structure and activity of $NiO/\alpha-Al_2O_3$ and $NiO/ZrO_2$ calcined at high temperatures, I. Structure, II. Activity in the fuel rich oxidation of methane. J. Catal., 88: 54–64.

[11] Blanks, R.F., Wittrig, T.S. and Peterson, D.A., 1990. Bidirectional adiabatic synthesis gas generator. Chem. Eng. Sci., 45: 2407–2413.

[12] Ashcroft, A.T., Cheetham, A.K., Foord, J.S., Green, M.L.H., Grey, C.P., Murrell, A.J. and Vernon, P.D.F., 1990. Selective oxidation of methane to synthesis gas using transition metal catalysts. Nature, 344: 319–321.

[13] Ashcroft, A.T., Cheetham, A.K., Green, M.L.H. and Vernon, P.D.F., 1991. Partial oxidation of methane to synthesis gas using carbon dioxide. Nature, 352: 225–226.

[14] Vernon, P.D.F., Green, M.L.H., Cheetham, A.K. and Ashcroft, A.T., 1990. Partial oxidation of methane to synthesis gas. Catal. Lett., 6: 181–186.

[15] Vernon, P.D.F., Green, M.L.H., Cheetham, A.K. and Ashcroft, A.T., 1992. Partial oxidation of methane to synthesis gas, and carbon dioxide as an oxidising agent for methane conversion. Catal. Today, 13: 417–426.

[16] Jones, R.H., Ashcroft, A.T., Waller, D., Cheetham, A.K. and Thomas, J.M., 1991. Catalytic conversion of methane to synthesis gas over europium iridate, $Eu_2Ir_2O_7$: An in situ study by X-ray diffraction and mass spectrometry. Catal. Lett., 8: 169–174.

[17] Poirier, M.G., Jean, G. and Poirier, M.P., 1992. Partial oxidation of methane over a praseodymium/ruthenium pyrochlore catalyst. Stud. Surf. Sci. Catal., 73: 359–366.

[18] Vermeiren, W.J.M., Blomsma, E. and Jacobs, P.A., 1992. Catalytic and thermodynamic approach of the oxyreforming reaction of methane. Catal. Today, 13: 427–436.

[19] Dissanayake, D., Rosynek, M.P., Kharas, K.C.C. and Lunsford, J.H., 1991. Partial oxidation of methane to carbon monoxide and hydrogen over a $Ni/Al_2O_3$ catalyst. J. Catal., 132: 117–127.

[20] Choudhary, V.R., Rajput, A.M. and Prabhakar, B., 1993. Nonequilibrium oxidative conversion of methane to CO and $H_2$ with high selectivity and productivity over $Ni/Al_2O_3$ at low temperatures. J. Catal., 139: 326–328.

[21] Choudhary, V.R., Mamman, A.S. and Sansare, S.D., 1992. Selective oxidation of methane to CO and $H_2$ over Ni/MgO at low temperatures. Agnew. Chem. Int. Ed. Engl., 31(9): 1189–1190.

[22] Choudhary, V.R., Rajput, A.M. and Rane, V.R., 1992. Low-temperature catalytic selective partial oxidation of methane to CO and $H_2$ over $Ni/Yb_2O_3$. J. Phys. Chem., 96: 8686–8688.

[23] Dissanayake, D., Rosynek, M.P. and Lunsford, J.H., 1993. Are the equilibrium concentrations of CO and $H_2$ exceeded during the oxidation of $CH_4$ over a $Ni/Yb_2O_3$ catalyst?. J. Phys. Chem., 97: 3644–3646.

[24] Bhattacharya, A.K., Breach, J.A., Chand, S., Ghorai, D.K., Hartridge, A., Keary, J. and Mallick, K.K., 1992. Selective oxidation of methane to carbon monoxide on supported palladium catalyst. Appl. Catal., 80: L1.

[25] Mouaddib, N., Feumi-Jantou, C., Garbowski, E. and Primet, M., 1992. Catalytic oxidation of methane over palladium supported on alumina: Influence of the oxygen-to-methane ratio. Appl. Catal. A, 87: 129–144.

[26] Marti, P.E., Maciejewski, M. and Baiker, A., 1993. Methane oxidation over palladium on zirconia prepared from amorphous $Pd_1Zr_3$ alloy. J. Catal., 139: 494–509.

[27] Nakamura, J., Umeda, S., Kubushiro, K. and Kunimori, K., 1993. Production of synthesis gas by partial oxidation of methane over the group VIII metal catalysts. J. Japan Pet. Inst., 36(2): 97–104.

[28] Lapszewicz, J.A. and Jiang, X., 1992. Investigation of the mechanism of the partial oxidation of methane to synthesis gas. Preprints - Division of Petroleum Chemistry, Amer. Chem. Soc., 37(1): 252–260.

[29] Korchnak, J.D., Dunster, M. and English, A., 1990. World Intellectual Property Organization, WO 90/06282 and WO 90/06297.

[30] Hochmuth, J.K., 1992. Catalytic partial oxidation of methane over a monolith supported catalyst, Appl. Catal. B, 1: 89–100.
[31] Hickman, D.A. and Schmidt, L.D., 1992. Synthesis gas formation by direct oxidation of methane over Pt monoliths. J. Catal., 138: 267–282.
[32] Hickman, D.A. and Schmidt, L.D., 1993. Production of syngas by direct catalytic oxidation of methane. Science, 259: 343–346.
[33] Hickman, D.A., Haupfear, E.A. and Schmidt, L.D., 1993. Synthesis gas formation by direct oxidation of methane over Rh monoliths. Catal. Lett., 17: 223–237.
[34] Hickman, D.A. and Schmidt, L.D., 1993. Steps in $CH_4$ oxidation over Pt and Rh surfaces: High-temperature reactor simulations. AIChE J., 39(7): 1164–1177.
[35] Torniainen, P., Chu, X. and Schmidt, L.D., 1994. Comparison of monolith-supported metals for the direct oxidation of methane to syngas. J. Catal., 146: 1–10.
[36] Bharadwaj, S.S. and Schmidt, L.D., 1994. Synthesis gas formation by catalytic oxidation of methane in fluidized bed reactors. J. Catal., 146, 11–21.
[37] Brophy, J.H. and Telford, C.D., The British Petroleum Company P.L.C., European Patent 164864 (December 18, 1985), US Patent 4758375 (19 July, 1988).
[38] Brophy, J.H. and Manning R.P., The British Petroleum Company P.L.C., European Patent 178853 (April 23, 1986), US Patent 4726913 (February 23, 1988).
[39] Rostrup-Nielsen, J.R., 1973. J. Catal., 31: 173–199.
[40] Vannice, M.A., 1975. J. Catal., 37: 449–473.

# Mechanism and Reactivity of Alkane C−H Bond Dissociation on Coordinatively Unsaturated Aluminum Ions, Determined by Theoretical Calculations

**Dan Fărcaşiu* and Povilas Lukinskas**

*Department of Chemical and Petroleum Engineering, University of Pittsburgh, 1249 Benedum Hall, Pittsburgh, Pennsylvania 15261*

*Received: October 8, 2001*

DFT calculations at the B3LYP/6-31G** level were conducted on the reaction of the propane molecule with the aluminum hydroxide clusters $(HO)_3Al(OH_2)_x$ ($x = 0,1$). Weak, physisorbed (van der Waals) complexes were identified. Chemisorption does not involve the Brønsted acidity of the catalyst, as no hydron transfer occurs. Instead, the reaction involves insertion of the aluminum atom into a C−H bond, followed by the migration of the hydrogen atom from aluminum to oxygen, to form the chemisorbed intermediate, $(H_2O)_{x+1}(HO)_2Al-CH_2Et$ or $(H_2O)_{x+1}(HO)_2Al-CHMe_2$, with the latter having a higher energy barrier. The elimination of hydrogen from C$\beta$ and oxygen gives then $H_2$ and propene, which forms a strong $\pi$ complex with the aluminum cluster for $x = 0$. The first step, chemisorption, has a lower energy barrier than the second, elimination, but still higher than the hydrogen dissociation on the same clusters. Thus, the rate relationship $H_2/D_2$ exchange > $H_2$/RH exchange > RH dehydrogenation is predicted, as was experimentally observed. The tetracoordinated aluminum cluster ($x = 1$) reacts with the hydrocarbon by the same pathway as the tricoordinated aluminum cluster ($x = 0$) but with higher barriers for both steps; the barriers are reduced for the larger cluster $(HO)_2(H_2O)Al-O-Al(OH)_2(H_2O)$. The alternative pathway, forming the alkyl−oxygen adduct $(HO)_2Al(OH_2)_x(H)-O(R)H$ is too high in energy to compete. Examination of butane and isobutane establishes the reactivity order: prim C−H > *sec*-C−H > *tert*-C−H. For isobutane, essentially only methyl C−H cleavage should occur in the common first step for hydrogen exchange and dehydrogenation. In the second step, i.e., the $\beta$ C−H cleavage in the Al-alkyl intermediate, the reactivity order is *tert*-C−H > *sec*-C−H > prim C−H. "Broken lattice" zeolites and especially extraframework aluminum species present in steamed zeolites should be more reactive than the intact zeolite lattices. Thus, the mechanism is relevant for the activation of alkanes for acid-catalyzed conversions on these catalysts, which have insufficient acid strength to cleave C−H and C−C bonds by hydron transfer.

## Introduction

Active forms of aluminum oxide catalyze the exchange between elemental hydrogen and deuterium (through the exchange with the OH group of the catalyst)[1] and the H−D exchange of saturated hydrocarbons.[2] Both these reactions have been described as examples of acid−base catalysis.[2] More specifically, following the developments of concepts of superacid chemistry, the reactions of hydrocarbons on solid acids, particularly aluminosilicates, have been generally interpreted as involving the activation of reactant by hydron transfer to form carbocations, either as intermediates or as transition structures.[3]

The computational studies of the activation of C−H bonds in alkanes have usually attempted to describe the accepted mechanism and, therefore, sought mostly pathways based on hydron transfer.[4] Likewise, the dissociation of hydrogen on aluminum hydroxide clusters was assumed to involve a heterolytic cleavage of the hydrogen−hydrogen bond, with the hydron going to oxygen (basic site) and the hydride going to aluminum (acid site). MO calculations, both semiempirical[5] and ab initio without electron correlation,[6] following this postulated reaction pathway, were conducted.[5,6] We noted, however, deficiencies in those calculations and conducted a computational study of the dissociative chemisorption of hydrogen on coordinatively unsaturated aluminum centers. In it, standard ab initio and DFT calculations were conducted with large basis sets (6-31G* to 6-311++G**) and electron correlation (MP2 and B3LYP, respectively).[7] They showed that the chemisorption occurs through the interaction of $H_2$ with the aluminum until both hydrogen atoms are bonded to Al, after which one hydrogen migrates to an adjacent oxygen atom. Thus, the reaction is better described as metal ion catalysis, rather than acid−base catalysis.[7] It is thus similar to the chemisorption of hydrogen on noble metals, with the migration of one hydrogen to a different atom (oxygen), akin to the extensively discussed spillover process.[8]

Another notable result of our calculations was that tri-, tetra-, and pentacoordinated aluminum atoms were all active in hydrogen dissociation, with the reactivity decreasing in that order.[7] The earlier reports had considered only tri- and pentacoordinated aluminum as potentially reactive,[5,6] but at the level of theory and with the constraints imposed to the system in those studies, the pentacoordinated species did not chemisorb hydrogen.[6b] For some obscure reason, the tetracoordinated aluminum had been considered coordinatively saturated by the workers in the field. Considering the concentrations of sites on alumina surfaces (typically 30% tetracoordinated; much less, but sometimes observed, pentacoordinated; immeasurably low, if at all, tricoordinated),[9] we concluded that tetracoordinated

* To whom correspondence should be addressed. Phone: 412-624-7449. Fax: 412-624-9639. E-mail: dfarca@pitt.edu.

10.1021/jp013724l CCC: $22.00 
Published on Web 02/05/2002

sites are most likely responsible for the catalytic activity of $\gamma$- and $\eta$-alumina.[7] A tetracoordinated aluminum atom connected to a silicon by an oxygen bridge was also found to chemisorb hydrogen by this mechanism, but with a higher potential energy barrier (PEB) than the corresponding two-aluminum cluster, thus showing that extraframework aluminum species should be more active than the intact zeolite structures.[7]

We also conducted a computational search in which the reaction pathway was not presupposed for the reaction of small alkanes with the same aluminum oxide clusters.[10] As in the previous study, we have considered both one-aluminum clusters, $(HO)_3Al(OH_2)_x$ (**1**, $x = 0$; **2**, $x = 1$) and the two-aluminum cluster $(HO)_2(H_2O)Al-O-Al(OH)_2(H_2O)$ (**3**). Like there, we did not attempt to extrapolate from the clusters to models of the solid, for instance by the application of periodic boundary conditions. Such an approach assumes that the entire unit cell, including the reactant, is periodically repeated,[11] which is not expected of catalytic alumina. Moreover, embedding the structural moiety into the surface should affect more the energies of reaction and activation than the mechanism of reaction and relative reactivity of sites of different structure, which were our goals. It was important to conduct our calculations at a satisfactory level of theory, with a large basis set. Also, it was reported that the errors from neglect of long-range electrostatic effects are less important than the errors from inadequate optimization of structures.[12] Furthermore, experimental activation energies of catalytic reactions conducted at high temperatures are not necessarily chemistry-derived. One runs the risk of trying to duplicate computationally activation energies of reactions that are transport-limited! A comparison of the results obtained for the double clusters with the results obtained for the one-aluminum clusters allows to establish the effect of the neighboring aluminum center on the chemisorption at the reactive aluminum center. The small clusters are, of course, appropriate for modeling the extraframework aluminum species present in steamed zeolites.[13]

Finally, we have examined the relative reactivity of primary, secondary, and tertiary C−H bonds, using as model reactants propane, butane, and isobutane. The results are reported in full, below.

## Computational Method

Most calculations were conducted with the program Gaussian 98;[14] only the STQN calculations, for which Gaussian 98 did not perform well, were conducted with the Gaussian 94 program,[15] all in the same manner as in the study of hydrogen chemisorption.[7] Standard ab initio calculations[16] with electron correlation and sufficiently large basis sets were not possible for the large systems studied in this work. Therefore, all geometry optimizations were conducted with the DFT-B3LYP method[17] and the 6−31G** basis set, with some MP2(FC)/6-31G** geometry optimizations run for comparison. Frequency analyses, giving also the zero-point energy corrections (ZPE),[16c] were conducted at the same level of theory. Transition structure searching by the STQN (synchronous transit-guided quasi Newton) method[18] and reaction pathway identification by the intrinsic reaction coordinate (IRC)[19] tracking were conducted in the standard manner.

No corrections were made for the basis set superposition error (BSSE).[20] They would affect mostly the energies of the physisorbed complexes and would be, therefore, inconsequential.

The computer program Molden[21] was used for the assignment of calculated frequencies to specific vibrations. The projections of structures shown in the figures were generated with the program XMol.[22]

## Results and Discussion

**1. Reaction of Propane on the Tricoordinated Aluminum Cluster.** The geometry of the aluminum hydroxide reactant **1** was chosen based on the consideration that transitional aluminas are formed by the calcination of a hydrated aluminum oxide, like boehmite. One can consider that the bulk of the solid is already set to a significant extent at the boehmite stage and the structural reorganization upon calcination affects mostly the surface.[23] We optimized, therefore, the geometry of the hydrated cluster **2** as the starting point and then removed the extra water molecule to obtain the corresponding reactive (coordinatively unsaturated) cluster **1** (eq 1).[7]

Two types of constraints were applied in our study of the reaction of hydrogen with **1**. In the first (A), the O1−O2−Al−O3 dihedral angle was kept constant at the same value as in **2** and the other geometrical parameters were optimized. In the alternative mode (B), the outer atoms of **1** were frozen in the position they had in the hydrated cluster **2** and the geometry of the central fragment (the Al $(-O-*)_3$ group) was optimized. The reaction proceeded in the same way in either mode and the PEB for the formation of the chemisorbed complex was the same for both.[7a] The reaction of **1** with the larger molecule, propane, was investigated only in mode A. Because there is no evidence that tricoordinated aluminum species exist at all in active alumina or zeolites, we concentrated on the reaction of the tetracoordinated aluminum cluster **2**, on which no geometry constraints were placed (see below). The reaction pathways calculated for clusters **1** and **2** were the same in every detail. Thus, even if the energy barriers for the reaction of **1** along pathways A and B were different, that finding would not affect the conclusions. Moreover, the reaction pathway for the reaction of the C−H bonds was in each case the same as that for the reaction of the H−H bond, where the same PEB was found for modes A and B.[7a]

$$\underset{\mathbf{2}}{(HO)_3Al-OH_2} \rightarrow \underset{\mathbf{1}}{(HO)_3Al} + H_2O \qquad (1)$$

The calculations have established the existence of a weak complex of **1** with propane (physisorbed propane), of the van der Waals type (**4**), 4 kcal/mol[24] more stable than the isolated reactants (without a BSSE correction). Two kinds of chemisorption products were identified, with alkyl-aluminum bond (**5**) and with alkyl-oxygen bond (**6**), illustrated for **1** by eqs 2 and 3, respectively, with $x = 0$. For each type of complex, the catalyst cluster can cleave either a primary or a secondary C−H bond (series **a** and **b** in eqs 2 and 3).

$$\underset{\mathbf{1}\ (x=0),\ \mathbf{2}\ (x=1)}{(HO)_3Al(OH_2)_x} + PrH \rightarrow \underset{\mathbf{5}\ (x=0),\ \mathbf{8}\ (x=1)}{(HO)_2Al(OH_2)_{x+1}(R)} \qquad (2)$$

$$\mathbf{1}, \mathbf{2} + PrH \rightarrow \underset{\mathbf{6}\ (x=0),\ \mathbf{9}\ (x=1)}{(HO)_2Al(OH_2)_x(H)\text{-}O(R)H} \qquad (3)$$

**a**: R = 1-Pr **b**: R = $CHMe_2$

The transition structure for the chemisorption step on the alkyl-aluminum pathway, identified by the STQN method,[18] was similar to the transition structure for hydrogen chemisorption. The imaginary frequency was identified as the bending of the Al−H bond toward O, that is, the migration of hydrogen from aluminum to oxygen.[21] The transition structure (TS1) for

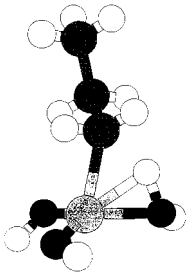

**Figure 1.** Transition structure (TS1) for the chemisorption of propane (methyl C−H cleavage) by C−Al bonding, on a tricoordinated aluminum cluster (**1** → **5a**).

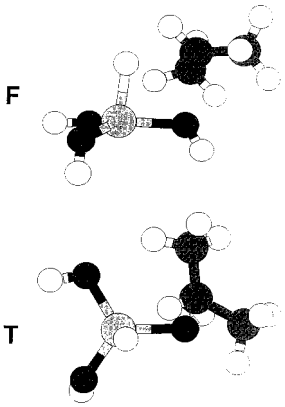


**Figure 2.** Transition structure (TS1) for the chemisorption of propane (methylene C−H cleavage) by C−O bonding, on a tricoordinated aluminum cluster (**1** → **6b**). F = front view, T = top view.

chemisorption on the tricoordinated cluster, **1** → **5a**, is shown in Figure 1.[22] IRC tracking verified the transition structures. In the transition structure, the distance of the migrating hydrogen to the oxygen is 20−25% longer than the normal O−H bond, whereas its distance to aluminum is only 10−15% longer than the normal Al−H bond. Most importantly, however, the Al−H distance is even shorter prior to the transition state and then increases, whereas the O−H distance decreases throughout the process. Thus, the reaction mechanism consists of the insertion of aluminum into the C−H bond, followed by hydrogen migration from Al to O, just like for hydrogen chemisorption.[7]

The alternative, alkyl−oxygen, pathway **1** → **6b** (eq 3), was closer to a concerted four-center process. Its transition structure, TS1, is shown in two projections in Figure 2. The C−O bond formation seemed to lag somewhat behind the Al−H bond formation. The charge distribution (Mulliken population analysis) showed that the reacting carbon acquired a positive charge on the pathway of eq 3 (**1** → **6b**); therefore, the corresponding reaction of a primary C−H bond (**1** → **6a**) should be of significantly higher energy and was not investigated.

The products of chemisorption on either pathway can react further, to form hydrogen and propene. It is well established that alkenes can be hydrogenated and alkanes dehydrogenated on alumina and on silica−alumina catalysts.[25] Locating a transition structure for the elimination from the O-alkyl complex **5** was a trivial matter, as the reaction proceeded smoothly over a cyclic transition structure (TS2, Figure 3),[22] in a process reminiscent of the thermal elimination of esters, leading to propene and the complex with chemisorbed hydrogen (adduct) on the aluminum cluster (eq 4). The hydrogen was transferred from C$\beta$ to another oxygen atom. It was much more difficult, however, to map the reaction pathway for the elimination from the alkyl-aluminum complexes **5a** and **5b**. The STQN method was not successful, because we did not have the structure of

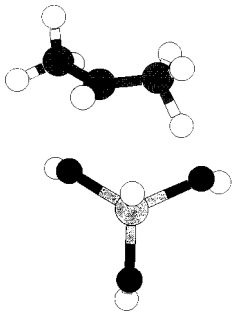

**Figure 3.** Transition structure (TS2) for the elimination of propene from the alkyl-oxygen adduct, **6b** (top view).

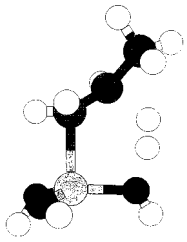

**Figure 4.** Transition structure (TS2) for the elimination of propene from the alkyl-aluminum adduct, **5a**.

the final state of the reaction. We were able to find the transition structure by standard Berny optimization of various candidates. The structure that we obtained was confirmed by IRC[19] tracking, which also gave the structure of the elimination product. The latter was a $\pi$ complex of propene with the aluminum cluster (**7**), formed together with a hydrogen molecule, which is also physisorbed on the cluster, but only weakly (eq 5). The coordinatively unsaturated aluminum atom binds much stronger to a carbon−carbon double bond ($\Delta E = -11.9$ kcal/mol for the complexation of propene to give **7**) than to a molecule of hydrogen ($\Delta E = -1.78$ kcal/mol for the complexation of $H_2$ to **1**, at B3LYP/6-31G** without ZPE correction).[7a] The former is a $\pi$ complex, and the latter is a van der Waals complex. There was much less cleavage of the Al−C bond than of the C−H bond at the transition state of the second step (TS2, shown in Figure 4, for the decomposition of **5a**).[22]

$$\mathbf{6b}, \mathbf{9b} \rightarrow \text{H-Al(OH)}_2(\text{-OH}_2)_{x+1} + \text{Me-CH=CH}_2 \quad (4)$$

$$\mathbf{5a}, \mathbf{5b}, \mathbf{8a} \rightarrow (\text{HO})_3(\text{H}_2\text{O})_x\text{Al-}\overset{\text{CH}_2}{\underset{\text{CHMe}}{\|}} + \text{H}_2 \quad (5)$$

**7** (x = 0), **10** (x = 1)

For comparison, we also examined the reaction coordinate for the alkyl-aluminum chemisorption pathway **1** → **5a** by MP2/6-31G** geometry optimization. The structures obtained were essentially the same, confirming the conclusion of the study of hydrogen chemisorption, in which the equivalency of the MP2 and B3LYP calculations was thoroughly tested.[7]

The energies of intermediates and products, relative to the starting materials, are shown in Table 1. As seen in the table, the alkyl−aluminum complexes were found more stable than the alkyl-oxygen complex **6b** by 6.1 kcal/mol (**5a**) and 3.8 kcal/mol (**5b**). The reaction coordinates for the two pathways were quite different. Thus, the chemisorbed complexes of eq 2 (Al−C bonding) represented shallow energy minima with low barriers (1−2 kcal/mol) for the return to reactants. The rate-determining step for the dehydrogenation was the elimination from **5**. About half of the energy barrier for dehydrogenation came from the endothermicity of the reaction (29.2 kcal/mol for the conversion

**TABLE 1: Calculated Relative Energies of Intermediates, Products, and Transition Structures for the Reaction of Propane with the Aluminum Hydroxide Clusters 1, 2, and 11[a]**

| reaction pathway | physisorbed reactant [b] | TS1 | chemisorbed complex | TS2 | physisorbed product(s)[b] | isolated products |
|---|---|---|---|---|---|---|
| | | | A. Tricoordinated Aluminum Cluster (**1**) as Catalyst | | | |
| Al−$CH_2$Et[c] | −4.01 | 32.19 | 31.24 | 57.10 | 17.63 | 29.23 |
| Al−CH(Me)$_2$[d] | −4.01 | 35.14 | 33.54 | 62.41 | 17.63 | 29.23 |
| Al−CH(Me)$_2$[e] | −6.33 | 33.59 | 31.50 | | | |
| O−CH(Me)$_2$[f] | −4.01 | 72.31 | 37.34 | 70.35 | 46.65[g] | 29.23[h] |
| | | | B. Tetracoordinated Aluminum Cluster (**2**) as Catalyst | | | |
| Al−$CH_2$Et [i] | −1.93 | 43.95 | 25.59 | 74.20 [j]<br>72.21[k] | 26.56 | 29.23 |
| Al−CH(Me)$_2$[l] | −1.93 | *m* | | | | |
| O−CH(Me)$_2$[n] | −1.93 | 82.22 | 32.28 | 75.98[o]<br>67.31[p] | 43.77 | 29.23[q] |
| | | | C. Two-Aluminum (Both Tetracoordinated) Cluster (**11**) as Catalyst | | | |
| Al−$CH_2$Et[r] | −3.77 | 37.02 | 20.89[s] | 67.01[t] | 20.49 | 29.23 |

[a] B3LYP/6-31G**//B3LYP/6-31G** + ZPE, kcal/mol, relative to the isolated starting materials (**1**, **2**, or **11** and PrH). [b] The values in this column are affected by basis set superposition errors. [c] **1** → **5a**, eq 2, then eq 5. [d] **1** → **5b**, eq 2, then eq 5. [e] MP2(FC)/6-31G**//MP2(FC)/6-31G** values. [f] **1** → **6b**, eq 3, then eq 4. [g] Propene physisorbed on the $(HO)_2AlH-OH_2$ cluster. [h] 44.98 kcal/mol if $(HO)_2AlH-OH_2$ is a product. As the energy for the latter was not ZPE-corrected, the number is only orientative. [i] **2** → **8a**, eq 2, then eq 5. [j] $d$(Al−$OH_2$) = 2.11 Å, as in the chemisorbed complex, **8a** (see text). [k] $d$(Al−$OH_2$) = 2.31 Å, see text. [l] **2** → **8b**, eq 2. [m] Decomposition to **5b** occurred. [n] **2** → **9b**, eq 3, then eq 4. [o] $d$(Al−$OH_2$) = 2.00 Å, as in the chemisorbed complex, **9b** (see text). [p] $d$(Al−$OH_2$) = 2.20 Å, see text. [q] 48.14 kcal/mol, if $(H_2O)_2AlH(-OH)_2$ is a product.[r] eq 6. [s] Adduct **12**. [t] $d$(Al−$OH_2$) = 2.136 Å, as in the chemisorbed complex, **12** (see text).

**SCHEME 1: Reaction Coordinate for Propane Dehydrogenation (Aluminum−Alkyl Pathway, Eqs 1 and 5, $x = 0$, Path a)**

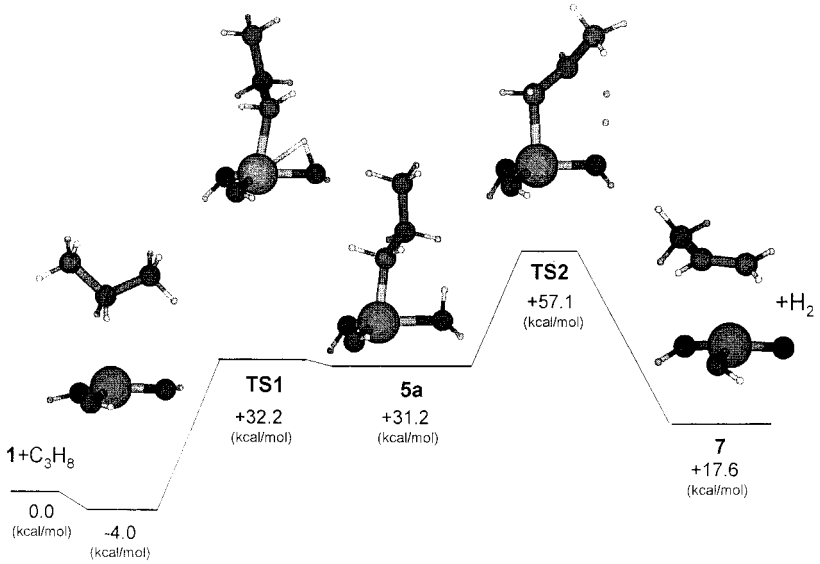


of propane to propene at B3LYP/6-31G** with ZPE correction). Both the chemisorbed intermediate and the two transition structures were lower in energy for the reaction of the primary C−H (**a**). This result can be rationalized by electronic factors, because the negative electric charge at the reacting carbon increased during the chemisorption (it was highest in the transition structure), but a contribution from steric factors needs also to be considered.

Contrastingly, the mechanism of eq 3 (O-alkyl pathway) has high energy barriers on both sides of the chemisorbed intermediate, with the barrier for the first step being slightly higher (by 2 kcal/mol). It can be safely concluded that both hydrogen exchange and dehydrogenation/hydrogenation occur exclusively by the alkyl−aluminum pathway. The potential energy profile of the lowest energy pathway (over **5a**) for propane dehydrogenation/propene hydrogenation on the aluminum cluster **1** is presented in Scheme 1. The energy shown for the product, **7**, includes the stabilizing interaction with the hydrogen molecule (−0.6 kcal/mol, again without BSSE correction).

A comparison between an alkyl-metal and an alkyl-oxygen pathway was recently reported for the dehydrogenation of ethane by the gallium atom of a cluster in which a $H_2Ga$ moiety was bonded to two tricoordinated (oxonium) oxygens of an aluminosilicate model.[26] The gallium-bonded hydrogens were involved in the reaction (a Ga−H bond was broken upon ethane chemisorption and a Ga−H bond was formed in the elimination step). The alkyl-metal pathway was also found the lower-energy process in that system.[26]

**2. Reaction of Propane on Tetracoordinated One-Aluminum and Two-Aluminum Clusters.** Because a tetracoordinated aluminum atom inherently has less flexibility than a tricoordinated atom, the geometry optimizations were conducted without any restraints. No chemisorbed complex of formula **8b** (eq 2) was identified in this way, however, because a water molecule dissociated and the reaction product was **5b**, described above. If the catalytic center was part of a solid, the lattice rigidity would prevent Al−O dissociation; therefore, chemisorption accompanied by a relaxation of the lattice

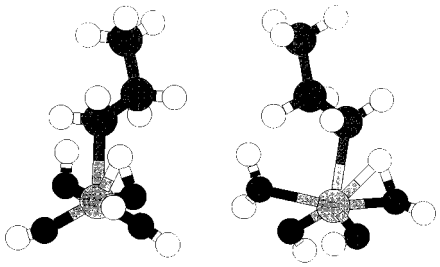


**Figure 5.** Transition structure (TS1) for the chemisorption of propane (methyl C−H cleavage) by C−Al bonding, on a tetracoordinated aluminum cluster (**2** → **8a**). F = front view, S = side view.

(increase of the O−Al bond length) should occur. As both the chemisorbed intermediate and the barrier for its formation were shown in the reaction with cluster **1**, above, to be higher in energy for the secondary C−H bond than for the primary C−H bond, the formation and reaction of **8b** were not investigated further.

The reaction of the tetracoordinated aluminum cluster **2** was mechanistically the same as the reaction of the tricoordinated cluster, **1**, both for the alkyl-aluminum pathway (**2** → **8a**, eq 2) and for the alkyl-oxygen pathway (**2** → **9b**, eq 3). The transition structure for chemisorption (TS1) of propane on **2** by eq 2 is shown in Figure 5. In the second step of the reaction, both **8a** and **9b** eliminated easier water than propene. Depending upon the rigidity of the lattice around the aluminum center, three possibilities have to be considered. (1) If the system was fully flexible, the elimination would occur as for the tricoordinated aluminum cluster **1**, with the energy barriers calculated above, after which the broken aluminum−oxygen bond would be reformed. (2) If the lattice was rigid, the Al−O bond length would be preserved throughout elimination from both **8a** and **9b**; the calculation with this assumption provides the highest limit for the decomposition energy barrier. (3) For a lattice endowed with some local flexibility (the most likely case), the Al−O would be lengthened to some extent at the transition state for elimination; the energy barrier would be lower than in case 2 but not necessarily higher than in case 1, because secondary interactions assisting the elimination might exist. Optimization of the transition structures for the elimination steps from **8a** and **9b** were conducted for Al−$OH_2$ distances frozen as in the chemisorbed complexes (case 2) and longer by 0.2 Å (case 3).

The calculated energies are shown in the second section of Table 1. It can be seen that the calculated PEB for the rate-determining steps of both the alkyl−aluminum pathway (elimination step) and the oxygen−aluminum pathway (the propane chemisorption step) were higher than in the reaction catalyzed by the tricoordinated aluminum cluster, **1**. The same relationship between tri- and tetracoordinated aluminum clusters was found for hydrogen chemisorption.[7] The complexation of propene by the tetracoordinated cluster is weak (ca 3 kcal/mol). Therefore, structure **10** in eq 5 should be considered as a van der Waals complex.

The chemisorption and elimination by the alkyl−aluminum pathway were also examined for the double (tetracoordinated-tetracoordinated) cluster, **11**. The geometry of this catalyst was generated in our previous work by the optimization of the hydrated species, $(H_2O)_2Al(OH)_2-O-Al(OH)_2(H_2O)$, and removal of a molecule of water.[7b] The oxygens in the terminal hydroxy groups (drawn in bold letters in eq 6) were frozen, and the geometry of the dehydrated cluster was optimized with these constraints, modeling the anchoring of the active site onto the lattice.[7b] The same constraints were kept in the optimization of the species resulting from the interaction of **11** with propane (eq 6).

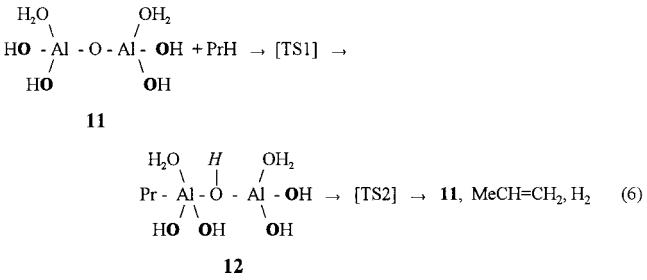


(6)

In the complex with chemisorbed propane, the hydrogen cleaved from a carbon went to the bridging oxygen, as expected.[7b] Otherwise, the reaction mechanism was the same as for the one-aluminum cluster **2**, and the Al−O bond also cleaved easier than the Al−C bond in the decomposition of the adduct **12**. Therefore, the transition structure for the elimination step (TS2) was optimized with the Al−$OH_2$ bond length frozen as in **12** (2.136 Å), to obtain the high limiting value of the potential energy barrier for elimination (option 2, above). The elimination is the rate-determining step of propane dehydrogenation on the dialuminum oxide-hydroxide cluster as well. Again as expected,[7b] all of the species along the reaction coordinate (intermediates and transition structures) are lower in energy for the two-aluminum cluster than for the one-aluminum cluster as catalyst (third section of Table 1).

On the basis of the close similarity observed in every point between the previous results on hydrogen dissociation[7] results and the present data on propane dehydrogenation, we can expect that a silicon−aluminum oxide model (hydrated) should also catalyze the latter reaction, but the energy barriers for the reactions should be higher than for the all-aluminum clusters.[7b] This prediction agrees with the comparative study by Holm and Blue of ethylene hydrogenation at 500 °C on alumina and silica−alumina catalysts.[25a]

**3. Reaction of Butanes on the Tricoordinated Aluminum Cluster.** The results shown above indicated that primary C−H bonds are more reactive than secondary C−H bonds toward the coordinatively unsaturated aluminum centers. To obtain further data on the relative reactivity of C−H bonds, we studied the reaction of butane (BuH) and isobutane (*i*-BuH) with cluster **1** on the alkyl−aluminum pathway (corresponding to Equations 2 and 5 for propane). The results are given in Table 2.

It is seen that the predicted relative reactivity of primary and secondary C−H bonds is the same for BuH as for propane. Moreover, the size of the hydrocarbon has little effect. Chain branching seems to have little effect on the alkane chemisorption (ca 1 kcal/mol difference between methyl C−H reactivity in BuH and *i*-BuH), but the elimination from the primary R−Al species has a lower barrier for the branched hydrocarbon than for the linear isomer.

A tertiary C−H bond of *i*-BuH is predicted to be less reactive than a secondary C−H bond of BuH by 3 kcal/mol for the dissociative chemisorption and by 5 kcal/mol for the elimination. An internal comparison of hydrogen atoms in *i*-BuH reveals a preference for the reaction involving initial insertion into a primary C−H bond over insertion into the tertiary C−H bond by 5.5 kcal/mol for dissociative chemisorption and by 13 kcal/mol for elimination.

**4. Implications for Catalysis Mechanism.** The calculations show that the hydrogen exchange with the catalyst has a much

**TABLE 2: Calculated Relative Energies of Intermediates, Products, and Transition Structures for the Reaction of Butane and Isobutane with the Aluminum Hydroxide Cluster 1[a]**

| reacting bond | physisorbed reactant[b] | TS1 | chemisorbed complex | TS2 | physisorbed product(s)[b] | isolated products |
|---|---|---|---|---|---|---|
| $PrCH_2-H$[c] | −3.33 | 32.07 | 31.09 | 57.39 | 17.71 | 31.40 |
| EtMeCH−H[c] | −3.33 | 35.88 | 34.65 | 62.45 | 17.71 | 31.40 |
| EtMeCH−H [d] | −3.33 | 35.88 | 34.65 | 60.26 | 14.09[e] | 25.68[e,f] |
| $(Me)_2CHCH_2-H$[g] | −4.14 | 33.26 | 31.63 | 54.25 | 12.76 | 30.62 |
| $Me_3C-H$ [g] | −4.14 | 38.82 | 35.09 | 67.31 | 12.76 | 30.62 |

[a] B3LYP/6-31G**//B3LYP/6-31G** + ZPE, kcal/mol, relative to the isolated starting materials (**1** and BuH or *i*-BuH). [b] The values in this column are affected by BSSE. [c] Reaction forming 1-butene. [d] Reaction forming 2-butene. [e] The value given is for *trans*-2-butene. [f] The value calculated for *cis*-2-butene is 28.52. [g] Reaction forming isobutene.

lower potential energy barrier than the elimination, for all clusters and for all types of C−H bonds. Therefore, it should be much faster than the elimination. We note that in the reaction of BuH-$d_{10}$ with HZSM-5 at 400−550 °C, H−D exchange was at least 1 order of magnitude faster than dehydrogenation and cracking.[27] The chemisorption of hydrogen on the same clusters was found to have a smaller potential energy barrier[7] than the chemisorption of the alkane, which is in perfect agreement with the experimental results.[28] Therefore, the $H_2$/catalyst exchange should be the fastest process. Indeed, this rate relationship was found in a study of the reaction of tritium gas with toluene and with hexane on three zeolites.[29]

The difference in reactivity, prim C−H ≫ *tert*-C−H (with *sec*-C−H between) is clearly apparent for *i*-BuH, where it is compounded by a statistical factor of 9. Experimentally, no *tert*-C−H exchange was observed in isobutane at temperatures at which the methyl hydrogens exchanged readily.[4d,30] In the comparison of the primary C−H bonds in BuH and *i*-BuH, we must note that in the interaction with coordinatively unsaturated aluminum sites on an irregular surface, steric effects may determine the relative reactivity.

Mechanistically, our calculations show that the hydrogen exchange[2,4,27,30] and elimination reactions[25] of an alkane on materials containing $Al(O-)_n$ sites, with $n = 3$ and 4, are examples of metal ion catalysis.[7] The cleavage of H−H and C−H bonds by insertion of metal atoms and ions (metal and metal ion catalysis) has been well-known for heavy metals, particularly noble metals, but it was not considered for aluminum. An increase in reactivity for "broken lattices" of zeolites and a role for extraframework aluminum species of steamed zeolites in hydrogen and alkane activation is predicted by this mechanism.

Alkane activation by solid acids, particularly zeolites, was described as involving hydron transfer to C−H[3a] and C−C bonds,[3b] the same as for the liquid superacids HCl−$AlCl_3$ (or, rather, $H_2O-AlCl_3$),[31] HF−$SbF_5$,[32] and HF−$TaF_5$.[33] It was, indeed, claimed that zeolites, among others, are solid superacids.[34] Computational descriptions based on this reactivity model have been published.[4,35] The superacidity of solids has, however, been contested.[36] It was shown that solids are intrinsically much weaker acids than liquids of similar structure.[36b] In particular, the zeolite HZSM-5, for which the mechanisms involving hydronated alkanes with pentacoordinated carbon (carbonium ions) and cleavage of sigma bonds by acidolysis were put forward,[3] was shown to be much weaker than trifluoromethanesulfonic acid.[37] The latter is a weak superacid, capable of isomerizing and cracking alkanes, but the initiation appears to be by oxidation.[38] Activation of alkanes by zeolites through hydron transfer is, therefore, highly questionable.

Alternatively, a hydride abstraction by a surface Lewis acid site has been proposed for alkane activation.[30a] It was noted, however, that hydride abstraction from alkanes does not occur even with the much stronger Lewis acid, $SbF_5$.[39]

A reverse heterolysis of C−H bonds by aluminum oxide catalysts was also proposed. Thus, the reaction of methane with aluminum hydroxide was described as a heterolytic reaction with an acid−base pair on the surface, with the hydron going to the negative oxygen and a methyl anion to the metal.[40] It was computationally modeled by a process involving a concerted four-center reaction.[41] Formation of alkyl anions requires extremely high basicities, which cannot be expected of either the bridging oxygens or the hydroxylic oxygens present in active alumina. The insertion of the metal ion into the C−H bonds, predicted by the calculations, liberates the mechanistic model from such improbable acid−base reactions. It is noteworthy that the transition structure calculated (HF/6-31G) for the methane chemisorption along the postulated reverse C−H heterolysis pathway is somewhat similar to the one that we find for propane, but the critical feature that the hydrogen of the C−H bond to be broken has a bonding interaction with aluminum before migrating to oxygen was not evidenced in that study.[41]

Initiation of alkane reactions on solid acids by a one-electron oxidation has also been proposed.[42] Dehydrogenation on tricoordinated and especially tetracoordinated aluminum centers by the mechanism uncovered here represents an alternative alkane activation mechanism. An easier dehydrogenation on all-aluminum rather than on aluminum−silicon hydroxide clusters explains the effect of extraframework aluminum species in steamed zeolites on catalytic activity. It follows that for mechanistic studies on zeolites, the rigorous and sensitive identification and quantification of extraframework aluminum species is essential. Unfortunately, no good analytical procedure exists. The existence of extraframework aluminum species is normally concluded from the observation of hexacoordinated aluminum in the sample. The hexacoordinated aluminum is *inactive*, however. Moreover, for the cluster sizes possible inside the cavities, hexacoordination can be achieved only with molecules of water as ligands. The latter would be lost on calcination. Then, *the hexacoordinated aluminum species observed in steamed zeolites after thermal activation must be present on the external surface of crystals*. The active aluminum is tetracoordinated, present most likely as assemblies of two (or more) adjacent tetracoordinated aluminum atoms,[43] in agreement with our findings here. Therefore, it is hardly distinguishable by $^{27}Al$ NMR from the lattice aluminum.

The one-electron transfer and aluminum insertion might occur competitively. In either case, the critical intermediate is a bonded or complexed olefin. In the reactions on aluminosilicates, the barrier for reaction of the olefin with the acid site is lower than the barrier for hydrogenation; therefore, a cationic-type (cationoidic) reaction ensues. At high temperatures and low pressure, olefin products desorb from the catalyst. In experiments with the feed as liquid and at lower temperatures (120−160 °C),

however, only saturated hydrocarbons were desorbed from the catalyst, as isomerization and disproportionation products, but they were formed entirely via olefinic intermediates.[44] The isomerization of hexane under the same conditions on acid mordenite also cannot be rationalized by the clasical mechanism of sigma bond acidolysis and carbocationic rearangement.[45] All of these findings are consonant with the present calculations.

**Acknowledgment.** Support of our research of strong acid catalysis by the Grant CTS-9812704, from NSF, is gratefully acknowledged. A grant of supercomputer time was obtained from the National Center for Supercomputing Applications (NCSA) in Urbana, IL.

## References and Notes

(1) (a) Taylor, H. S.; Diamond, H. *J. Am. Chem. Soc*. **1935**, *57*, 1256. (b) Lee, J. K.; Weller, S. W. *Anal. Chem*. **1958**, *30*, 1057. (c) Hall, W. K.; Leftin, H. P.; Cheselske, F. J.; O'Reilly, D. E. *J. Catal*. **1963**, *2*, 506. (d) Hall, W. K.; Lutinski, F. E. *J. Catal*. **1963**, *2*, 518. (e) Carter, J.; Lucchesi, P.; Corneil, P.; Yates, D. J. C.; Sinfelt, J. H. *J. Phys. Chem*. **1965**, *69*, 3070. (f) Garrett, B. R. T.; Rooney, J. J. *J. Chem. Soc., Perkin Trans. 2* **1974**, 960.

(2) For references, see: Yoshida, S. In *Theoretical Aspects of Heterogeneous Catalysis*; Moffat, J. B., Ed.; Van Nostrand Reinhold: New York, 1990; p 506.

(3) (a) Haag, W. O.; Dessau, R. M. *Proc. 8th Intl. Congr. Catal., Berlin 1984*, vol. 2; Dechema: Frankfurt-am Main, 1984; p 305. (b) Abbot, J.; Wojchechowski, B. *Ind. Eng. Chem. Prod. Res. Dev*. **1985**, *24*, 501. (c) Giannetto, G.; Sansare, S.; Guisnet, M. *J. Chem. Soc., Chem. Commun*. **1986**, 1302 (d) Hall, W. K.; Lombardo, E. A.; Engelhardt, J. *J. Catal*. **1989**, *115*, 611. (e) See the discussion in Fărcaşiu, D.; Lukinskas, P. *Rev. Roumaine Chim*. **1999**, *44*, 1091.

(4) (a) van Santen, R. A.; Kramer, G. J. *Chem. Rev*. **1995**, *95*, 637. (b) Kazansky, V. B.; Frash, M. V.; van Santen, R. A. *Appl. Catal., A* **1996**, *146*, 225. (c) Rigby, A. M.; Kramer, G. J.; van Santen, R. A. *J. Catal*. **1997**, *170*, 1. (d) Bates, S. P.; van Santen, R. A. *Adv. Catal.* **1998**, *42*, 1. (e) Zygmunt, S. A.; Curtiss, L. A.; Iton, L. E. *Abstracts, 16th Meeting of the North American Catalysis Society, Boston, MA, June 2*, **1999**, *119*. (f) Esteves, P. M.; Nascimento, N. A. C.; Mota, C. J. A. *J. Phys. Chem. B* **1999**, *103*, 10417.

(5) Zelenovskii, V. M.; Zhidomirov, G. M.; Kazanskii, V. B. *Zh. Fiz. Khim*. **1984**, *58*, 1788.

(6) (a) Senchenya, I. N.; Kazanskii, V. B. *Kinet. I Katal*. **1988**, *29*, 1331. (b) Ioka, F.; Sakka, T.; Ogata, Y.; Iwasaki, M. *Can. J. Chem*. **1993**, *71*, 663.

(7) (a) Fărcaşiu, D.; Lukinskas, P. *J. Phys. Chem. A* **1999**, *103*, 8483. (b) Lukinskas, P.; Fărcaşiu, D. *Appl. Catal. A* **2001**, *209*, 193.

(8) (a) Khoobiar, S. *J. Phys. Chem*. **1964**, *68*, 411. (b) Robell, A. J.; Ballou, E. V.; Boudart, M. *J. Phys. Chem*. **1964**, *68*, 2748. (c) Vannice, M. A.; Neikan, W. C. *J. Catal*. **1971**, *20*, 260. (d) Levy, R. V.; Boudart, M. *J. Catal*. **1974**, *32*, 304. (e) Fleisch, T.; Aberman, R. *J. Catal*. **1977**, *50*, 268. (f) Conner, W. C., Jr.; Pajonk, G. M.; Teichner, S. J. *Adv. Catal*. **1986**, *34*, 1. (g) Musso, J. C.; Parera, J. M. *Appl. Catal*. **1987**, *30*, 81.

(9) (a) Coster, D.; Blumenfeld, A. L.; Fripiat, J. J. *J. Phys. Chem*. **1994**, *98*, 6201. (b) Lee, M.-H.; Cheng, C.-F.; Heine, V.; Klinowski, J. *Chem. Phys. Lett*. **1997**, *265*, 673.

(10) Preliminary communication: Fărcaşiu, D.; Lukinskas, P. *Chem. Commun*. **2001**, 77.

(11) Schwarz, K.; Nusterer, E.; Blöchl, P. E. *Catal. Today* **1999**, *50*, 501.

(12) Sauer, J.; Ugliengo, P.; Garrone, G.; Saunders, V. R. *Chem. Rev*. **1994**, *94*, 2095.

(13) Shertukde, P. V.; Hall, W. K.; Marcelin, G. *Catal. Today* **1992**, *94*, 491.

(14) Frisch, M. J.; Trucks, G. W.; Schlegel, H. B.; Scuseria, G. E.; Robb, M. A.; Cheeseman, J. R.; Zakrzewski, V. G.; Montgomery, J. A., Jr.; Stratmann, R. E.; Burant, J. C.; Dapprich, S.; Millam, J. M.; Daniels, A. D.; Kudin, K. N.; Strain, M. C.; Farkas, O.; Tomasi, J.; Barone, V.; Cossi, M.; Cammi, R.; Mennucci, B.; Pomelli, C.; Adamo, C.; Clifford, S.; Ochterski, J.; Petersson, G. A.; Ayala, P. Y.; Cui, Q.; Morokuma, K.; Malick, D. K.; Rabuck, A. D.; Raghavachari, K.; Foresman, J. B.; Cioslowski, J.; Ortiz, J. V.; Stefanov, B. B.; Liu, G.; Liashenko, A.; Piskorz, P.; Komaromi, I.; Gomperts, R.; Martin, R. L.; Fox, D. J.; Keith, T.; Al-Laham, M. A.; Peng, C. Y.; Nanayakkara, A.; Gonzalez, C.; Challacombe, M.; Gill, P. M. W.; Johnson, B. G.; Chen, W.; Wong, M. W.; Andres, J. L.; Head-Gordon, M.; Replogle, E. S.; Pople, J. A. *Gaussian 98*, revision A.9; Gaussian, Inc.: Pittsburgh, PA, 1999.

(15) Frisch, M. J.; Trucks, G. W.; Schlegel, H. B.; Gill, P. M. W.; Johnson, B. G.; Robb, M. A.; Cheeseman, J. R.; Keith, T.; Petersson, G. A.; Montgomery, J. A.; Raghavachari, K.; Al-Laham, M. A.; Zakrzewski, V. G.; Ortiz, J. V.; Foresman, J. B.; Cioslowski, J.; Stefanov, B. B.; Nanayakkara, A.; Challacombe, M.; Peng, C. Y.; Ayala, P. Y.; Chen, W.; Wong, M. W.; Andres, J. L.; Replogle, E. S.; Gomperts, R.; Martin, R. L.; Fox, D. J.; Binkley, J. S.; Defrees, D. J.; Baker, J.; Stewart, J. P.; Head-Gordon, M.; Gonzalez, C.; Pople, J. A. *Gaussian 94*, revision D.3; Gaussian, Inc.: Pittsburgh, PA, 1995.

(16) (a) Pople, J. A. *Acc. Chem. Res*. **1970**, *3*, 217. (b) Pople, J. A. *Int. J. Mass Spectrom. Ion Phys.* **1976**, *19*, 89. (c) Hehre, W. J.; Radom, L.; Schleyer, P. v. R.; Pople, J. A. *Ab initio Molecular Orbital Theory*; Wiley-Interscience: New York, 1986.

(17) (a) Hohenberg, P.; Kohn, W. *Phys. Rev*. **1964**, *136*, B864. (b) Kohn, W.; Sham, L. *Phys. Rev.* **1965**, *140*, A1133. (c) Parr, R. G.; Yang, W. *Density Functional Theory of Atoms and Molecules*; Oxford University Press: New York, 1989. (d) Becke, A. D. *J. Chem. Phys.* **1993**, *98*, 5648.

(18) Peng, C.; Schlegel, H. B. *Isr. J. Chem*. **1993**, *33*, 449.

(19) Gonzales, C.; Schlegel, H. B. *J. Phys. Chem*. **1989**, *90*, 2154.

(20) Chalasiński, G.; Gutowski, M. *Chem. Rev*. **1988**, *88*, 943.

(21) Schaftenaar, G. *MOLDEN. A Portable Electron Density Program* Available at: ftp ftp.caos.kun.nl. Name: anonymous.

(22) XMol, version 1.3.1; Minnesota Supercomputing Center, Inc.: Minneapolis, MN, 1993.

(23) Knözinger, H.; Ratnasamy, P. *Catal. Rev. Sci. Eng*. **1978**, *17*, 31.

(24) 1 cal = 4.184 J.

(25) (a) Holm, V. C. F.; Blue, R. W. *Ind. Eng. Chem*. **1951**, *43*, 501. (b) Carleton, F. B.; Gilmore, T. A.; Laverty, T. D.; Rooney, J. J. *J. Chem. Soc. Chem. Commun*. **1977**, 896. (c) Narbershuber, T. F.; Vinnek, H.; Lercher, J. A. *J. Catal*. **1995**, *157*, 388. (d) Narbershuber, T. F.; Brait, T.; Seshan, K.; Lercher, J. A. *J. Catal*. **1997**, *172*, 127.

(26) Frash, M. V.; van Santen, R. A. *J. Phys. Chem. A* **2000**, *104*, 2468.

(27) Narbershuber, T. F.; Stockenhuber, M.; Brait, T.; Seshan, K.; Lercher, J. A. *J. Catal*. **1996**, *160*, 183.

(28) Kazansky, V. B.; Borovkov, V. Yu.; Zaitsev, A. V. *Proc. 9th Intl. Congr. Catal., Calgary* **1988**, *3*, 1426.

(29) Long, M. A.; Garnett, J. L.; Williams, P. G. *Aust. J. Chem*. **1982**, *35*, 1057.

(30) (a) Schoofs, B.; Schuermans, J.; Schoonheydt, R. A. *Micropor. Mesopor. Mater*. **2000**, *35*−*36*, 99. (b) Paravano, C.; Hammel, E. F.; Taylor, H. S. *J. Am. Chem. Soc*. **1948**, *70*, 2269. (c) Hansford, R. C.; Waldo, P. G.; Drake, I. C.; Honig, R. E. *Ind. Eng. Chem*. **1952**, *44*, 1108. (d) Hindin, S. G.; Mills, G. A.; Oblad, A. G. *J. Am. Chem. Soc*. **1955**, *77*, 538. (e) Burwell, R. L., Jr.; Porte, H. A.; Hamilton, W. H. *J. Am. Chem. Soc*. **1959**, *81*, 828. (f) Lapszewicz; J. A.; Jiang, X.-Z. *Catal. Lett*. **1992**, *13*, 103. (g) Iglesia, E.; Baumgartner, J. E. *Catal. Lett*. **1993**, *21*, 545. (h) Sommer, J.; Hachoumy, M.; Garin, F.; Barthomeuf, D. *J. Am. Chem. Soc*. **1994**, *116*, 5491.

(31) (a) Bloch, H. S.; Pines, H.; Schmerling, L. *J. Am. Chem. Soc*. **1946**, *68*, 153. (b) Nenitzescu, C. D.; Avram, M.; Sliam, E. *Bull. Soc. Chem. France* **1955**, 1266. (c) See also: Nenitzescu, C. D.; Cantuniari, I. P. *Ber. Dtsch. Chem. Ges.* **1933**, *66*, 1097.

(32) (a) J. M.Oelderik cited in: Brouwer, D. M.; Mackor, E. L. *Proc. Chem. Soc*. **1964**, 147. (b) Oelderik, J. M.; Mackor, E. L.; Platteeuw, J. C.; van der Wie, A. British Patent 981,311 (appl. 1962), equivalent to U.S. Patent 3,201,494, 1965. (c) Brouwer, D. M.; Hogeveen, H. *Prog. Phys. Org. Chem*. **1972**, *9*, 179.

(33) Fărcaşiu, D.; Siskin, M.; Rhodes, R. P. *J. Am. Chem. Soc*. **1979**, *101*, 7671.

(34) (a) Jacobs, P. A. *Carboniogenic Activity of Zeolites*; Elsevier: Amsterdam, 1977. (b) Mirodatos, C.; Barthomeuf, D. *J. Chem. Soc. Chem. Commun*. **1981**, 39. (c) Jacobs, P. A. *Catal. Rev.-Sci. Eng*. **1982**, *24*, 415. (d) Mihindou-Koumba, P. C.; Lemberton, J. L.; Perot, G.; Guisnet, M. *Nouv. J. Chim*. **1984**, *8*, 31. (e) Patrilyak, K. I.; Bortyshevskii, V. A.; Tsuprik, I. N.; Gutyrya, V. S.; Baiburskii, V. L. *Doklady Akademii Nauk S. S. S. R.* **1985**, *283*, 384. (f) Martens, J. A.; Jacobs, P. A. In ref 2, p 52.

(35) Treatments of alkene hydrogenation/alkane dehydrogenation: (a) Senger, S.; Radom., L. *J. Am. Chem. Soc*. **2000**, *122*, 2613. (b) Kazansky, V. B.; Frash, M. V.; van Santen, R. A. *Catal. Lett*. **1994**, *28*, 211.

(36) (a) Fărcaşiu, D.; Marino, G. M.; Kastrup, R. V.; Rose, K. D. presented at the 185th American Chemical Society National Meeting, Seattle, WA, March 1983, Abstract ORGN 160. (b) Fărcaşiu, D.; Ghenciu, A.; Marino, G.; Rose, K. D. *J. Am. Chem. Soc.* **1997**, *119*, 11826.

(37) (a) Fărcaşiu, D. *J. Chem. Soc. Chem. Commun*. **1994**, 1801. (b) Xu, T.; Munson, E. J.; Haw, J. F. *J. Am. Chem. Soc.* **1994**, *116*, 1962.

(38) (a) Fărcaşiu, D. Lukinskas, P. *J. Chem. Soc., Perkin Trans. 2* **1999**, 1609. (b) Fărcaşiu, D. Lukinskas, P. *J. Chem. Soc., Perkin Trans. 2* **1999**, 2715. (c) Fărcaşiu, D. Lukinskas, P. *J. Chem. Soc., Perkin Trans. 2* **2000**, 2295.

(39) Olah, G. A.; Surya Prakash, G. K. S.; Sommer, J. *Superacids*; Wiley: New York, 1985; p 249.

(40) Sokolovskii, V. D.; Mamedov, E. A. *Catal. Today* **1992**, *14*, 331 (Part 4).

(41) Capitán, M. J.; Odriozola, J. A.; Márquez, A.; Sanz, J. F. *J. Catal*. **1995**, *156*, 273.

(42) (a) Stamires, D. N.; Turkevich, J. *J. Am. Chem. Soc*. **1964**, *86*, 749. (b) Shih, S. *J. Catal*. **1983**, *79*, 390. (c) McVicker, G. B.; Kramer, G. M.; Ziemiak, J. J. *J. Catal*. **1983**, *83*, 286. (d) Fărcaşiu, D.; Ghenciu, A. *Prepr. Div. Pet. Chem., Am. Chem. Soc.* **1994**, *39*, 479. (e) Fărcaşiu, D.; Ghenciu, A.; Li, J. Q. *J. Catal*. **1996**, *158*, 116.

(43) Alvarez, L. J.; Blumenfeld, A. L.; Fripiat, J. J. *J. Chem. Phys*. **1998**, *108*, 1724.

(44) Fărcaşiu, D.; Lee, K.-H. *J. Mol. Catal., A* **2000**, *161*, 213.

(45) Fărcaşiu, D.; Lee, K.-H. *Catal. Commun.* **2001**, *2*, 5.

# Formation of Hydrocarbons from the Reduction of Aqueous $CO_2$ by Zero-Valent Iron

LESLIE I. HARDY† AND ROBERT W. GILLHAM*

*Waterloo Centre for Groundwater Research, University of Waterloo, Waterloo, Ontario, N2L 3G1 Canada*

The reduction of aqueous $CO_2$ by zero-valent iron was studied in batch and column experiments. Ten hydrocarbons up to C5 were identified as products of the reduction process and were shown to have Anderson–Schulz–Flory (ASF) product distributions. A direct consequence of the ASF product distribution is that a significant mass of hydrophobic hydrocarbons may remain sorbed to the iron surface. Based on a reaction mechanism proposed for the electroreduction of aqueous $CO_2$ with nickel electrodes, iron acts as both a reactant by corroding to supply electrons and as a catalyst by promoting the formation and growth of hydrocarbon chains. Water is also a reactant in the system. When iron is used to enhance the dechlorination of chlorinated organic compounds, the slow desorption of the hydrocarbon products may become the rate-limiting step in the reaction.

## Introduction

Chlorinated hydrocarbons, primarily used as industrial solvents and dry cleaning fluids, are widespread and persistent groundwater contaminants. The most common method used to treat this contamination involves pumping contaminated water to the surface for treatment; however, complete removal of the contaminants from the subsurface is rarely achieved, and the treatment usually only transfers the contamination to another medium (*1*). A possible alternative to pump and treat is the containment of the contamination with *in situ* barriers using reactive media to degrade the contaminants present in the groundwater (*2*).

Zero-valent iron has recently been shown to rapidly dechlorinate a wide range of chlorinated hydrocarbons in laboratory batch and column experiments (*3–6*) and has been successfully used to dechlorinate trichloroethylene and perchloroethylene in a field demonstration of a reactive barrier system (*7, 8*). Zero-valent iron is a very promising reactive medium due to its effectiveness, low cost, and ability to degrade contaminants over wide concentration ranges; however, the reaction mechanism remains elusive. Studies to date have confirmed that the reaction is reductive, abiotic, and heterogeneous. While it has been proposed that the reduction proceeds by direct electron transfer from the iron surface to the chlorinated organic, the possibility that adsorbed hydrogen from the reduction of water is involved in a catalytic reaction on the iron surface has not been eliminated (*6*).

Abiotic dechlorination of chlorinated hydrocarbons in aqueous solution has received relatively little attention compared to biological systems. Abiotic studies include homogeneous reactions with water (*9–11*) or reactions mediated by transition metal complexes such as porphyrins (*12–15*). Heterogeneous dechlorination reactions in aqueous solution have been studied for mineral–water systems (*16–19*), as has electrolysis with platinum electrodes (*20*). Hydrodechlorination using a proprietary palladium catalyst and hydrogen gas has also been reported (*21*). While some of these reactions are relatively rapid, notably those with the palladium catalyst, abiotic dechlorination generally proceeds too slowly to be a useful remediation technology. Iron-enhanced dechlorination proceeds at rates comparable to those reported for the palladium catalyst, and it has the very significant advantage that an engineered system is not required to supply another reactant.

This study is based on the results of preliminary design studies for a large-scale field installation of an *in situ* reactive barrier. In those tests, it was found that dissolved C1–C5 hydrocarbons were present in a control column containing iron and water. Because no organic constituents were present in the influent solution, the source of the hydrocarbons was unknown. This result is similar to observations reported by Senzaki and Kumagi (*22*), who attributed the presence of the hydrocarbons to the transformation of unidentified organics in the source water.

The purpose of this study was to identify reaction products and the reaction pathway of iron and aqueous solution systems. It is shown that C1–C5 hydrocarbons are formed by the reduction of aqueous $CO_2$ by zero-valent iron and that the products have an Anderson–Schulz–Flory (ASF) distribution. ASF product distributions are well known in Fischer–Tropsch synthesis where long-chain hydrocarbons are produced by contacting CO and $H_2$ gases with a heterogeneous catalyst such as iron or nickel (*23*). A conceptual model is presented which postulates that alkenes and alkanes are formed on the iron surface and that alkenes can be re-incorporated into longer hydrocarbon chains. This conceptual model is used to show that a deviation from an ideal ASF distribution is expected for long-chain hydrocarbons and that significant carbon mass may remain sorbed to the iron surface. Based on a reaction mechanism proposed for the electroreduction of aqueous $CO_2$, iron in this system acts as both a reactant, by corroding to supply electrons, and as a catalyst, by promoting the formation of hydrocarbons. Water is also a reactant in this system.

## Experimental Section

Tests were conducted with various iron and aqueous solution combinations to evaluate the effects of different materials on the hydrocarbons detected in solution. Selected batches of iron were pretreated with $H_2$ to increase the concentration of hydrogen in the iron. This pretreatment was undertaken to determine if adsorbed hydrogen

* Corresponding author.

† Present address: Morrow Environmental Consultants, 8658 Commerce Court, Burnaby, BC, V5A 4N6 Canada.

0013-936X/96/0930-0057$12.00/0 

**TABLE 1**
**Simulated Groundwater Inorganic Analysis**

| parameter | measured concn (mg/L) | measured concn (mequiv/L) |
|---|---|---|
| $Fe^{2+}$ | <0.05 | <0.002 |
| $Na^{+}$ | 8.59 | 0.374 |
| $Mg^{2+}$ | 1.09 | 0.090 |
| $Ca^{2+}$ | 2.47 | 0.123 |
| $Cl^{-}$ | 14.8 | 0.417 |
| $SO_4^{2-}$ | 4.42 | 0.092 |
| $HCO_3^{-}$ | 12.3 | 0.201 |

affected the concentration of hydrocarbons detected in solution. A total of 14 batch experiments and three column experiments were completed. All experiments were conducted at room temperature, between 20 and 25 °C.

**Materials.** Most experiments were conducted with the iron proposed for use in large-scale field applications. This material is relatively inexpensive, commercially available (Master Builders, Cleveland, OH) metal cuttings. Analyses indicate that this material is approximately 90% iron, with small amounts of other metals (<5% Mn, <3% Cu, and <2% Cr; Canviro Analytical Labs, Ltd.) and 2.4% C. The material has a BET surface area of 1.1 $m^2/g$ and a grain size between 0.6 and 2.0 mm. Selected batches of the commercial iron were pretreated with $H_2$ gas by filling a stainless steel cell with iron and applying the hydrogen pressure (5 or 10 atm) for several weeks. No attempt was made to remove ambient air from the pressure cell prior to the application of the gas pressure. The hydrogen was analytical grade and was used without purification. Additional experiments were conducted using electrolytic iron (Fisher Scientific, 100 mesh, >99% iron) to validate data interpretations. Except for the hydrogen gas pretreatment, both sources of iron were used as received.

Various waters were used over the course of the study, though most tests were conducted using a simulated groundwater prepared by adding reagent-grade salts ($MgSO_4$, $CaCl_2$, NaCl, and $NaHCO_3$) to distilled water and then acidifying with HCl to a pH of 6.0. A chemical analysis of this water is given in Table 1. Selected experiments were conducted using organic-free water (distilled, carbon filtered, and UV oxidized) with no added salts, and with water containing 40 mg/L $CaCO_3$. No attempt was made to deoxygenate or decarbonate the waters prior to use.

The waters used for the column experiments with electrolytic iron were prepared from 18 MΩ·cm Nanopure water that was deoxygenated and decarbonated by bubbling with $N_2$ gas for 5 h. $CaCO_3$ (120 mg/L) was added to one water, and KBr (40 mg/L) was added to the other. These waters were stored in glass carboys under an $N_2$ atmosphere to prevent contamination from atmospheric $O_2$ and $CO_2$.

**Analyses.** Samples for hydrocarbon analyses were collected in 2-mL vials with 0.5 mL of headspace and immediately sealed with a Teflon-faced silicone septa. Samples were shaken for 15 min on a rotary shaker for equilibration with the headspace. Headspace samples of 50 μL were collected and manually injected into the gas chromatographs using a gas-tight syringe.

Samples were analyzed for hydrocarbons using gas chromatographs with a flame ionization detector or a photoionization detector. The FID was a Hewlett-Packard Model 5790 GC with a GS-Q column (J&W Scientific, 30 m × 0.545 mm). The oven temperature program was 60 °C for 3 min and 25 °C/min to 90 °C. The injection port and detector temperatures were 120 and 180 °C, respectively. The carrier gas was nitrogen, with a flow rate of 9 mL/min, and the split ratio was 5:1. Alkenes were also analyzed on a Photovac 10S50 GC with a photoionization detector and an isothermal oven at 30 °C. The ionization potential of the PID bulb was 10.6 eV, and the carrier gas was zero air at a flow rate of 10 mL/min. The PID was fitted with a TFE-packed column with 5% SE-30 on Chromosorb G, AW-DMCS (100–120 mesh).

Hydrocarbons in the samples were identified by comparing retention times with hydrocarbon standards. The gas chromatographs were calibrated with a commercially prepared gas standard containing methane, ethene, ethane, propene, propane, 1-butene, *n*-butane, and isobutane. Ambient methane concentrations for the particular day, which ranged from 2 to 5 μg/L in the gas phase, were subtracted from the sample concentrations. The PID was calibrated for *cis*- and *trans*-2-butene with individual gas standards; butene data are presented as total butenes. Water concentrations were calculated using Henry's law constants from MacKay and Shiu (*24*). Methanol-based standards were prepared for the three individual pentene isomers. Gas standards were purchased from Linde, and the pentene isomers were purchased from Aldrich. The detection limits for these compounds, as presented in Tables 2 and 3, were determined using the EPA procedure for method detection limit (MDL). The PID had a lower detection limit for alkenes than the FID, and consequently, the PID data are presented here. Samples were not analyzed for alcohols, hydrogen gas, or formate.

**Batch Experiments.** In these tests, 10.0 g of iron was added to 40-mL glass vials. The vials were then filled with aqueous solution, leaving no headspace, and were immediately sealed with aluminium crimp caps and Teflon-faced silicone septa. The filled vials were weighed and then placed on a rotating disk (two revolutions per minute, axis horizontal), which allowed complete mixing without excessive agitation. The rotating disk was kept in the dark to avoid photocatalytic reactions. As required, vials were removed from the rotating disk and centrifuged for 2 min at 380*g* to remove suspended iron. Samples for hydrocarbon analysis were collected through the septa with a 2.0-mL syringe.

**Column Experiments.** The column procedure was similar to that described in Gillham and O'Hannesin (*5*). A 1 m long acrylic column (3 cm i.d.) was packed with the commercial iron in 2-cm increments. Seven sampling ports were located along the column at distances at 5, 10, 20, 30, 40, 60, and 80 cm from the influent end. Each sampling port consisted of a nylon Swagelok fitting (0.16 cm o.d.) with a permanently mounted 3.8 cm long 16 gauge luer lock syringe needle. The syringe needle was packed with glass wool and capped with a plastic syringe tip filled with silicone. Simulated groundwater was drawn from a plastic container at 0.5 mL/min by a peristaltic pump. With an average water-filled porosity of 0.40, the water had a residence time in the column of 14 h. All tubing was Teflon, with the exception of a short length of Viton tubing that passed through the pump. A stainless steel 'T' on the delivery line allowed sampling of the influent water. The column was sampled by clamping the effluent line and allowing water to flow from a sampling port directly into

**TABLE 2**

## Hydrocarbons Detected in Batch Experiments[a]

| $H_2$ pretreatment (atm) | water type | time (h) | methane | ethene | ethane | propene | propane | butenes | total HC | ASF distribution parameters: slope α | intercept α | $R^2$ |
|---|---|---|---|---|---|---|---|---|---|---|---|---|
| **Commercial Iron** | | | | | | | | | | | | |
| 0 | sim GW | 144 | 2.7 | 0.45 | 0.8 | 0.14 | < | < | 4.1 | 0.14 | 0.09 | 0.98 |
| 0 | sim GW | 144 | 2.7 | 1.63 | 1.1 | 0.38 | < | < | 5.8 | 0.22 | 0.19 | 0.91 |
| 0 | sim GW | 144 | 3.2 | 0.91 | 0.8 | 0.18 | < | < | 5.1 | 0.14 | 0.10 | 0.96 |
| 0 | sim GW | 144 | 2.6 | 1.17 | 0.8 | 0.30 | < | < | 4.9 | 0.20 | 0.17 | 0.95 |
| 0 | sim GW | 144 | 1.5 | 0.33 | 0.4 | 0.09 | < | 0.3 | 2.6 | 0.15 | 0.12 | 0.96 |
| 0 | sim GW | 144 | 1.7 | 0.91 | 0.8 | 0.16 | < | 0.2 | 3.8 | 0.18 | 0.16 | 0.89 |
| 0 | sim GW | 123 | 1.2 | 0.60 | 0.3 | 0.23 | < | < | 2.3 | 0.26 | 0.23 | 0.96 |
| 5 | sim GW | 144 | 3.0 | 3.58 | 1.9 | 0.99 | < | 0.9 | 10.4 | 0.37 | 0.37 | 0.87 |
| 5 | sim GW | 123 | 2.1 | 0.37 | 1.0 | 0.34 | < | < | 3.8 | 0.17 | 0.12 | 0.97 |
| 10 | sim GW | 142 | 4.5 | 2.05 | 2.1 | 0.67 | < | 0.4 | 9.7 | 0.25 | 0.23 | 0.96 |
| 5 | organic free | 144 | 3.4 | 2.72 | 2.2 | 0.75 | < | 0.4 | 9.4 | 0.27 | 0.25 | 0.93 |
| 10 | 40 mg/L $CaCO_3$ | 142 | 4.6 | 2.49 | 1.8 | 0.57 | < | 0.3 | 9.8 | 0.24 | 0.21 | 0.95 |
| **Electrolytic Iron** | | | | | | | | | | | | |
| 0 | organic free | 141 | 1.0 | 0.14 | 0.3 | < | < | 0.1 | 1.5 | | | |
| 0 | sim GW | 141 | tr | 0.17 | tr | 0.05 | < | 0.1 | 0.3 | | | |
| method detection limit | | | 0.9 | 0.03 | 0.3 | 0.03 | 0.4 | 0.1 | | | | |

[a] Note: these samples were not analyzed for pentenes. All concentrations are expressed as μg/L; sim GW = simulated groundwater; < = not detected; tr = trace.

**TABLE 3**

## Hydrocarbons Detected in Column Experiments[a]

| distance (cm) | methane | ethene | ethane | propene | propane | butenes | 1-pentene | *cis*-2-pentene | *trans*-2-pentene | total HC |
|---|---|---|---|---|---|---|---|---|---|---|
| **Commercial Iron, Simulated Groundwater, Time = 138 days** | | | | | | | | | | |
| 0 | < | < | < | < | < | < | NA | NA | NA | < |
| 5 | 4.6 | 0.33 | 1.8 | 1.73 | < | 1.1 | NA | NA | NA | 9.6 |
| 10 | 8.4 | 0.26 | 1.7 | 1.38 | < | 0.7 | NA | NA | NA | 12.4 |
| 20 | 7.8 | 0.24 | 1.5 | 1.27 | < | 0.6 | NA | NA | NA | 11.4 |
| 30 | 6.5 | 0.26 | 1.4 | 1.13 | < | 0.4 | NA | NA | NA | 9.7 |
| 40 | 6.0 | 0.31 | 1.5 | 1.27 | < | 0.7 | NA | NA | NA | 9.8 |
| 60 | 4.4 | 0.28 | 1.4 | 1.15 | < | 0.5 | NA | NA | NA | 7.7 |
| 80 | 3.7 | 0.26 | 1.2 | 1.10 | < | 0.4 | NA | NA | NA | 6.7 |
| 100 | 2.9 | 0.24 | 1.2 | 0.98 | < | 0.2 | NA | NA | NA | 5.5 |
| **Commercial Iron, Simulated Groundwater, Time = 351 days** | | | | | | | | | | |
| 0 | < | < | < | < | < | < | < | < | < | < |
| 5 | 6.3 | 0.33 | 2.7 | 1.29 | 1.6 | 1.5 | < | 0.4 | < | 14.1 |
| 10 | 71.0 | 0.63 | 2.3 | 1.34 | 2.0 | 1.9 | 0.2 | 0.2 | 1.2 | 80.8 |
| 20 | 118.9 | 0.68 | 2.2 | 1.35 | 1.6 | 1.8 | 0.1 | 1.5 | 0.8 | 128.9 |
| 30 | 125.3 | 0.73 | 2.3 | 1.35 | 1.9 | 1.9 | 0.1 | 1.4 | 0.8 | 135.8 |
| 40 | 111.9 | 0.59 | 2.2 | 1.35 | < | 1.7 | < | 0.8 | 0.2 | 118.7 |
| 60 | 92.5 | 0.63 | 1.7 | 1.15 | < | 1.5 | < | 0.3 | < | 97.8 |
| 80 | 98.4 | 0.68 | 1.9 | 1.20 | < | 1.5 | < | < | < | 103.7 |
| 100 | 115.9 | 0.59 | 1.6 | 1.13 | < | 1.5 | < | < | < | 120.7 |
| **Electrolytic Iron, 120 mg/L $CaCO_3$ Water, Time = 25 days** | | | | | | | | | | |
| 4 | tr | 0.05 | 0.5 | 0.03 | < | < | < | < | < | 0.6 |
| 8 | 0.9 | 0.06 | 1.5 | 0.07 | < | 0.2 | < | < | < | 2.7 |
| 12 | Tr | 0.04 | 0.4 | 0.03 | < | 0.1 | < | < | < | 0.6 |
| **Electrolytic Iron, 40 mg/L KBr Water, Time = 25 days** | | | | | | | | | | |
| 4 | tr | < | 0.8 | 0.05 | < | < | < | < | < | 0.9 |
| 8 | 1.2 | 0.05 | 1.0 | 0.07 | < | 0.2 | < | < | < | 2.5 |
| 12 | < | 0.04 | 0.3 | 0.03 | < | < | < | < | < | 0.4 |
| MDL | 0.9 | 0.03 | 0.3 | 0.03 | 0.4 | 0.1 | 0.6 | 5.5 | 5.5 | |

[a] All concentrations are expressed as μg/L. MDL = method detection limit; < = not detected; NA = not analyzed; tr = trace.

a 2.0-mL syringe. Two 16 cm long columns containing electrolytic iron were prepared in a similar manner.

## Results and Discussion

**Hydrocarbons Detected.** Hydrocarbons, including methane, ethene, ethane, propene, propane, 1-butene, and *cis*-2-butene were detected in all experiments. Trace concentrations of the three pentene isomers were detected in the commercial iron column when these compounds were first tested for after 1 year of continuous operation. Samples from the batch experiments were not analyzed for pentenes. Pentene concentrations are reported in Table 3, even though they fall below the 99% confidence interval of the method detection limit. The concentrations of the various hydrocarbons in one of the batch experiments and in the commercial iron column are presented in Figures 1 and 2, respectively. Batch experiment data at approximately 140 h for the various iron and water combinations are presented

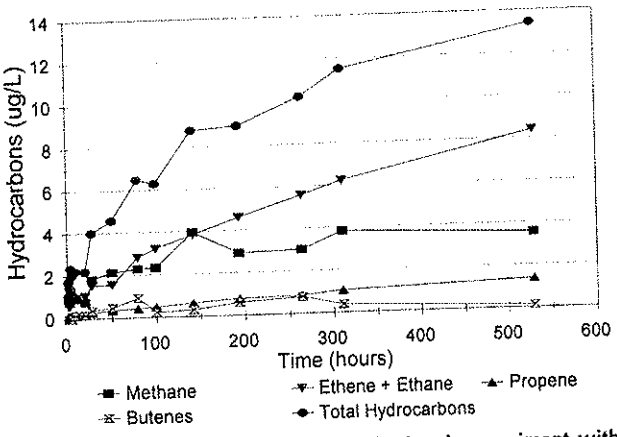


**FIGURE 1. Hydrocarbons detected in the batch experiment with simulated groundwater and commercial iron that had been pretreated with 10 atm $H_2$.**

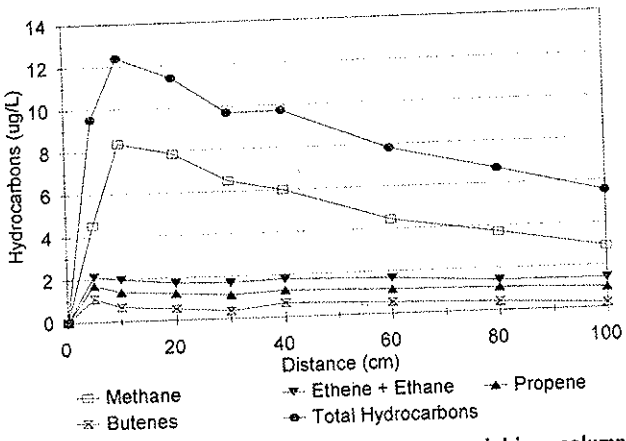


**FIGURE 2. Hydrocarbons detected in the commercial iron column at 138 days.**

in Table 2. Complete data sets for the column experiments are presented in Table 3. All concentration data are presented on a weight per volume basis for evaluation of the product distributions.

Three possible explanations for the generation of detectable hydrocarbons are proposed: (1) release by corrosion of the commercial iron; (2) transformation products of unidentified organics in the source water; and (3) synthesis from the reduction of aqueous $CO_2$. The commercial iron has a poorly characterized carbon component (2.4% by weight), which appears to be partially derived from the industrial process by which the metal fragments and cutting oil are heated in a rotary kiln. While exact details of the process are proprietary, based on temperatures typically used to anneal iron, the process undoubtedly heats the iron to between 700 and 1100 °C. Under these conditions, any hydrocarbons present on the iron would likely be transformed to graphitic carbon (*25*).

Though the carbon associated with the commercial iron was believed to be nonreactive, tests were conducted to compare hydrocarbon production between the commercial and electrolytic iron. As shown in Tables 2 and 3, hydrocarbons were also detectable with electrolytic iron, though at lower concentrations than with the commercial iron. The data for the electrolytic iron presented in Table 2 are quantitatively uncertain due to apparent leakage from the reactive vials; however, the evidence strongly suggests that the observed hydrocarbons are not being released from the commercial iron.

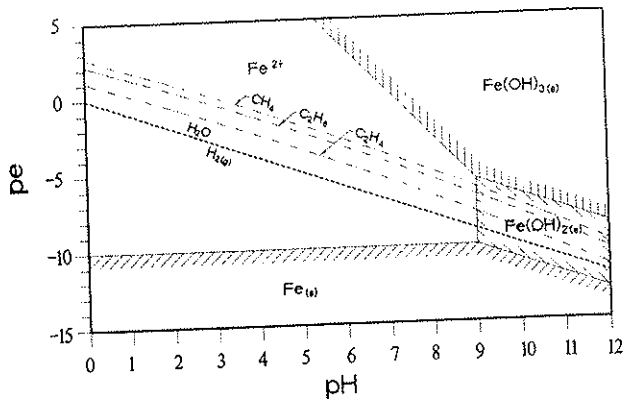


**FIGURE 3. pe–pH diagram for the Fe-$H_2O$-$CO_2$ system, assuming $10^{-5}$ M Fe in solution. The reduction potentials for the $CO_2$/hydrocarbon couples were calculated according to the method presented in ref 26.**

A second potential source of the observed hydrocarbons, as suggested by Senzaki and Kumagi (*22*), is the transformation of unidentified organics in the source water. While no hydrocarbons or unidentified peaks were observed in the source waters, batch experiments were conducted with specially prepared organic-free water to test this hypothesis. The organic-free water was prepared from distilled water that was passed through an activated carbon filter and then exposed to UV light. As shown in Table 2, the use of organic-free water had no affect on the amount of detectable hydrocarbons.

Having largely discounted the possibilities that the hydrocarbons are being released from the commercial iron or are transformation products of unidentified hydrocarbons in the source water, the remaining possibility is that the hydrocarbons are formed by the reduction of aqueous $CO_2$. Standard reduction potentials for the various $CO_2$/hydrocarbon couples were calculated according to the method presented by Pankow (*26*), and the results for methane, ethene, and ethane are presented in Figure 3. The formation of hydrocarbons from the reduction of aqueous $CO_2$ is thermodynamically possible, but the reactions are extremely slow without a suitable biotic or abiotic catalyst due to the requirement of multiple electron transfer. Methane will be the dominant species at strongly reducing conditions; however, it should be noted that the other hydrocarbons have standard reduction potentials near that of methane, and they may also be present in aqueous solution at equilibrium.

In all experiments, it appears that there were much larger concentrations of aqueous $CO_2$ than hydrocarbons detected, which may indicate that $CO_2$ is present in excess and is not limiting the reaction rate. This could explain why varying the alkalinity of the aqueous solution did not noticeably affect the hydrocarbon concentrations (Tables 2 and 3). The detection limits for the hydrocarbons are approximately 2 orders of magnitude lower than the detection limit for $HCO_3^-$. Therefore, even if aqueous $CO_2$ was nondetectable, there could still be enough carbon present to account for the observed hydrocarbons. For example, in the electrolytic iron column experiment using KBr water, the total mass of carbon detected at the 8-cm sampling port was $10^{-6.8}$ mol/L. Therefore, only 0.01 mg/L of $HCO_3^-$ ($10^{-6.8}$ mol/L) would be required to synthesize the hydrocarbons detected in the column. This would explain why attempting to decarbonate the KBr water by

purging with $N_2$ did not significantly affect the concentration of hydrocarbons detected in the electrolytic iron column. While it has not been proven that the hydrocarbons detected in these experiments were formed by the reduction of aqueous $CO_2$, it is a reasonable hypothesis based on the data and relevant electrochemical literature as included in the following discussion.

**Reduction of Aqueous $CO_2$ and Fischer–Tropsch Synthesis.** The formation of long-chain hydrocarbons from the reduction of aqueous $CO_2$ was first reported by Japanese electrochemists in the mid-1980s (*27*). When copper electrodes were used in an electrolysis cell containing water and $CO_2$, significant amounts of $H_2$, alkenes, alkanes, and alcohols were formed. Prior to this time, researchers had investigated the formation of formate, HCOOH, from aqueous $CO_2$ (*28*), but they did not analyze for gaseous products such as $CH_4$, $C_2H_4$, or $C_2H_6$. It was later found that most pure metal electrodes produced hydrocarbons (*29–32*) but that copper was by far the most efficient. The reaction products from electrolysis were found to vary with the potential applied (*29–36*), the pressure of $CO_2$ applied (*31, 32*), the electrode surface texture (*33*), the type and concentration of electrolytes in solution (*34, 35*), and the temperature (*31, 32, 36*).

The potentials typically applied during electroreduction studies are more reducing than the potential provided by the anaerobic corrosion of $Fe_{(s)}$, but the difference is relatively small. As shown in Figure 3, the overpotential at near-neutral pH for the $CO_2$/hydrocarbon couples versus the $Fe_{(s)}/Fe^{2+}$ couple is about −0.3 V, assuming $10^{-5}$ M iron in solution. It is known that the highest Faradic efficiency for hydrocarbon formation is achieved at an applied potential of approximately −1.4 V versus the standard hydrogen electrode (SHE) (*27, 29–37*). However, Kudo et al. (*32*) found that hydrocarbons were detectable in a nickel electrode system at approximately 10% of the peak Faradic efficiency at an applied potential of −0.78 V SHE (pe = −13.2). An applied potential of −0.78 V provides an overpotential to the $CO_2$/hydrocarbon couples of about −0.5 V at near-neutral pH. Therefore, the relatively small overpotential provided by the anaerobic corrosion of the iron is comparable to that quoted in the electrochemical literature.

Fischer–Tropsch synthesis is the process by which CO and $H_2$ gases are passed over a heterogeneous catalyst, such as iron or nickel, to form long-chain hydrocarbons. It is noted that the first Fischer–Tropsch catalysts were alkali-treated metal shavings (*23*) and thus were similar to the commercial iron used in this study. The analogy between the electrochemical reduction of aqueous $CO_2$ and Fischer–Tropsch synthesis was first suggested by Hori et al. (*37*) in 1989. Using data from a palladium electrode study in which up to C6 hydrocarbons formed (*36*), Cook et al. (*38*), as cited in Kudo et al. (*32*), showed that the hydrocarbon products had an Anderson–Schulz–Flory (ASF) distribution, which is well known from Fischer–Tropsch synthesis. In 1993, Kudo et al. (*32*) showed that the hydrocarbons formed from the electroreduction of aqueous $CO_2$ by iron, nickel, or cobalt electrodes also have ASF distributions.

Knowledge of Fischer–Tropsch synthesis can be used to provide insight into the mechanisms of aqueous $CO_2$ reduction. Desorption of a growing carbon chain from the iron surface determines whether the chain will be a hydrocarbon or an alcohol. Alkenes form by $\beta$-hydrogen abstraction from the growing carbon chain, whereas alkanes or alcohols form by adding either an H or a OH to the $\alpha$-hydrogen of the carbon chain. Alkanes can also form as a secondary product by re-adsorption of an alkene onto the iron surface, followed by hydrogenation by adsorbed hydrogen. The catalytic hydrogenation of gas phase ethene to ethane by hydrogen adsorbed to transition metals is well known (*39*); however, recent work suggests that the presence of water inhibits this secondary hydrogenation reaction and that alkanes are mainly formed as a primary product (*40, 41*).

**Molecular Weight Distribution.** The products of Fischer–Tropsch synthesis, hydrocarbons and alcohols, have an Anderson–Schultz–Flory product distribution, which could also be described as a "most-probable" or "normal" distribution. The following development will be restricted to hydrocarbons, but the same principles could be applied to the formation of alcohols. The Anderson–Schulz–Flory distribution of molecular weights can be expressed in two ways (23): eq 1 is that given by Schulz, and eq 2 is that given by Flory

$$M_n = (\ln^2 \alpha) n \alpha^n \tag{1}$$

$$M_n = (1 - \alpha)^2 n \alpha^{(n-1)} \tag{2}$$

where $n$ is the number of carbons in the chain, and $M_n$ is the *weight* fraction (not mole fraction) of hydrocarbons with carbon number $n$. The primary hydrocarbons can be partially transformed into various isomers; therefore, the weight fraction $M_n$ is the sum of all hydrocarbon isomers for a given carbon number $n$. $\alpha$ is the probability of chain growth and is defined as

$$\alpha_n = \frac{R_{p,n}}{R_{p,n} + R_{t,n}} \tag{3}$$

where $R_{p,n}$ is the rate of chain propogation, and $R_{t,n}$ is the rate of chain termination, i.e. the rate at which it desorbs from the catalyst surface. In an ideal ASF distribution, the probability of chain growth is independent of n, and a plot of log $(M_n/n)$ versus $n$ is linear. Equation 1 does not adequately describe the product distribution when $\alpha < 0.5$; however, the two equations are equivalent when $\alpha > 0.5$. The equations give identical results when determining $\alpha$ from a graphical representation of the molecular weight distribution of the reaction products. Equation 1 can be expressed in logarithmic form as

$$\log\left(\frac{M_n}{n}\right) = \log(\ln^2 \alpha) + n \log \alpha \tag{4}$$

The products of a reaction have an ASF distribution if the plot of log $(M_n/n)$ versus $n$ is linear and if the value of $\alpha$ as determined from the slope (log $\alpha$) and the intercept with the $y$-axis [log $(\ln^2 \alpha)$] are approximately equal (*23*). All values for the slope and intercept of the ASF plots presented here were calculated by linear regression.

It has been shown that the hydrocarbons formed by the electroreduction of aqueous $CO_2$ by iron, nickel, and cobalt electrodes have ASF distributions. Iron had the highest probability of chain growth of these three metals, which is consistent with the fact that iron is one of the most active Fischer–Tropsch catalysts. However, as shown in Table 4, it appears that Kudo et al. (32) miscalculated the value of $\alpha$ for the iron electrode. The values of $\alpha$ calculated here

**TABLE 4**

**ASF Distribution Parameters for the Electroreduction of Aqueous $CO_2$ [a]**

| | iron | nickel | cobalt |
|---|---|---|---|
| slope α | 0.59 | 0.33 | 0.46 |
| intercept α | 0.52 | 0.31 | 0.42 |
| $R^2$ | 0.97 | 0.98 | 0.98 |
| calculated α | 0.56 | 0.32 | 0.44 |
| reported α | 0.7 | 0.36 | 0.42 |

[a] Values for α were reported by Kudo et al. (*32*). Data for the iron and cobalt electrodes are from Nakagawa et al. (*31*).

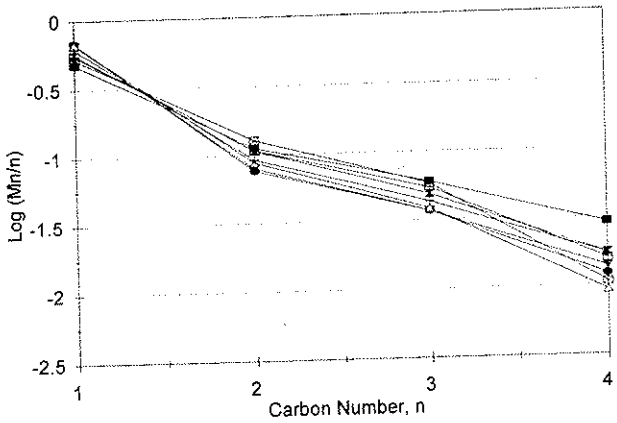


**FIGURE 4. Anderson–Schulz–Flory plot for the commercial iron column at 138 days. Each line represents one sample.**

for nickel and cobalt appear to be in agreement with the values reported in ref 32; however, the calculated value for iron (α = 0.56) is substantially lower than the value reported (α = 0.7).

Early time (138 days) data from the commercial iron column (Table 3) has an average probability of chain growth of 0.30. As shown in Figure 4, ASF plots for the data are reasonably linear, and the values for α determined from the slope and intercept are very similar; therefore, the hydrocarbons appear to have an ASF distribution.

Methane is expected to be the dominant aqueous carbon species at strongly reducing conditions (*26*). Though the large increase in methane between day 138 and day 351 data for the commercial iron column is difficult to explain, it is not entirely inconsistent with the literature. In Fischer–Tropsch synthesis, the weight fraction of methane is always higher than predicted by an ideal ASF distribution, and there is no apparent consensus in the literature to explain this phenomenon (*42*). The high methane concentrations in the commercial iron column at late time (351 days) change the interpretation of the ASF plots slightly. As shown in Figure 5, the hydrocarbons from C2 to C5 plot as a straight line, but the measured methane concentrations are too high relative to the other hydrocarbons. Normalizing the hydrocarbons without methane changes the value of α determined from the intercept without changing the slope of the linear segment of the line. From the slope of the linear segment from C2 to C5 ($R^2$ = 0.96), the value for α = 0.58, and the value from the intercept is α = 0.50. Therefore, the data meet the requirements for an ASF distribution reasonably well, and the average value of α = 0.54 is comparable to the value (α = 0.56) calculated from Kudo's data. For the sake of clarity, only the data from the 10-cm sampling port are presented in Figure 4, but data

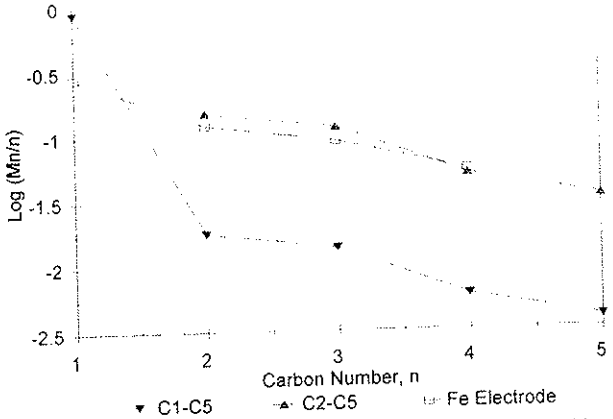


**FIGURE 5. ASF plot for 10-cm sampling port in the commercial iron column at 351 days. Iron electrode data is from ref 31.**

from the other sampling ports are similar. While the hydrocarbon concentrations observed in the commercial iron column changed with time, the fact that the late time probability of chain growth is comparable to published data indicates that the column may be approaching steady state.

The hydrocarbons detected in the batch experiments also appear to have an ASF product distribution, and pretreating the commercial iron used in the batch experiments with $H_2$ increased the measured hydrocarbon concentrations and the observed probability of chain growth. As shown in Table 2, after 140 h, the average and standard deviation of the total hydrocarbon concentrations in the seven tests using untreated iron is 4.1 ± 1.3 μg/L versus 8.6 ± 2.7 μg/L for the five tests using hydrogenated iron. The average probability of chain growth is α = 0.17 ± 0.05 for the untreated iron and α = 0.25 ± 0.08 for the hydrogenated iron. These results indicate that adsorbed hydrogen may be a reactant in the reduction of aqueous $CO_2$.

**Implications of the ASF Product Distribution.** The formation of long-chain hydrocarbons has implications for studies of iron-enhanced degradation of chlorinated organics, including effects on the carbon mass balance and the rate of the dechlorination reaction (*5*). According to eqs 1 and 2, as the value of α increases for an ideal ASF distribution, the weight percent of heavy hydrocarbons also increases. As shown in Figure 6, if the probability of chain growth is less than 0.3, virtually all of the hydrocarbon mass in the system will be in the form of C1–C4 hydrocarbons. However, it the steady state value of α is 0.54, then approximately 80% of the hydrocarbon mass will be present from C1 to C4, with the remainder in the form of heavier molecular weight hydrocarbons. Analyses are usually not conducted for the heavier hydrocarbons, and their increasing hydrophobicity makes it unlikely that they will be detectable in the water as they will tend to remain sorbed to the surface. In Fischer–Tropsch synthesis, the use of an ASF distribution to correct mass balance problems is recommended when heavy hydrocarbons remain on the catalyst, or where the analytical technique is incapable of heavy hydrocarbon analysis (*43*, *44*).

The data presented in Table 3 show that the probability of chain growth and the hydrocarbon concentrations both increase with time; therefore, it appears that these iron and water systems take a very long time to reach steady state. The re-incorporation of alkenes into longer hydrocarbons

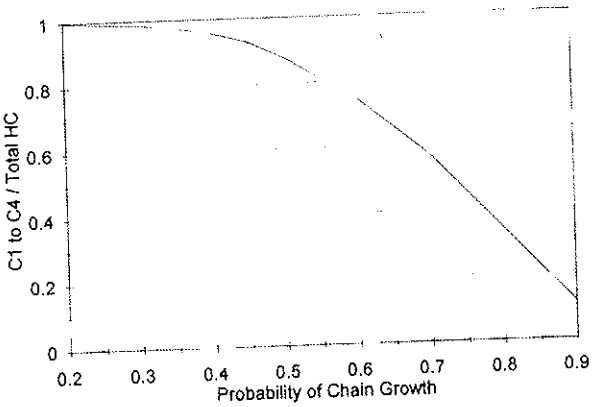


**FIGURE 6. C1–C4 hydrocarbons as a fraction of total hydrocarbons versus probability of chain growth. This figure is for an ideal ASF distribution.**

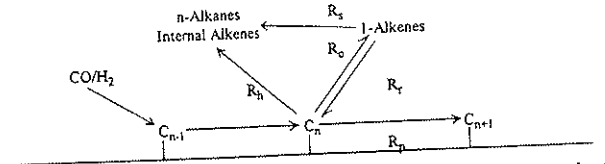


**FIGURE 7. Termination pathways for hydrocarbons formed on catalyst surface. In this reaction scheme, alkenes and alkanes can form as primary products, and alkanes and internal alkenes can also form by secondary reactions, after Iglesia et al. (41).**

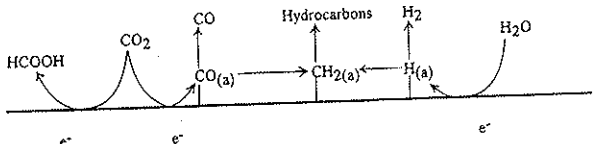


**FIGURE 8. Proposed reaction mechanism for the reduction of aqueous $CO_2$, after Kudo et al. (32). Termination pathways leading to the formation of hydrocarbons detectable in solution are presented in Figure 7.**

may explain these results. The re-incorporation of alkanes into growing hydrocarbon chains is not thermodynamically favored; however, alkenes readily re-incorporate (*40*, *41*). As the carbon chain length increases, the mobility of the compound decreases due in part to the increasing octanol–water partitioning coefficient, $K_{ow}$. As the carbon chain becomes less mobile, the probability of leaving the iron surface decreases, and the probability of chain growth increases. This concept of transport-enhanced alkene readsorption (*40*, *41*) was recently developed in Fischer–Tropsch synthesis to explain deviations from ASF distributions and the increasing alkane/alkene ratio at high carbon numbers. Using this conceptual model, it is hypothesized that the slow approach to steady state is related to competitive sorption and the increasing hydrophobicity of the hydrocarbons that are formed. As reactive sites on the iron surface become populated with long-chain hydrocarbons, the short alkenes that desorb from the iron surface are less likely to be re-adsorbed and incorporated into longer hydrocarbons. Consequently, at later time, the apparent concentrations of these short-chain hydrocarbons increase, and the observed probability of chain growth increases.

The final step required in a heterogeneous reaction is for the product to desorb from the surface; however, if long-chain hydrocarbons are forming on the iron surface, they will tend to remain there, and desorption could become the rate-limiting step in the reaction. The rate of chain termination for a given carbon number, $R_{t,n}$, is the sum of rates for the various chain termination pathways. As shown in Figure 7, these termination pathways include $\beta$-hydrogen abstraction to form an alkene, $R_o$, $\alpha$-hydrogen addition to form an alkane, $R_h$, and secondary reactions of 1-alkenes to form alkanes and internal alkenes. The transport-enhanced alkene readsorption model of Madon et al. (*40*) adds the additional parameter of alkene re-adsorption, $R_{r,n}$, which is carbon number dependent. Therefore, the rate of chain termination, $\beta_n$, can be expressed as

$$\beta_n = R_{t,n}/R_{p,n} = (R_h + R_o + R_s - R_{r,n})/R_{p,n} \quad (5)$$

As $R_{r,n}$ increases with $n$, the rate of chain termination will decrease, and the probability of chain growth for that carbon number, $\alpha_n$, will increase according to

$$\alpha_n = 1/(1 + \beta_n) \quad (6)$$

Eventually, a point is reached where the 1-alkenes for a given carbon number are completely consumed by these re-adsorption reactions. This point represents a minimum for the rate of chain termination, $\beta_n$, and a maximum for the probability of chain growth, $\alpha_n$. This conceptual model implies a deviation from an ASF distribution because of the increasing probability of chain growth with increasing carbon chain length. Therefore, the expected deviation from an ideal ASF distribution will result in even more carbon remaining sorbed to the surface as long hydrocarbon chains. The removal of these hydrocarbons from the surface may become the rate-limiting step in the reaction.

The hydrocarbons formed in gas phase Fischer–Tropsch synthesis, in the electroreduction of aqueous $CO_2$, and the short hydrocarbon chains detected in the iron and water systems of this study all have Anderson–Schulz–Flory product distributions, which suggest a common reaction mechanism. Kudo et al. (*32*), proposed a reaction mechanism for the reduction of aqueous $CO_2$ with nickel electrodes based on their experimental data, the existing electrochemical literature, and the reaction mechanisms known from Fischer–Tropsch synthesis. They concluded that the electroreduction of aqueous $CO_2$ proceeded through electron transfer to form either HCOOH or $CO_{(ads)}$. The carbon monoxide either desorbs as $CO_{(g)}$ or reacts with $H_{(ads)}$ from the reduction of water to form carbene groups, $-CH_2-$, which polymerize on the electrode surfadce to form hydrocarbons. Their reaction scheme (Figure 8) appears to be applicable to the iron and water system of this study with the slight modification that the electrons are provided by anaerobic corrosion rather than the application of an electric current. With the exception of Kudo et al., who reported the formation of methane and ethane in a control experiment with nickel electrodes, to our knowledge, the formation of hydrocarbon chains from the reduction of aqueous $CO_2$ without the application of electric current has not previously been reported.

**Unidentified Hydrocarbons.** An unidentified peak with a retention time between propene and 1-butene was noted on the PID in all batch experiments with the hydrogenated iron, and this peak was particularly prominent in samples collected from the column with electrolytic iron and $CaCO_3$ water. Though unconfirmed, this peak may be isobutene. A sample was sent to a commercial lab for gas chromatograph/mass spectrometer identification. Nothing was detectable in the sample; however, the method detection limit quoted by the lab for the GC/MS was approximately

3 orders of magnitude higher than that achieved with the PID or FID.

During the course of these studies, a large peak was intermittently detected on a Photovac 10S70 PID. This peak has the same retention time as formaldehyde, and its rapid disappearance is consistent with formaldehdye being oxidized to formate (*45*). The ionization potential of the PID is 10.6 eV, but the ionization potential of formaldehdye is 10.88 eV, indicating that formaldehyde should only be detectable if it is present in very high concentrations. The rapid disappearance of the peak made accurate quantification impossible on the PID. Attempts were made to derivatize the samples to allow analysis for low molecular weight aldehydes on an electron capture detector (*46*), but the results were inconclusive. The possible presence of formaldehyde may be significant because Pijolat et al. (*47*), in a study using an iron catalyst to hydrogenate gas phase $CO_2$, suggest that formate species re-activate the catalyst by reducing $Fe^{2+}$ back to $Fe^0$. This line of investigation was not pursued further in this study.

## Conclusions

Based on these investigations, we make the following conclusions.

(1) Hydrocarbons were formed by the reduction of aqueous $CO_2$ by iron metal. Ten hydrocarbons up to C5 were identified.

(2) The hydrocarbons detected appear to exhibit an Anderson–Schulz–Flory product distribution, which is well known in Fischer–Tropsch synthesis, where CO and $H_2$ are contacted with a catalyst to form long-chain hydrocarbons.

(3) Pretreating the iron with $H_2$ increased the total mass of hydrocarbons detected in solution, and increased the observed probability of chain growth. This indicates that adsorbed hydrogen is a reactant in the reduction of aqueous $CO_2$.

(4) Late time data from the commercial iron column experiment are comparable to published data on the electroreduction of aqueous $CO_2$ with iron electrodes and have a probability of chain growth for the C2–C5 hydrocarbons of $\alpha = 0.54$.

(5) In an ideal ASF distribution with a probability of chain growth of $\alpha = 0.54$, approximately 80% of the total hydrocarbon mass is between C1 and C4, and the remaining hydrocarbon mass is heavier than C4. Analyses are usually not conducted for these heavier hydrocarbons, and their increasing hydrophobicity makes it unlikely that they will be detectable in the water as they will tend to remain sorbed to the iron surface.

(4) The hydrocarbon concentrations and the observed probability of chain growth both increase with time. This slow approach to equilibrium may be related to the increasing hydrophobicity of the growing hydrocarbon chains on the surface of the iron. As the chain length increases, the probability that any alkenes formed will be re-adsorbed and incorporated into a longer hydrocarbon chain also increases; therefore, the probability of chain growth will increase with chain length until it reaches an asymptotic value. Based on this conceptual model, the expected deviation from an ideal ASF distribution will result in even more carbon remaining sorbed to the iron surface as long-chain hydrocarbons. Desorption of hydrocarbon products from the iron surface may become the rate-limiting step for iron-enhanced degradation of chlorinated organics.

(7) The overpotential applied to the $CO_2$/hydrocarbon couples by the anaerobic corrosion of zero-valent iron ($\approx$–0.3 V) is comparable to overpotentials quoted in the electrochemistry literature for the reduction of aqueous $CO_2$.

(8) Based on a reaction mechanism proposed for the electroreduction of aqueous $CO_2$ with nickel electrodes, the iron in this system acts as both a reactant, by corroding to supply electrons, and as a catalyst, by promoting the formation of hydrocarbons. Water is also a reactant in this system. Having successfully applied ASF distributions to systems containing iron, water, and $CO_2$, the concept can now be applied to iron and water systems with chlorinated organics present. Deviations from ASF distribution can be evaluated in relation to the proposed mechanism for the reduction of aqueous $CO_2$ and in the conceptual model of transport-enhanced alkene readsorption. An important consideration will be to determine if there is a compound or concentration dependence for the observed probability of chain growth, $\alpha$, and its affect on the carbon mass balance. While this work does not reveal how iron metal removes chlorines from chlorinated organics, it does indicate that catalysis may have important effects on the product distribution, the carbon mass balance, and possibly the reaction rate.

## Acknowledgments

The authors gratefully acknowledge the valuable discussions with Eric Reardon and Rick Devlin of the Department of Earth Sciences and the laboratory advice and assistance of Stephanie O'Hannesin, Greg Friday, and Wayne Noble. Financial support was provided through Research Grant A6414 of the Natural Sciences and Engineering Research Council of Canada.

## Literature Cited

(1) Mackay, D. M.; Cherry, J. A. *Environ. Sci. Technol.* **1989**, *23*, 630–636.
(2) Gillham, R. W.; Burris, D. R. Presented at the Subsurface Restoration Conference, Third International Conference on Ground Water Quality Research, Dallas, TX, 1994.
(3) Reynolds, G. W.; Hoff, J. T.; Gillham, R. W. *Environ. Sci. Technol.* **1990**, *24*, 135–142.
(4) Gillham, R. W.; O'Hannesin, S. F. Metal-catalyzed abiotic degradation of halogenated organic compounds. Presented at the IAH Conference on Modern Trends in Hydrogeology, Hamilton, Ontario, 1992.
(5) Gillham, R. W.; O'Hannesin, S. F. *Ground Water* **1994**, *32*, 958–967.
(6) Matheson, L. J.; Tratnyek, P. G. *Environ. Sci. Technol.* **1994**, *28*, 2045–2053.
(7) O'Hannesin, S. F. M.Sc. Thesis, University of Waterloo, 1993.
(8) O'Hannesin, S. F.; Gillham, R. W. A Permeable Reaction Wall for *in situ* Degradation of Halogenated Organic Compounds. Presented at the 45th Canadian Geotechnical Society Conference, Toronto, Ontario, 1992.
(9) Vogel, T. M.; Criddle, C. S.; McCarty, P. L. *Envion. Sci. Technol.* **1987**, *21*, 722–736.
(10) Jeffers, P. M.; Ward, L. M.; Woytowitch, L. M.; Wolfe, N. L. *Environ. Sci. Technol.* **1989**, *23*, 965–969.
(11) Roberts, L. A.; Gschwend, P. M. *Environ. Sci. Technol.* **1991**, *25*, 76–86.
(12) Barbash, J. E.; Reinhard, M. *Environ. Sci. Technol.* **1989**, *23*, 1349–1357.
(13) Schwarzenbach, R. P.; Stierli, R.; Lanz, K.; Zeyer, J. *Environ. Sci. Technol.* **1990**, *24*, 1566–1574.
(14) Dunnivant, F. M.; Schwarzenbach, R. P.; Macalady, D. L. *Environ. Sci. Technol.* **1992**, *26*, 2133–2141.
(15) Gantzer, C. J.; Wackett, L. P. *Environ. Sci. Technol.* **1991**, *25*, 715–722.
(16) Jafvert, C. T.; Wolfe, N. L. *Environ. Toxicol. Chem.* **1987**, *6*, 827–837.

(17) Ulrich, H. J.; Stone, A. T. *Environ. Sci. Technol.* **1989**, *23*, 421–428.
(18) Kriegman-King, M. R.; Reinhard, M. *Environ. Sci. Technol.* **1992**, *26*, 2198–2206.
(19) Kriegman-King, M. R.; Reinhard, M. *Environ. Sci. Technol.* **1994**, *28*, 692–700.
(20) Criddle, C. S.; McCarty, P. L. *Environ. Sci. Technol.* **1991**, *25*, 973–978.
(21) Kovenklioglu, S.; Cao, Z.; Shah, D.; Farrauto, R. J.; Balko, E. N. *AIChE J.* **1992**, *38*, 1003–1012.
(22) Senzaki, T.; Kumagi, Y. *Kogyo Yosui* **1988**, *357*, 2–7 (in Japanese).
(23) Henrici-Olivé, G.; Olivé, S. *Angew. Chem. Int. Ed. Engl.* **1976**, *15*, 136–141.
(24) MacKay, D.; Shiu, W. Y. *J. Phys. Chem. Ref. Data* **1981**, *10*, 1175–1199.
(25) Somorjai, G. A. *J. Phys. Chem.* **1990**, *94*, 1013–1023.
(26) Pankow, J. F. *Aquatic Chemistry Concepts*; Lewis: Boca Raton, 1993.
(27) Hori, Y.; Murata, A.; Takahashi, R.; Suzuki, S. *J. Am. Chem. Soc.* **1987**, *109*, 5022–5023.
(28) Stalder, C. J.; Chao, S.; Summers, D. P.; Wrighton, M. S. *J. Am. Chem. Soc.* **1983**, *105*, 6318–6320.
(29) Noda, H.; Ikeda, S.; Oda, Y.; Imal, K.; Maeda, M.; Ito, K. *Bull. Chem. Soc. Jpn.* **1990**, *63*, 2459–2462.
(30) Azuma, M.; Hashimoto, K.; Hiramoto, M.; Watanabe, M.; Sakata, T. *J. Electrochem. Soc.* **1990**, *137*, 1772–1778.
(31) Nakagawa, S.; Kudo, A.; Azuma, M.; Sakata, T. *J. Electroanal. Chem.* **1991**, *308*, 339–343.
(32) Kudo, A.; Nakagawa, S.; Tsuneto, A.; Sakata, T. *J. Electrochem. Soc.* **1993**, *140*, 1541–1545.
(33) Kyriacou, G.; Anagnostopoulos, A. *J. Electroanal. Chem.* **1992**, *322*, 233–246.
(34) Murata, A.; Hori, Y. *Bull. Chem. Soc. Jpn.* **1991**, *64*, 123–127.
(35) Kyriacou, G.; Anagnostopoulos, A. *J. Appl. Electrochem.* **1993**, *23*, 483–486.
(36) Azuma, M.; Hashimoto, K.; Watanabe, M.; Sakata, T. *J. Electroanal. Chem.* **1990**, *294*, 299–303.
(37) Hori, Y.; Murata, A.; Takahashi, R. *J. Chem. Soc., Faraday Trans. 1* **1989**, *85*, 2309–2326.
(38) Cook, R. L.; MacDuff, R. C.; Sammelis, A. F. *Proceedings of International Symposium on Chemical Fixation of Carbon Dioxide*, Nagoya, Japan, 1991; p 39.
(39) Somorjai, G. A.; Van Hove, M. A.; Bent, B. E. *J. Phys. Chem.* **1988**, *92*, 973–978.
(40) Madon, R. J.; Reyes, S. C.; Iglesia, E. *J. Phys. Chem.* **1991**, *95*, 7795–7804.
(41) Iglesia, E.; Reyes, S. C.; Madon, R. J. *J. Catal.* **1991**, *129*, 238–256.
(42) Puskas, I.; Hurlbut, R. S.; Pauls, R. E. *J. Catal.* **1993**, *139*, 591–601.
(43) Snel, R.; Zwart, J. *Appl. Catal.* **1986**, *22*, 337–343.
(44) Hindermann, J. P.; Hutchings, G. J.; Kiennemann, A. *Catal. Rev.* **1993**, *35*, 1–127.
(45) Schwarzenbach, R. P.; Gschwend, P. M.; Imboden, D. M. *Environmental Organic Chemistry*; Wiley-Interscience: New York, 1993.
(46) Glaze, W. H.; Koga, M.; Cancilla, D. *Environ. Sci. Technol.* **1989**, *23*, 838–847.
(47) Pijolat, M.; Perrichon, V.; Primet, M.; Bussiere, P. *J. Mol. Catal.* **1982**, *17*, 367–380.

*Received for review January 27, 1995. Revised manuscript received July 10, 1995. Accepted July 31, 1995.*[⊗]

ES950054M

[⊗] Abstract published in *Advance ACS Abstracts,* October 1, 1995.

PERGAMON

Chemosphere 49 (2002) 371–378

CHEMOSPHERE

www.elsevier.com/locate/chemosphere

# Enhanced dehalogenation of halogenated methanes by bimetallic Cu/Al

Hsing-Lung Lien *, Weixian Zhang

*Department of Civil and Environmental Engineering, National University of Kaohsiung, Kaohsiung, Taiwan*

Received 17 October 2001; received in revised form 4 June 2002; accepted 4 June 2002

**Abstract**

A low-cost and high effective copper/aluminum (Cu/Al) bimetal has been developed for treatments of halogenated methanes, including dichloromethane, in near neutral and high pH aqueous systems. Bimetallic Cu/Al was prepared by a simple two-step synthetic method where Cu was deposited onto the Al surface. The presence of Cu on Al significantly enhanced rates of degradation of halogenated methanes and reduced toxic halogenated intermediates. The stability of Cu/Al was preliminarily studied by a multi-spiking batch experiment where complete degradation of carbon tetrachloride was achieved for seven times although the Cu/Al aging was found. Roles of Cu may involve protecting Al against an undesirable oxidation with water, enhancing reaction rates through the galvanic corrosion, and increasing the selectivity to a benign compound (i.e., methane). Kinetic analyses indicated that the activity of bimetallic Cu/Al was comparable to that of iron-based bimetals (e.g., palladized iron) and zero-valent metals. Bimetallic Cu/Al could be a promising reactive reagent for remediation of halogenated solvents-contaminated groundwater associated with high pH problems.


*Keywords:* Bimetals; Aluminum; Zero-valent metals; Dichloromethane; Groundwater remediation

## 1. Introduction

Halogenated organic solvents have extensively been used for several decades in industrial applications such as the manufacture of refrigerants, herbicides, plastics, and solvents. Due to leaks, spills, and releases from industrial sources, they inevitably contaminate environments such as soil and groundwater. According to a study conducted by the US Geological Survey from 1985 to 1995, of 60 volatile organic compounds (VOCs), halogenated organic solvents such as carbon tetrachloride, chloroform, and trichloroethylene were among the most frequently detected VOCs in groundwater in urban and rural areas (Squillace et al., 1999). Because of inertness and toxicity, many halogenated organic solvents have been classified as priority pollutants including carbon tetrachloride and chloroform (US EPA, 1979).

Permeable reactive barriers (PRBs) represent a promising environmental remedial technology for remediation of groundwater contaminated with halogenated organic solvents (Puls et al., 1998; Liang et al., 2000). PRBs involve the placement or formation of a reactive treatment zone in the path of a contaminant plume in which groundwater passively moves while contaminants precipitate, adsorb or degrade. Treatment zones can be created by injecting reagents or by placing reactive solid-phase matrices into the subsurface. Substantial research efforts have been initiated over the past few years to identify reactive media that can be used in PRBs to treat halogenated organic solvents. Several different types of reactive media have been examined

* Corresponding author. Present address: Environmental Protection Agency, Robert S. Kerr Environmental Research Center, 919 Kerr Research Drive, Ada, OK 74820, USA. Tel.: +1-580-436-8740; fax: +1-580-436-8703.

*E-mail address:* lien.sam@nuk.gov (H.-L. Lien).

0045-6535/02/$ - see front matter 
PII: S0045-6535(02)00248-5

including zero-valent metals (e.g., Fe, Zn) (Gillham and O'Hannesin, 1994; Matheson and Tratnyek, 1994; Boronina et al., 1995; Roberts et al., 1996), bimetallic complexes (e.g., Pd/Fe, Pd/Zn) (Grittini et al., 1995; Muftikian et al., 1995; Fennelly and Roberts, 1998; Cheng and Wu, 2000), colloidal-size iron (Cantrell and Kaplan, 1997) and nanoscale iron materials (Lien and Zhang, 1999a, 2001). The reactive reagent most successfully deployed to date has been zero-valent iron (ZVI). ZVI has been demonstrated to be effective in removing a wide array of contaminants including halogenated organic solvents, heavy metals (Su and Puls, 2001), and radionuclides (Gu et al., 1998; Morrison et al., 2001).

Although ZVI has been shown a great success in treatments of many halogenated organic contaminants, very often it fails to degrade dichloromethane. For example, studies have shown that, of 14 halogenated organic compounds, only dichloromethane did not show measurable degradation by 100 mesh iron filings (Gillham and O'Hannesin, 1994). Similar results have also been observed in studies using bimetallic catalysts (Lien and Zhang, 1999a) and supported Pd catalysts (Lowry and Reinhard, 1999). The difficulty of the dichloromethane degradation tends to cause an incomplete degradation of carbon tetrachloride (Matheson and Tratnyek, 1994). Because complete degradation was not achieved, the accumulation of dichloromethane, which has the federal maximum contaminant levels of 5 μg/l, may require further treatments.

Another potential impact on ZVI is the high pH effect that deteriorates ZVI activity (Chen et al., 2001). The reductive degradation by ZVI involves metal corrosion for which ZVI serves as electron donors:

$$Fe^0 \rightarrow Fe^{2+} + 2e^- \quad (1)$$

This characteristic reaction of iron corrosion results in oxidative dissolution at near neutral pH. In aqueous systems, enhanced iron corrosion by water leads to increased pH and the formation of iron hydroxide precipitates:

$$Fe^0 + 2H_2O \rightarrow Fe^{2+} + H_2 + 2OH^- \quad (2)$$

The accumulation of hydroxide precipitates on the metal surface results in the loss of iron activity over time (Matheson and Tratnyek, 1994). Since the pH increase favors the formation of iron hydroxide, ZVI could not be the suitable reactive reagent at high pH. On the contrary, zero-valent aluminum may serve as a better reactive reagent under high pH conditions because the presence of $OH^-$ ions does not cause the formation of oxide precipitates but facilitates the removal of aluminum oxide (Birnbaum et al., 1997):

$$Al_2O_3 + 2OH^- \rightarrow 2AlO_2^- + H_2O \quad (3)$$

Therefore, the development of aluminum-based reactive media in PRBs may be a promising strategy to overcome high pH problems in groundwater remediation.

The use of aluminum-based bimetals for dehalogenation of chlorinated hydrocarbons has been reported (Schlimm and Heitz, 1996); however, investigation was conducted in the pH range of 4–7. We report here a bimetallic system of copper/aluminum complexes (Cu/Al) that effectively degraded halogenated methanes including dichloromethane under near neutral pH and high pH conditions. The bimetallic effect in dehalogenation has been shown that adding Pd, or Ni to Fe significantly increased the degradation rate in many halogenated organic solvents compared to the Fe alone (Grittini et al., 1995; Muftikian et al., 1995; Fennelly and Roberts, 1998; Lien and Zhang, 1999a). In this work, Cu was selected because of its low reduction potential (+0.34 V, relative to −1.662 V of aluminum). This property may better protect Al against undesirable side reactions (e.g., oxidation with water) when the bimetallic structure of Cu/Al is created. Moreover, Cu is known as a mild hydrogenation catalyst (Satterfield, 1991). It is effective for most of the elementary reactions that are required in catalytic dehalogenation (Yang et al., 1997). The deposited Cu may therefore be beneficial to the overall performance of bimetallic Cu/Al based on the catalytic property of Cu.

In this paper, a synthetic method of bimetallic Cu/Al is presented and the structure of Cu/Al was determined by X-ray diffraction (XRD). A multi-spiking test was performed to investigate the stability of Cu/Al. The results from batch experiments on the rate and extent of the halogenated methane transformation by Cu/Al are presented. Kinetic analysis was conducted by using pseudo-first-order rate equation and activity was expressed as both observed and surface-area-normalized rate constants.

## 2. Experimental

### 2.1. Materials

HPLC grade carbon tetrachloride, chloroform, dichloromethane, chloromethane, and bromoform were obtained from Aldrich. Methanol was purchased from Pharmco (ACS grade). A standard gas mixture containing methane, ethane, ethylene, and $C_3$–$C_4$ hydrocarbons (15 ppm each) was obtained from Supelco. Standard gases of 1.04% ethylene and 1.04% methane were acquired from Aldrich. Sodium hydroxide (98.7%) and cupric sulfate pentahydrate (99.8%) were acquired from J. T. Baker. Commercial grade aluminum metal (~20 μm) and copper powder were obtained from Aldrich and Fisher Scientific, respectively.

### 2.2. Preparation of bimetallic Cu/Al

Bimetallic Cu/Al was prepared in two simple steps at a fume hood. First, cupric sulfate gel was generated in an alkaline solution by adding 1.5 g of sodium hydroxide into a 30 ml of cupric sulfate solution (0.27 M). Next, metallic Cu was deposited onto the Al surface through a redox reaction. Five grams of Al metal was added into the gel and immediate fume evolution was observed. Copper ions ($Cu^{2+}$) underwent a fast reduction to $Cu^0$ by the oxidation of Al metal. While complete redox reaction was achieved, the gray aluminum was turned into black particles. Assuming that all the Cu metal was reductively precipitated onto the Al surface, the content of the Cu in the Al was calculated as 10% by weight. It is worth pointing out that an attempt to synthesize bimetallic Cu/Al through the reduction of $Cu^{2+}$ by Al under acidic conditions was unsuccessful. At low pH, monodispersed Cu particles instead of bimetallic particles were produced when cupric sulfate reacted with Al powders. Interestingly, the preparation of other aluminum-based bimetals such as Co/Al, Fe/Al, and Ni/Al was restricted to acidic conditions.

### 2.3. Batch system

Batch experiments were carried out in 150 ml serum bottles (Wheaton glass) containing 20 g/l of bimetallic Cu/Al. Stock solutions of halogenated methanes were prepared in methanol. For each bottle, 10 μl of stock solution was spiked into 50 ml of aqueous solution to achieve a desired initial concentration. The serum bottles were then capped with Teflon Mininert valves and mixed on a rotary shaker (30 rpm) at room temperature ($22 \pm 1$ °C). Batch bottles containing halogenated methanes in the absence of metal particles were used as controls. Analyses of organic mass in the controls indicated that the mass varied by less than 5% over the course of a typical experiment. Parallel experiments were also conducted to determine rates of the carbon tetrachloride degradation by Al and Cu alone. Solution pH was adjusted by HCl (1.0 N) and NaOH (1.0 N) prior to experiments.

### 2.4. Analyses

Halogenated methanes were analyzed by a headspace-gas chromatograph (GC) method. At selected time intervals, a 20 μl headspace gas aliquot was withdrawn by a gastight syringe for GC analysis. Headspace samples were analyzed by a HP5890 GC equipped with a DB-624 capillary column (J&W, 30 m × 0.32 mm) and an electron capture detector. Oven temperature was set at 50 °C for 10 min, injection port temperature was 180 °C, and detector temperature was 300 °C. Concentrations of halogenated methanes were determined by the external standard method using calibration curves. Calibration curves for each compound were made initially and the variability was checked daily before analysis (<15%). Since the solution/headspace ratio was identical between calibration and batch reaction systems, concentrations determined by the calibration curves account for vapor/water partitioning. It should be pointed out that no attempt was made to analyze the dimerization products such as hexachloroethane and tetrachloroethylene because dimerization reaction is not favored in dilute aqueous systems (Matheson and Tratnyek, 1994).

Hydrocarbon products in the headspace were analyzed with a Shimadzu GC equipped with a flame ionization detector (FID) and an AT-Q column (Alltech, 30 m × 0.32 mm). Oven, injection port, and detector temperature were set at 30, 250, and 300 °C, respectively. Hydrocarbons in the samples were identified by comparing GC retention times with standards (Supelco) and the GC was calibrated with gas standards (Aldrich). Aqueous concentrations were calculated using Henry's law constants (Mackay and Shiu, 1981).

### 2.5. Solid phase characterization

Speciation of Cu/Al at the metal surface was analyzed by a X-ray diffractometer MiniFlex (Rigaku Co.) at 30 keV and 15 mA. The instrument used copper target tube radiation (Cu $K_{\alpha 1}$) to produce X-rays with a wavelength of 1.54 Å. Samples were placed on a quartz plate and were scanned from 5° to 80° ($2\theta$) at a rate of 2° $2\theta$/min. The resultant XRD patterns were analyzed by XRD Pattern Processing, JADE® 5, Materials Data Inc. to calculate the interplanar spacings and relative intensities, and determine the $2\theta$ values of peaks. Total surface area of Cu/Al was measured by Auto III 9400 mercury porosimeter (Micromeritics Instrument Co.) with a maximum pressure of about 227, 370 kPa. The contact angle between mercury and the solid surface was set at 130°. Prior to measurement, Cu/Al particles were nitrogen-dried overnight under ambient temperature ($22 \pm 1$ °C). Average surface area of Cu/Al was determined to be about 5.31 $m^2$/g.

## 3. Results

XRD measurements were carried out to investigate the structure of Cu/Al bimetal. Fig. 1 illustrates the XRD patterns of Al metal (pattern a) and Cu/Al bimetal (pattern b). The characteristic peaks of Al metal appeared at 38.6°, 44.8°, 65.2°, and 78.4° as indicated by a square symbol and the peaks assigned to Cu were at the positions at 43.4°, 50.5°, and 74.1° as indicated by a circle symbol. In Fig. 1, the XRD pattern indicated that bimetallic Cu/Al consisted of metallic Al, metallic Cu, and

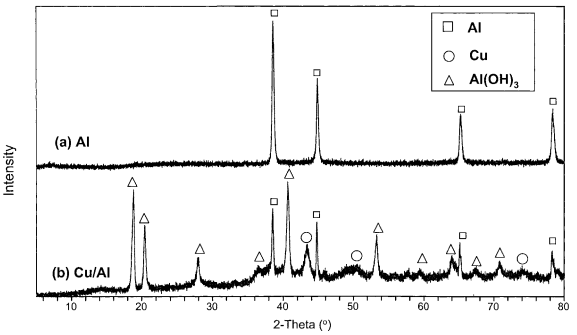


Fig. 1. XRD patterns of zero-valent Al and bimetallic Cu/Al.

aluminum hydroxide (Bayerite, $Al(OH)_3$). The characteristic peaks of aluminum hydroxide were assigned to 18.8°, 20.4°, 27.9°, 36.6°, 40.7°, 53.3°, 59.6°, 64.0°, 67.4°, and 70.8° as indicated by a triangle symbol. Aluminum hydroxide is a product from the redox reaction between Al and $Cu^{2+}$ during the formation of Cu/Al:

$$3Cu^{2+} + 2Al^0 + 6OH^- \rightarrow 3Cu^0 + 2Al(OH)_3 \quad (4)$$

Although no attempts were made to investigate the effect of aluminum hydroxide in this study, our early work showed that the presence of aluminum oxide tended to benefit the degradation of tetrachloroethylene with Al (Lien and Zhang, 1999b).

The reaction kinetics of the degradation of halogenated methanes was modeled with a pseudo-first-order rate equation. Plots of the natural logarithm of concentrations of halogenated methanes versus time through linear regression analysis gave straight line results. Linear regression analyses were used to obtain observed first-order rate constants ($k_{obs}$). Disappearance of carbon tetrachloride reacting with Cu/Al, Al, and Cu metals at pH 7.6 is plotted in the form of $\ln(C/C_0)$ as a function of time in Fig. 2 where $C_0$ is the initial concentration of carbon tetrachloride (31.8 mg/l). Data presented in Fig. 2 indicated that the disappearance of carbon tetrachloride exhibited pseudo-first-order behavior ($R^2 > 0.98$). Carbon tetrachloride was rapidly degraded by Cu/Al while a slow degradation of carbon tetrachloride by using Al alone was observed. No measurable degradation of carbon tetrachloride by Cu alone was found. Observed rate constants of Cu/Al and Al alone were 0.48 and 0.012 ($h^{-1}$), respectively. This indicated that Cu/Al increased the degradation rate by a factor of about 40 compared to Al alone.

Effects of pH on the activity of Cu/Al in reactions with carbon tetrachloride are shown in Fig. 3. Rates of carbon tetrachloride reduction increased by a factor of about 2.3 times when initial pH was increased from 7.6 to 9.2. Unlike ZVI that has been found to decrease rates as pH increased (Chen et al., 2001), Cu/Al exhibited

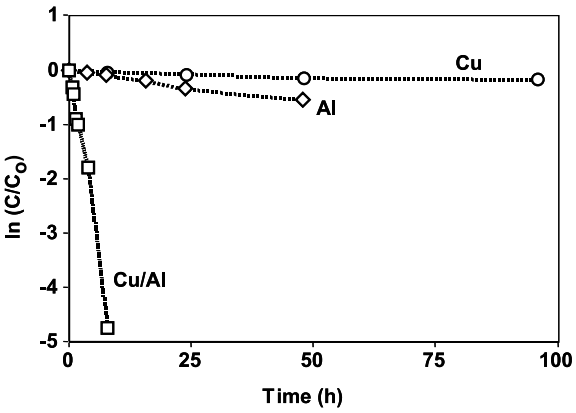


Fig. 2. Degradation of carbon tetrachloride (31.8 mg/l) by Cu/Al, Al, and Cu at pH 7.6. In all cases, batch experiments were conducted with 20 g/l of metal loading.

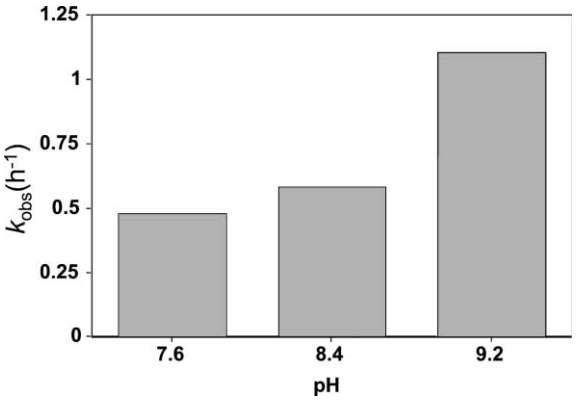


Fig. 3. Effect of pH on the carbon tetrachloride degradation by Cu/Al. Initial concentration of carbon tetrachloride was 31.8 mg/l and metal loading was 20 g/l.

higher rates of carbon tetrachloride reduction at increased pH. This suggests that Cu/Al may serve as a better reactive reagent for remediation of contaminated groundwater associated with high pH problems. Furthermore, an increase in pH throughout the experiment was found in all studies. During a 24-h reaction period, pH increased from 7.6, 8.4, and 9.2 to 8.6, 8.9, and 9.7, respectively.

Fig. 4 shows the time course of the product formation when degrading halogenated methanes by Cu/Al at pH 8.4. As shown in Fig. 4(a), carbon tetrachloride was completely degraded within 8 h while methane, chloroform, and dichloromethane were produced. Bimetallic Cu/Al gave a yield to methane of about 23%, whereas only trace amounts of chloroform and dichloromethane were detected (~1%) at the end of the experiment. Fig. 4(b) shows complete degradation of chloroform within 24 h. Dichloromethane and methane accounted for

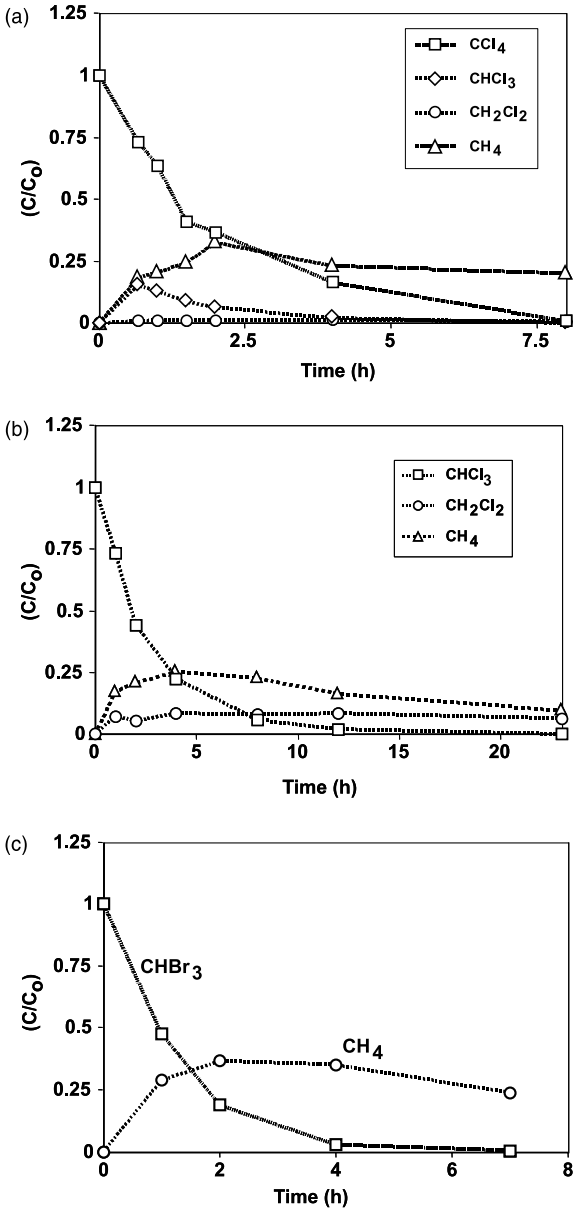


Fig. 4. Transformation of halogenated methanes by Cu/Al at pH 8.4. Metal loading was 20 g/l. (a) Carbon tetrachloride (31.8 mg/l), (b) chloroform (30.0 mg/l), and (c) bromoform (34.1 mg/l).

about 8.3% and 12.5% of the chloroform lost, respectively. The results for the degradation of bromoform are shown in Fig. 4(c). Bromoform was completely and rapidly degraded while no brominated intermediates such as dibromomethane were found. Methane was the only detectable product accounting for 35% of the bromoform lost. In all studies, minor amounts of hydrocarbons such as ethane and ethylene appeared briefly

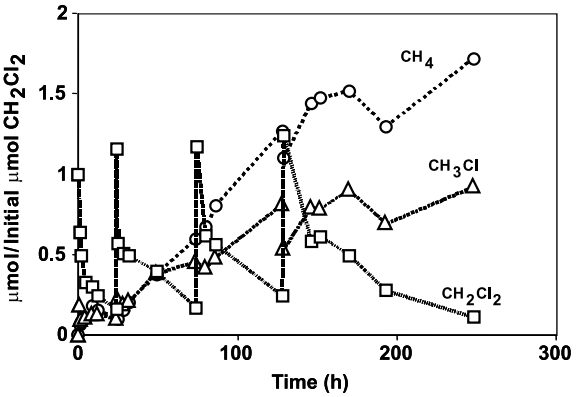


Fig. 5. Multi-spiking test for the transformation of dichloromethane by Cu/Al. The spiking amount of the reactant was 16 μmol for each cycle. Metal loading was 20 g/l.

in the headspace. For example, in the degradation of carbon tetrachloride, ethane and ethylene accounted for approximately 3% and less than 1% of the carbon tetrachloride lost, respectively.

To determine the capability of degrading dichloromethane by Cu/Al, experiments were conducted by repetitive spiking of dichloromethane into a batch bottle. The batch bottle containing 20 g/l of Cu/Al was spiked with 16 μmol of dichloromethane four times. Fig. 5 shows the normalized total μmol of dichloromethane and reaction products in the bottle as a function of time. A fast initial process followed by a slow subsequent process was found throughout the experiment while the accumulation of dehalogenation products (i.e., chloromethane and methane) was detected. The formation of these dehalogenation products indicated dichloromethane underwent a reductive dehalogenation reaction. The fast initial disappearance of dichloromethane implies that the removal of dichloromethane involves the sorption occurring initially. Similar results have been observed in many other surface-mediated processes where the rapid initial drop of reactants was attributed to the effect of sorption (Burris et al., 1998; Deng et al., 1999). A combination of sorption with dehalogenation reaction may account for the degradation of dichloromethane.

The above study was carried out by using fresh Cu/Al. From an application point of view, the length of time that Cu/Al can maintain its activity is an important concern. A multi-cycle experiment was executed to evaluate the stability of Cu/Al (Fig. 6). In this study, 10 μmol of carbon tetrachloride was repeatedly spiked into a batch system when complete degradation of carbon tetrachloride was achieved in each cycle. The total operation time was about 250 h, which corresponded to seven cycles. The Cu/Al aging was found in this study where the observed rate constant declined from about

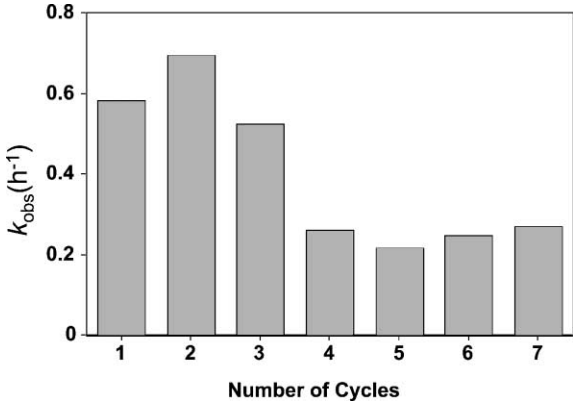


Fig. 6. Stability of bimetallic Cu/Al in the degradation of carbon tetrachloride. Ten μmol of carbon tetrachloride was added into the bottle for each cycle. Metal loading was 20 g/l.

0.58 ($h^{-1}$) at first cycle to 0.26 ($h^{-1}$) at fourth cycle. Nevertheless, activity of Cu/Al remained quite stable with an average observed rate constant of 0.26 ($h^{-1}$) from fourth cycle throughout the last. Compared to Al, Cu with the low reduction potential could better protect Al against undesirable oxidants such as oxygen and water. The presence of Cu on the Al surface clearly promotes the activity, stability, and usefulness of Cu/Al.

## 4. Discussion

The combination of Al with Cu significantly enhanced rates of the degradation of halogenated methanes compared to either Al or Cu alone. The poor performance of Al alone is a consequence of the formation of a protective oxide layer on the Al surface that inhibits the reducibility of Al at near neutral pH. Metallic Cu is incapable of serving as an effective reductant because of its low reduction potential. In contrast, the high activity of Cu/Al is attributed, at least in part, to the enhanced-bimetallic corrosion. In the bimetallic Cu/Al system, galvanic cells are created by coupling active metal (i.e., Al) with inert metal (i.e., Cu). The galvanic cells of Cu/Al couples lead to a significantly large potential gradient (~2.0 V) as compared to other bimetallic systems (e.g., 1.4 V of Pd/Fe bimetal). Elemental Al serves as the anode and becomes preferably oxidized in the galvanic cells while Cu serves as the cathode (Davis, 1999). In other words, the bimetallic structure of Cu/Al enhances the reducibility of Al for reductive dehalogenation by facilitating the Al corrosion.

The transformation of carbon tetrachloride has been proposed to proceed through different reaction pathways depending on the proton availability (Matheson and Tratnyek, 1994; Choi and Hoffmann, 1995). At low pH (proton-rich), carbon tetrachloride undergoes a hydrogenation to chloroform (Eq. (5)) while base-catalyzed hydrolysis of carbon tetrachloride to carbon monoxide occurs at high pH (proton-deficient) (Eqs. (6) and (7)):

$$CCl_4 + 2e^- + H^+ \rightarrow CHCl_3 + Cl^- \quad (5)$$

$$CCl_4 + 2e^- \rightarrow CCl_2 : + 2Cl^- \quad (6)$$

$$CCl_2 : + H_2O \rightarrow CO + 2HCl \quad (7)$$

In this study, the degradation of carbon tetrachloride by Cu/Al showed a relatively low carbon mass balance (28%) but a noticeable yield of methane (23%) at pH 8.4. The low mass balance of carbon, including only trace amounts of chloroform and dichloromethane, indicates Eq. (5) is a minor reaction. The rest of carbon (72%) may be attributed to the formation of non-halogenated products such as carbon monoxide according to Eqs. (6) and (7). They were undetectable by using the provided analytic methods. Similar results have been observed in the photoreduction of carbon tetrachloride at high pH (Choi and Hoffmann, 1995). In fact, hydrolysis being a separate reaction has been reported in many reductions with active metals in the absence of protons (Brewster, 1954).

On the other hand, relatively high yields of methane have commonly been observed in the catalytic dehalogenation of carbon tetrachloride using hydrogenation catalysts such as Pd (Lien and Zhang, 1999a; Lowry and Reinhard, 1999). Because Pd is incapable of transforming dichloromethane, step-wise formation of methane through a sequential dehalogenation of carbon tetrachloride is unlikely. Therefore, high yields of methane have been attributed to the direct transformation of carbon tetrachloride to methane at the surface of catalysts (Lowry and Reinhard, 1999). However, in the absence of catalysts, carbon tetrachloride reacting with ZVI underwent the sequential degradation to chloroform and dichloromethane while no yield of methane was observed (Matheson and Tratnyek, 1994). Bimetallic Cu/Al gave 23% yield to methane in the degradation of carbon tetrachloride suggesting that it is not a simple sequential dehalogenation. Since Cu acts as a hydrogenation catalyst (Yang et al., 1997), other reactions such as the direct transformation of carbon tetrachloride at the Cu/Al surface might be responsible for the formation of methane. Furthermore, Cu/Al would gain a great advantage over ZVI or Pd catalysts due to its capability of degrading dichloromethane. This capability may be attributed to synergistic effects between Cu catalysis and high reducibility of Al through galvanic cells of Cu/Al couples.

To better compare bimetallic Cu/Al with other types of metals, it is useful to normalize observed rate constants in accordance with activity per unit metal surface area. Surface-area-normalized rate constant proposed

Table 1
Observed and surface-area-normalized rate constants for halogenated methanes

| Compounds | $k_{obs}$ ($h^{-1}$)[a] | $k_{SA}$ (l/h/$m^2$)[a] | ($R^2$)[a] | $k_{SA}$ (l/h/$m^2$ )[b] | $k_{SA}$ (l/h/$m^2$)[c] |
|---|---|---|---|---|---|
| $CCl_4$ | 0.58 | $5.5 \times 10^{-3}$ | 0.985 | $(1.2 \pm 1.5) \times 10^{-1}$ | $9.0 \times 10^{-3}$ |
| $CHCl_3$ | 0.32 | $3.1 \times 10^{-3}$ | 0.994 | $(9.2 \pm 7.3) \times 10^{-4}$ | $6.5 \times 10^{-3}$ |
| $CH_2Cl_2$ | 0.066 | $6.2 \times 10^{-4}$ | 0.800 | NR[d] | NR[d] |
| $CHBr_3$ | 0.85 | $7.9 \times 10^{-3}$ | 0.997 | $1.7 \times 10^{-2}$ | – |

[a] This study.
[b] ZVI, data from Johnson et al. (1996) except for $CH_2Cl_2$ obtained from Gillham and O'Hannesin (1994).
[c] Nanoscale Pd/Fe, data from Lien and Zhang (1999a).
[d] NR: no reaction.

by Johnson et al. (1996) has widely been used for this purpose:

$$k_{SA} = \frac{k_{obs}}{a_s \rho} \tag{8}$$

where $k_{SA}$ is the surface-area-normalized rate constant (l/h/$m^2$); $k_{obs}$ is the observed first-order rate constant; $a_s$ is the specific surface area of metal ($m^2$/g); $\rho$ is the mass concentration of metal (g/l). In the case of this study, $a_s$ and $\rho$ were 5.31 ($m^2$/g) and 20 (g/l), respectively. The observed first-order rate constants for the degradation of halogenated methanes by Cu/Al determined by linear regression analysis of the experimental data are given in Table 1. The values of $k_{SA}$ can therefore be determined according to Eq. (8). Table 1 also lists literature $k_{SA}$ values for granular iron (Johnson et al., 1996) and nanoscale Pd/Fe particles (Lien and Zhang, 1999a).

The disappearance of carbon tetrachloride, chloroform, and bromoform exhibited pseudo-first-order behavior ($R^2 > 0.98$) whereas a poor coefficient of determination ($R^2 = 0.80$) indicated that the overall reaction of dichloromethane was not pseudo-first-order (Table 1). Since the dehalogenation of dichloromethane was a slow process compared to that of carbon tetrachloride or chloroform, the fast initial sorption process became a significant factor influencing the data linearization in accordance with pseudo-first-order kinetics. As a result, the linearization of the measured data reflecting mixed effects of sorption and reactions did not exhibit pseudo-first-order behavior.

Nanoscale Pd/Fe particles have been shown to degrade chlorinated methanes and ethylenes more effectively than granular iron although some literature data reported a significantly high reactivity of carbon tetrachloride reacting with granular iron (Johnson et al., 1996; Lien and Zhang, 1999a, 2001). The activity of bimetallic Cu/Al in reactions with halogenated methanes was comparable with that of nanoscale Pd/Fe particles and granular iron (Table 1). Considered the low cost of copper (relative to palladium) and its high activity, Cu/Al could be a promising reactive reagent for remediation of groundwater contaminated with halogenated methanes.

## 5. Conclusions

The present investigation on the degradation of halogenated methanes indicates the potential application of bimetallic Cu/Al for groundwater remediation. It has great potential for serving as a reactive reagent in PRBs. Bimetallic Cu/Al effectively degraded halogenated methanes under high pH conditions where conventional reagents such as zero-valent iron are deteriorated. Moreover, bimetallic Cu/Al showed capability of degrading dichloromethane, a recalcitrant contaminant that cannot be degraded by zero-valent metals. Advantages of bimetallic Cu/Al also include (i) high activity and stability for the degradation of halogenated organic solvents in aqueous solutions; (ii) low production of toxic intermediates; and (iii) cost-effectiveness. However, before this technology can be fully optimized for environmental applications, further study is needed. Important questions that need to be investigated include (i) effects of environmental factors on long-term performance of bimetallic Cu/Al, (ii) effects of Cu to Al ratio on Cu/Al activity, (iii) mass balance of reaction products, and (iv) the potential production of dissolved metals (e.g., $Cu^{2+}$ and $Al^{3+}$).

## Acknowledgements

H.L. wishes to thank Dr Rick Wilkin of Robert S. Kerr Environmental Research Center, US Environmental Protection Agency for his assistance in conducting the XRD analysis.

## References

Birnbaum, H.K., Buckley, C., Zeides, F., Sirois, E., Rozenak, P., Spooner, S., Lin, J.S., 1997. Hydrogen in aluminum. J. Alloy Compd. 253–254, 260–264.

Boronina, T., Klabunde, K.J., Sergeev, G., 1995. Destruction of organohalides in water using metal particles: Carbon tetrachloride/water reactions with magnesium, tin, and zinc. Environ. Sci. Technol. 29, 1511–1517.

Brewster, J.H., 1954. Mechanisms of reductions at metal surfaces. I. A general working hypothesis. J. Am. Chem. Soc. 76, 6361–6363.

Burris, D.R., Allen-King, R.M., Manoranjan, V.S., Campbell, T.J., Loraine, G.A., Deng, B., 1998. Chlorinated ethene reduction by cast iron: Sorption, and mass transfer. J. Environ. Eng. 124, 1012–1019.

Cantrell, K.J., Kaplan, D.I., 1997. Zero-valent iron colloid emplacement in sand columns. J. Environ. Eng. 123, 499–505.

Chen, J., Al-Abed, S.R., Ryan, J.A., Li, Z., 2001. Effects of pH on degradation of trichloroethylene by zero-valent iron. J. Hazard. Mater. B83, 243–254.

Cheng, S.F., Wu, S.C., 2000. The enhancement methods for the degradation of TCE by zero-valent metals. Chemosphere 41, 163–1270.

Choi, W., Hoffmann, M.R., 1995. Photoreductive mechanism of $CCl_4$ degradation on $TiO_2$ particles and effects of electron donors. Environ. Sci. Technol. 29, 1646–1654.

Davis, J.R. (Ed.), 1999. Corrosion of Aluminum and Aluminum Alloys. ASM International, Materials Park, OH.

Deng, B., Burris, D.R., Campbell, T.J., 1999. Reduction of vinyl chloride in metallic iron–water systems. Environ. Sci. Technol. 33, 2651–2656.

Fennelly, J.P., Roberts, A.L., 1998. Reaction of 1,1,1-trichloroethane with zero-valent metals and bimetallic reductants. Environ. Sci. Technol. 32, 1980–1988.

Gillham, R.W., O'Hannesin, S.F., 1994. Enhanced degradation of halogenated aliphatics by zero-valent iron. Ground Water 32, 958–967.

Grittini, C., Malcomson, M., Fernando, Q., Korte, N., 1995. Rapid dechlorination of polychlorinated biphenyls on the surface of a Pd/Fe bimetallic system. Environ. Sci. Technol. 29, 2898–2900.

Gu, B., Liang, L., Dickey, M.J., Yin, X., Dai, S., 1998. Reductive precipitation of uranium(VI) by zero-valent iron. Environ. Sci. Technol. 32, 3366–3373.

Johnson, T.L., Scherer, M.M., Tratnyek, P.G., 1996. Kinetics of halogenated organic compound degradation by iron metal. Environ. Sci. Technol. 30, 2634–2640.

Liang, L., Korte, N., Gu, B., Puls, R., Reeter, C., 2000. Geochemical and microbial reactions affecting the long-term performance of in situ "iron barriers". Adv. Environ. Res. 4, 273–286.

Lien, H.L., Zhang, W., 1999a. Transformation of chlorinated methanes by nanoscale iron particles. J. Environ. Eng. 125, 1042–1047.

Lien, H.L., Zhang, W., 1999b. Activated $Al/Al_2O_3$ for transformation of chlorinated hydrocarbons. In: Proceedings of the 1999 ASCE–CSCE National Conference on Environmental Engineering, Norfolk, VA, pp. 827–831.

Lien, H.L., Zhang, W., 2001. Nanoscale iron particles for complete reduction of chlorinated ethenes. Colloid Surface A: Physiochem. Eng. Aspects 191, 97–106.

Lowry, G.V., Reinhard, M., 1999. Hydrodehalogenation of 1- to 3-carbon halogenated organic compounds in water using a palladium catalyst and hydrogen gas. Environ. Sci. Technol. 33, 1905–1910.

Mackay, D., Shiu, W.Y., 1981. A critical review of Henry's law constants for chemicals of environmental interest. J. Phys. Chem. Ref. Data 10, 1175–1199.

Matheson, L.J., Tratnyek, P.G., 1994. Reductive dehalogenation of chlorinated methanes by iron metal. Environ. Sci. Technol. 28, 2045–2053.

Morrison, S.J., Metzler, D.R., Carpenter, C.E., 2001. Uranium precipitation in a permeable reactive barrier by progressive irreversible dissolution of zerovalent iron. Environ. Sci. Technol. 35, 385–390.

Muftikian, R., Fernando, Q., Korte, N., 1995. A method for the rapid dechlorination of low molecular weight chlorinated hydrocarbons in water. Water Res. 29, 2434–2439.

Puls, R.W., Powell, R.M., Blowes, D.W., Gillham, R.W., Schultz, D., Sivavec, T., Vogan, J.L., Powell, P.D., Landis, R., 1998. Permeable Reactive Barrier Technologies for Contaminant Remediation. EPA/600/R-98-125, Office of Research and Development, Washington, DC.

Roberts, A.L., Totten, L.A., Arnold, W.A., Burris, D.R., Campbell, T.J., 1996. Reductive elimination of chlorinated ethylenes by zero-valent metals. Environ. Sci. Technol. 30, 2654–2659.

Satterfield, C.N., 1991. Heterogeneous Catalysis in Industrial Practice, second ed. McGraw-Hill, Inc., New York, NY.

Schlimm, C., Heitz, E., 1996. Development of a wastewater treatment process: Reductive dehalogenation of chlorinated hydrocarbons by metals. Environ. Prog. 15 (1), 38–46.

Squillace, P.J., Moran, M.J., Lapham, W.W., Price, C.V., Clawges, R.M., Zogorski, J.S., 1999. Volatile organic compounds in untreated ambient groundwater of the United States, 1985–1995. Environ. Sci. Technol. 33, 4176–4187.

Su, C., Puls, R.W., 2001. Arsenate and arsenite removal by zerovalent iron: Kinetics, redox transformation, and implications for in situ groundwater remediation. Environ. Sci. Technol. 35, 1487–1492.

US EPA, 1979. Water-Related Environmental Fate of 129 Priority Pollutants. Vol. II: Halogenated Aliphatic Hydrocarbons, Halogenated Ethers, Monocyclic Aromatics, Phthalate Esters, Polycyclic Aromatic Hydrocarbons, Nitrosamines, and Miscellaneous Compounds. Washington, DC. Office of Water Planning and Standards, US Environmental Protection Agency, EPA-440/4-79-029B.

Yang, M.X., Sarkar, S., Bent, B.E., 1997. Degradation of multiply-chlorinated hydrocarbons on Cu(100). Langmuir 13, 229–242.

KINETICS, CATALYSIS, AND REACTION ENGINEERING

# Decomposition of Formic Acid under Hydrothermal Conditions

**Jianli Yu and Phillip E. Savage***

*Department of Chemical Engineering, The University of Michigan, Ann Arbor, Michigan 48109-2136*

The thermal decomposition of formic acid was studied in dilute aqueous solutions and in the absence of added oxygen at temperatures between 320 and 500 °C and pressures between 178 and 303 atm for residence times between 1.4 and 80 s. Under these conditions, the formic acid conversion ranged from 38% to 100%, and the major products were always $CO_2$ and $H_2$, which indicates that decarboxylation is the preferred reaction path for formic acid decomposition under hydrothermal conditions. CO also appeared as a product, which shows that a dehydration path is available, but the CO yield was always at least an order of magnitude lower than the yields of $CO_2$ and $H_2$. The kinetics of formic acid disappearance and product formation at temperatures above 320 °C are consistent with a reaction rate law that is first order in formic acid. The implications of the present results to the generally accepted molecular decomposition mechanism are discussed, as are the alternative free-radical, ionic, and surface-catalyzed reaction mechanisms proposed in the literature.

## Introduction

Water at elevated temperatures and pressures continues to be explored as a chemical reaction medium (Savage et al., 1995; Katritzky et al., 1996; Mishra et al., 1995). One technological application that exploits oxidation reactions in water near its critical point ($T_c$ = 374 °C, $P_c$ = 218 atm) involves the safe conversion of organic wastes into innocuous compounds. When this chemical conversion occurs below the critical point of water, the technology is referred to as wet air oxidation. When the conversion occurs above the critical point of water, the technology is referred to as supercritical water oxidation. Regardless of the specific temperature and pressure of the aqueous reaction medium, however, carboxylic acids are frequently observed intermediate products from the hydrothermal oxidation of a wide variety of organic compounds and wastes (Thornton and Savage, 1990; Copa and Gitchel, 1989). As a consequence, a knowledge of the decomposition pathways, kinetics, and mechanisms for organic acids in high-temperature water is useful. In this paper we focus on the decomposition of the simplest organic acid, formic acid, in both sub- and supercritical water.

Although the literature provides experimental results for formic acid decomposition in the gas phase (Blake and Hinshelwood, 1960; Blake et al., 1971; Saito et al., 1984; Hsu et al., 1982) and formic acid oxidation in aqueous solutions (Wightman, 1981; Mishra et al., 1995), it provides much less information on the decomposition of formic acid in hot, aqueous solutions in the absence of added oxygen. Bjerre and Sørensen (1992) conducted two such experiments at 260 °C and in new and used reactors. The experiment in the used reactor resulted in a higher formic acid conversion, higher yields of $CO_2$ and $H_2$, and a lower yield of CO. In both reactors, however, the yield of $CO_2$ always exceeded that of CO. The authors attributed the differences in the results obtained from the two different reactors to the surface of the used reactor being rough and corroded and thereby influencing the reaction. Brill et al. (1996) reported preliminary results on the hydrothermal decomposition of formic acid up to 330 °C. They reported only the $CO_2$ concentration, and they observed that the temporal variation of the $CO_2$ concentration showed three distinct phases. The initial stage, which was not unimolecular, showed a monotonic increase in the $CO_2$ concentration with time. A second quiescent stage, where little conversion occurs, appeared next, and then a final explosive stage appeared, wherein decomposition is very rapid. These authors noted the similarity in these results to those reported by Falconer and Madix (1974) for the decomposition of formic acid on clean Ni(110) surfaces at $10^{-7}$ Torr and 100−125 °C and suggested that surface reactions were important in their hydrothermal reactor.

The present paper expands upon these two previous hydrothermal reaction studies and further broadens the field. We provide experimental data for the yields of formic acid and all of its major decomposition products as functions of time. Our experimental conditions include temperatures up to 500 °C, which is 170 °C higher than any previous hydrothermal studies. We explore the effects of temperature, pressure (or water density), and reactor surface/volume ratio and provide a quantitative kinetics analysis of formic acid decomposition under hydrothermal conditions.

## Experimental Section

Formic acid was obtained from Aldrich in a nominal purity of 95−97% and used as received. An aqueous stock solution containing about 1000 ppm formic acid

* Corresponding author. E-mail: psavage@umich.edu. Phone: (313) 764-3386. Fax: (313) 763-0459.

S0888-5885(97)00182-6 CCC: $15.00 
Published on Web 01/05/1998

was prepared with distilled, deionized, degassed water. This dilute aqueous solution served as the reactor feed, and it was loaded into a 1 gal pressure vessel blanketed with 500 psi helium before beginning an experiment.

Reactions were accomplished in a Hastelloy C-276 tubular flow reactor system, which has been previously described in detail (Thornton and Savage, 1990). The system comprises a nominal preheat section (1.08 mm i.d.) and a nominal reactor section joined to one another with a Hastelloy block that was fitted with a thermocouple. All reaction temperatures reported in this paper are the temperatures detected by this thermocouple. One of the reactors was 1 m long with 1.40 mm i.d., and a second reactor was 1.74 m long with 1.08 mm i.d. The tubular reactor system is immersed in a temperature-controlled (Techne TC-8D) fluidized bath (Techne SBL-2) of aluminum oxide particles. The nominal pressure and temperature were constant in the reactor section during each experiment. The formic acid solution was fed through the preheat line and then into the reactor tube by an Eldex high-pressure liquid chromatography pump. After leaving the heated reactor, the reactor effluent was rapidly cooled in a heat exchanger, depressurized, and then separated into gas and liquid phases at ambient conditions.

The vapor phase was directed to a 10-port Valco valve, which injected a known volume of gas (either 0.50 or 0.156 mL) into a Hewlett Packard Model 5890 series II gas chromatograph (GC) equipped with a thermal conductivity detector. Sample constituents were separated on a 10 ft. $\times$ $^1/_8$ in. o.d. stainless steel column packed with 100/120 mesh Supelco Carboseive S-II. Peak areas were calculated and reported by an HP 3392A integrator. The detector polarity was reversed before the hydrogen peak appeared so we could quantify the yield of hydrogen. The oven temperature was 35 °C for the first 7 min, and it then increased 16 °C/min until it reached 225 °C. Helium flowing at 20 mL/min served as the carrier gas. The flow rate of the vapor-phase reactor effluent was measured by using a soap-film flow meter.

The flow rate of the liquid-phase reactor effluent was determined by measuring the time required to fill a graduated cylinder of known volume. Samples of the liquid phase were collected and analyzed by a Waters high-performance liquid chromatograph (HPLC) equipped with a Supelco C610H gel column and operated isocratically with UV detection at 210 nm. The mobile phase was an aqueous solution of 0.1% $H_3PO_4$.

Both the GC and HPLC were calibrated by determining the detector response for sets of standards with known amounts of CO, $CO_2$, and $H_2$ (for the GC) and formic acid (for the HPLC). We typically made two independent measurements of the gas- and liquid-phase flow rates and compositions for each steady-state reaction condition. Molar yields of products were calculated as the molar flow rate of the product in the reactor effluent divided by the molar flow rate of reactant into the reactor. The molar yields calculated from the analytical results for the replicate samples always agreed to within a few percent. We assumed that the effluent gas and liquid streams are in equilibrium when these phases separate at ambient conditions, and we used Henry's law to calculate the amount of dissolved gases in the liquid phase. We also calculated the carbon balance as the percentage of carbon atoms in the feed that appear in quantified products in the reactor effluent.

The residence times reported for these experiments were calculated as the combined volume of the reactor and preheater sections divided by the volumetric flow rate of the fluid at the nominal reaction conditions less an estimated preheat time. The preheat time was taken to be constant for a given reaction temperature. It was calculated as the amount of time the flowing fluid spent in the preheater at the highest flow rate used in the experiments. We verified experimentally that this amount of time was sufficient to preheat the feed to the reaction temperature at the high flow rate. These preheat times were typically between 1 and 2 s. Given the weak sensitivity of the heat-transfer coefficient to the flow rate and the precise position in the preheater tubing (Holgate et al., 1992), we expect the preheat time to be only a weak function of the flow rate and hence roughly constant during a set of experiments at a fixed temperature. This approach provides a consistent basis for calculating the residence time.

## Results

Tables 1 and 2 display the experimental conditions investigated and the results obtained in this study of the decomposition of formic acid under hydrothermal conditions. The results in Table 1 were obtained from a reactor with 1.40 mm i.d., whereas the results in Table 2 were obtained from a reactor with 1.08 mm i.d. In most cases, the results in Tables 1 and 2 are average values calculated from flow rate measurements and analyses of two, and at times four, different gas- and liquid-phase samples collected at the same nominal steady-state reaction conditions. We excluded from these tables results from experiments with carbon balances less than 85%. Only 8 of the roughly 150 data sets suffered from low carbon balances, and all eight of these data sets were from experiments run at low flow rates where the uncertainty in the gas-phase flow rate measurement is highest.

$CO_2$ is the major carbon-containing reaction product under all conditions studied. The yield of $CO_2$ is always at least an order of magnitude higher than the yield of CO. This high selectivity to $CO_2$ under hydrothermal conditions is consistent with the results of Brill et al. (1996) and Bjerre and Sørensen (1992). This result stands in contrast with previous gas-phase studies, however, where CO is the major product (Blake and Hinshelwood, 1960; Blake et al., 1971; Saito et al., 1984; Hsu et al., 1982). In a subsequent section of this paper we discuss reasons for this difference in the product spectrum for the hydrothermal and gas-phase decomposition.

If formic acid decomposes to form $CO_2$ as a major product, then stoichiometry demands that $H_2$ also be formed in equal yields. We were able to quantify the $H_2$ yields, and the results appear in Tables 1 and 2. The $H_2$ yield is always high and close to the value of the $CO_2$ yield. In fact, the $CO_2/H_2$ ratio is typically between 0.9 and 1.2, which shows that these two products appear in roughly equal yields. We estimate the uncertainty in the $CO_2$ and $H_2$ yields to be $\pm$10% and $\pm$15% of the reported values, respectively. These individual uncertainties lead to a relative uncertainty of 18% in the $CO_2/H_2$ ratio, which implies that nearly all of the experimental results possess a $CO_2/H_2$ ratio that includes the

**Table 1. Formic Acid Decomposition at 250 atm and Different Temperatures**

| reaction temp (°C) | residence time (s) | formic acid conc. (mmol/L) | water conc. (mol/L) | formic acid conv. (%) | CO yield (%) | $CO_2$ yield (%) | $H_2$ yield (%) | carbon balance (%) |
|---|---|---|---|---|---|---|---|---|
| 321 | 15.4 | 15.7 | 39.0 | 69 | 0.9 | 63 | 67 | 95 |
| 321 | 20.1 | 15.7 | 38.9 | 71 | 1.1 | 66 | 70 | 96 |
| 321 | 27.6 | 15.7 | 38.9 | 76 | 1.3 | 67 | 65 | 92 |
| 322 | 45.8 | 15.7 | 38.9 | 86 | 1.6 | 71 | 74 | 86 |
| 339 | 12.7 | 10.4 | 36.5 | 71 | 2.0 | 78 | 104 | 108 |
| 340 | 13.8 | 10.4 | 36.5 | 76 | 1.6 | 70 | 69 | 95 |
| 340 | 16.0 | 10.4 | 36.4 | 79 | 1.7 | 72 | 71 | 94 |
| 340 | 18.8 | 10.4 | 36.4 | 84 | 2.1 | 79 | 81 | 97 |
| 340 | 23.6 | 10.4 | 36.4 | 90 | 2.9 | 84 | 89 | 98 |
| 341 | 34.0 | 10.4 | 36.3 | 100 | 3.9 | 94 | 101 | 98 |
| 358 | 6.5 | 13.3 | 33.2 | 38 | 1.4 | 42 | 32 | 106 |
| 358 | 8.4 | 13.3 | 33.1 | 46 | 1.6 | 48 | 39 | 103 |
| 359 | 11.0 | 13.2 | 33.0 | 55 | 1.8 | 54 | 47 | 101 |
| 360 | 16.1 | 13.1 | 32.8 | 70 | 1.9 | 67 | 61 | 100 |
| 361 | 37.1 | 13.1 | 32.6 | 98 | 2.4 | 84 | 92 | 88 |
| 378 | 3.4 | 10.6 | 26.7 | 41 | 1.1 | 47 | 37 | 107 |
| 380 | 3.9 | 10.1 | 25.5 | 49 | 1.3 | 52 | 43 | 104 |
| 379 | 5.1 | 10.3 | 26.1 | 55 | 1.5 | 55 | 48 | 101 |
| 380 | 6.9 | 10.3 | 25.9 | 65 | 1.6 | 59 | 50 | 95 |
| 379 | 10.1 | 10.5 | 26.4 | 77 | 2.2 | 71 | 69 | 96 |
| 380 | 17.5 | 10.1 | 25.4 | 95 | 3.1 | 88 | 92 | 96 |
| 397 | 1.9 | 2.9 | 10.2 | 96 | 1.3 | 90 | 92 | 95 |
| 395 | 2.6 | 3.1 | 10.9 | 97 | 1.5 | 90 | 100 | 95 |
| 396 | 3.3 | 3.0 | 10.6 | 97 | 1.5 | 92 | 95 | 97 |
| 399 | 3.8 | 2.9 | 9.89 | 99 | 1.3 | 92 | 99 | 95 |
| 399 | 4.9 | 2.8 | 9.73 | 100 | 1.2 | 91 | 96 | 93 |
| 400 | 6.8 | 2.8 | 9.55 | 100 | 1.3 | 94 | 102 | 96 |
| 420 | 2.4 | 2.2 | 7.48 | 85 | 5.0 | 73 | 79 | 93 |
| 420 | 3.4 | 2.2 | 7.48 | 90 | 5.8 | 77 | 79 | 93 |
| 420 | 5.0 | 2.2 | 7.48 | 100 | 5.9 | 82 | 86 | 87 |
| 461 | 1.5 | 1.7 | 5.85 | 100 | 5.9 | 89 | 97 | 95 |
| 461 | 1.9 | 1.7 | 5.86 | 100 | 5.4 | 90 | 97 | 95 |
| 461 | 2.5 | 1.7 | 5.86 | 100 | 5.2 | 88 | 98 | 93 |
| 463 | 3.4 | 1.7 | 5.81 | 100 | 5.1 | 87 | 95 | 92 |
| 461 | 5.5 | 1.7 | 5.85 | 100 | 6.5 | 83 | 85 | 89 |
| 480 | 1.5 | 1.6 | 5.42 | 100 | 4.2 | 89 | 99 | 93 |
| 481 | 1.9 | 1.6 | 5.42 | 100 | 3.3 | 88 | 101 | 91 |
| 482 | 2.5 | 1.6 | 5.40 | 100 | 2.7 | 88 | 98 | 91 |
| 481 | 3.8 | 1.6 | 5.42 | 100 | 2.6 | 86 | 93 | 89 |
| 501 | 1.4 | 1.5 | 5.06 | 100 | 3.7 | 89 | 99 | 93 |
| 501 | 1.8 | 1.5 | 5.05 | 100 | 2.7 | 91 | 98 | 93 |
| 501 | 2.5 | 1.5 | 5.06 | 100 | 1.9 | 91 | 97 | 92 |
| 501 | 3.6 | 1.5 | 5.06 | 100 | 2.0 | 87 | 83 | 89 |

expected value of unity within their experimental uncertainties.

Figure 1 displays the temporal variations of the molar yields of the major carbon-containing products from formic acid decomposition at 250 atm and at 360, 380, and 420 °C. At all three temperatures, the formic acid yield steadily decreases with time while the $CO_2$ yield steadily increases. The yield of CO also increases with time, but the CO yield is much lower than the $CO_2$ yield. The monotonic trends in the product yields apparent in Figure 1 and in Tables 1 and 2 differ from the trends observed by Brill et al. (1996). As mentioned in the Introduction section, these investigators found that the $CO_2$ temporal profile exhibited three distinct regions. In the initial region the $CO_2$ yield increased monotonically, in the second region a "quiescent" period appeared wherein the $CO_2$ yield remained largely unchanged as the residence time increased, and in the final region an "explosive" increase in $CO_2$ production was observed. We found no need to invoke the existence of three different reaction stages to explain the formic acid decomposition data reported herein.

## Reaction Kinetics

The analysis in this section focuses on the kinetics of formic acid disappearance. We first determine the reaction order and then the rate constant at several of the temperatures investigated.

The global reaction order, $n$, for formic acid disappearance can be determined by assessing the effect of the formic acid concentration, $C$, on the reaction rate.

$$\text{rate} = kC^n$$

To this end, we conducted a set of experiments at 360 °C and 250 atm wherein the concentration of formic acid in the reactor feed stream was varied by an order of magnitude but all other process variables (flow rate, temperature, pressure) remained unchanged. Each experiment provided the formic acid conversion, $X$, from which we calculated the pseudo-first-order rate constant, $k'$, for formic acid disappearance as

$$k' = \frac{-\ln(1 - X)}{\tau}$$

**Table 2. Formic Acid Decomposition at 380 °C and Different Pressures**

| reaction pressure (atm) | residence time (s) | formic acid conc. (mmol/L) | water conc. (mol/L) | formic acid conv. (%) | CO yield (%) | $CO_2$ yield (%) | $H_2$ yield (%) | carbon balance (%) |
|---|---|---|---|---|---|---|---|---|
| 178 | 1.6 | 1.5 | 5.29 | 66 | 0.7 | 60 | 48 | 94 |
| 178 | 2.5 | 1.5 | 5.29 | 64 | 0.8 | 58 | 47 | 95 |
| 178 | 4.1 | 1.5 | 5.29 | 69 | 0.9 | 60 | 44 | 92 |
| 178 | 6.5 | 1.5 | 5.29 | 74 | 1.0 | 67 | 49 | 94 |
| 178 | 11.8 | 1.5 | 5.29 | 90 | 0.8 | 80 | 58 | 91 |
| 205 | 2.1 | 2.2 | 7.27 | 67 | 0.9 | 64 | 52 | 98 |
| 205 | 3.5 | 2.2 | 7.25 | 75 | 0.8 | 72 | 59 | 99 |
| 205 | 5.6 | 2.2 | 7.26 | 88 | 0.6 | 82 | 68 | 95 |
| 205 | 9.1 | 2.2 | 7.29 | 96 | 0.4 | 89 | 69 | 94 |
| 205 | 16.4 | 2.2 | 7.24 | 100 | 0.5 | 90 | 72 | 90 |
| 219 | 2.7 | 2.7 | 9.35 | 85 | 1.0 | 80 | 65 | 96 |
| 219 | 4.6 | 2.7 | 9.37 | 92 | 0.7 | 87 | 72 | 96 |
| 219 | 7.3 | 2.7 | 9.31 | 96 | 0.5 | 91 | 76 | 95 |
| 219 | 12.0 | 2.7 | 9.29 | 99 | 0.4 | 93 | 77 | 94 |
| 219 | 17.2 | 2.7 | 9.20 | 100 | 0.3 | 90 | 68 | 90 |
| 250 | 23.2 | 10.2 | 25.6 | 92 | 1.7 | 91 | 83 | 101 |
| 250 | 28.3 | 10.1 | 25.4 | 96 | 1.9 | 95 | 85 | 100 |
| 250 | 36.2 | 10.1 | 25.3 | 99 | 1.6 | 98 | 91 | 100 |
| 250 | 46.3 | 10.1 | 25.2 | 100 | 1.2 | 99 | 95 | 100 |
| 250 | 49.7 | 10.0 | 25.1 | 100 | 1.9 | 95 | 87 | 97 |
| 250 | 63.3 | 10.0 | 25.1 | 100 | 0.9 | 92 | 81 | 93 |
| 273 | 25.5 | 8.0 | 27.8 | 99 | 1.8 | 95 | 79 | 97 |
| 273 | 29.9 | 8.1 | 27.9 | 100 | 1.2 | 95 | 78 | 96 |
| 273 | 39.9 | 8.1 | 27.8 | 100 | 0.9 | 102 | 81 | 103 |
| 273 | 55.1 | 8.1 | 27.8 | 100 | 0.4 | 92 | 75 | 93 |
| 301 | 34.1 | 8.6 | 29.6 | 100 | 1.3 | 97 | 85 | 99 |
| 302 | 44.2 | 8.6 | 29.6 | 100 | 0.8 | 96 | 83 | 97 |
| 302 | 62.0 | 8.6 | 29.6 | 100 | 0.3 | 94 | 79 | 94 |
| 303 | 80.1 | 8.6 | 29.7 | 100 | 0.0 | 86 | 59 | 86 |

The pseudo-first-order rate constant is related to the formic acid concentration by

$$k' = kC_{\text{mean}}^{n-1}$$

so a log−log plot of these pseudo-first-order rate constants as a function of the mean formic acid concentration ($C_{\text{mean}}$) in the reactor during the experiment provides the global reaction order as 1 plus the slope of the best-fit line through the data. Figure 2 provides the log−log plot of the data, and the slope of the line that best fits the data is $-0.06 \pm 0.18$. The uncertainty given here and elsewhere in this paper represents the 95% confidence interval about the reported value. Therefore, the global reaction order for formic acid decomposition under hydrothermal conditions is $0.94 \pm 0.18$. Given the uncertainty in the reaction order and its proximity to unity, we conclude that formic acid disappearance is adequately described by first-order kinetics under the conditions of the present experiments.

We can also use the results of the experiments in Figure 2 to obtain an estimate of the first-order rate constant at 360 °C. The seven experiments in Figure 2 gave rate constants that ranged from 0.10 to 0.15 $s^{-1}$, and the mean value was $0.127 \pm 0.016$ $s^{-1}$.

Having determined the reaction order and the rate constant at 360 °C, we next used the data in Tables 1 and 2 from experiments at 320, 340, 360, 380, and 420 °C to determine the first-order rate constant at each of these temperatures. Experiments at higher temperatures led to complete conversion even at the shortest residence times studied, so these high-temperature data are not useful for quantitative kinetics analysis. Linear regression of the data as $\ln(1/(1 - X))$ vs $\tau$ provided the rate constant as the slope of the line through the origin that best fit the experimental data.

Table 3, which lists these rate constants, shows that the rate constant at 250 atm increases as the temperature increases from 320 to 420 °C. Linear regression of these data as $\ln k$ vs $1/T$ (an Arrhenius plot) leads to Arrhenius parameters of $\log A$ ($s^{-1}$) = 6.2 and $E$ = 20.5 kcal/mol. This preexponential factor is lower than transition state theory (Moore and Pearson, 1981) would lead one to expect for an elementary unimolecular reaction ($\log A \cong 13 \pm 1$). This low value can perhaps be rationalized, however, if there is a significant loss of entropy as the atoms in the reactant arrange themselves to form the activated complex. We note that ab initio quantum chemical calculations showed that the activated complex for the unimolecular gas-phase decomposition of formic acid to form $CO_2$ and $H_2$ involves a four-center transition state (Ruelle et al., 1986; Melius et al., 1990; Goddard et al., 1992; Francisco, 1992), as shown in Figure 3. This transition state is certainly more "ordered" than formic acid, so $\Delta S^{\ddagger}$ should be less than zero. According to these quantum chemical calculations, however, the activation energy for this decarboxylation path should be about 65−70 kcal/mol, which is much greater than the 20.5 kcal/mol we obtained from these experiments. Thus, these experimental Arrhenius parameters for the first-order rate constant for formic acid decomposition under hydrothermal conditions differ from those expected for a unimolecular elimination reaction in the gas phase based on quantum chemical calculations.

One possible reason for these differences is that the mechanism for the hydrothermal decomposition differs from the gas-phase mechanism and that water plays a role in the reaction. Ruelle et al. (1986) and Ruelle (1987) suggested that water is a catalyst for the decarboxylation reaction. Later, Melius et al. (1990) considered the potential catalytic effect of water on both the decarboxylation and dehydration paths. Illustrations

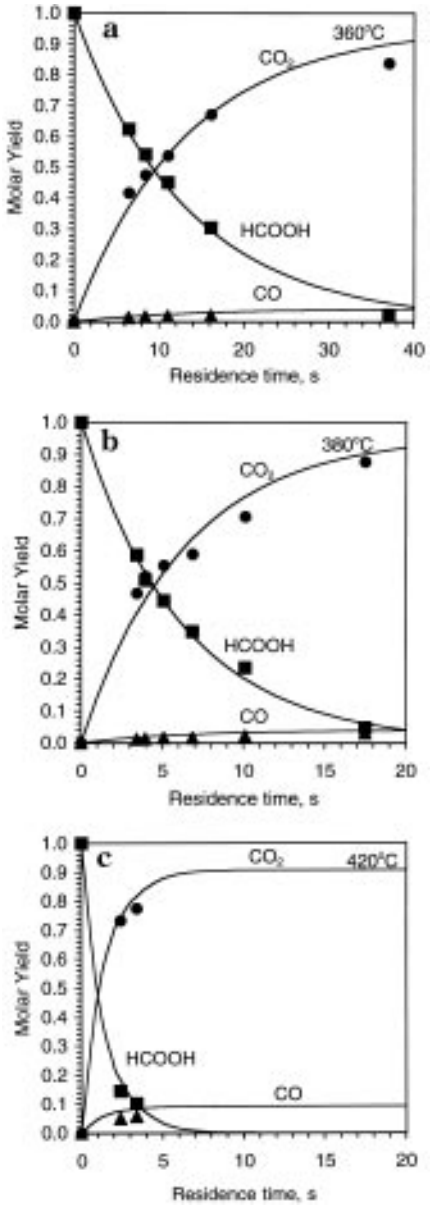


**Figure 1.** Temporal variation of product yields from formic acid decomposition at 250 atm (discrete points are experimental data; smooth curves are calculated from rate constants in Table 4): (a) 360 °C; (b) 380 °C; (c) 420 °C.

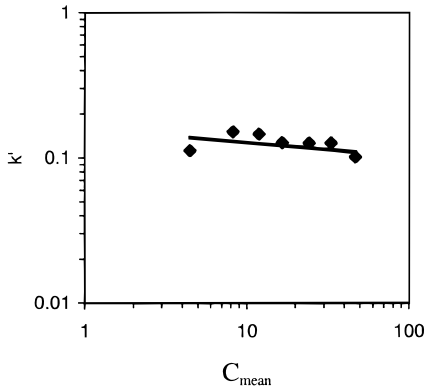


**Figure 2.** Effect of formic acid concentration on the first-order rate constant for formic acid disappearance at 360 °C and 250 atm.

of the relevant transition states for these water-catalyzed decomposition mechanisms appear in Figure 3. All of these quantum chemical calculations showed that the activation energy for a decarboxylation reaction

**Table 3. Rate Constants for Formic Acid Disappearance under Hydrothermal Conditions**

$-r_{HCOOH} = k[HCOOH]$ $\quad -r_{HCOOH} = k[HCOOH][H_2O]$

| temp (°C) | pressure (atm) | $k$ (1/s) | $k$ (L/mol·s) | 95% CI[a] (% of $k$) |
|---|---|---|---|---|
| 320 | 250 | 0.050 | 0.0013 | 26 |
| 340 | 250 | 0.098 | 0.0027 | 3 |
| 360 | 250 | 0.127[b] | 0.0038 | 13 |
| 360 | 250 | 0.097 | 0.0029 | 17 |
| 380 | 250 | 0.164 | 0.0063 | 8 |
| 420 | 250 | 0.719 | 0.096 | 24 |
| 380 | 178 | 0.216 | 0.041 | 36 |
| 380 | 205 | 0.366 | 0.050 | 13 |
| 380 | 219 | 0.430 | 0.046 | 20 |
| 380 | 250 | 0.116 | 0.0045 | 12 |
| 380 | 273 | 0.192 | 0.0069 | n.d.[c] |

[a] CI = confidence interval. [b] Determined from data in Figure 2. [c] n.d. = not determined because of insufficient data.

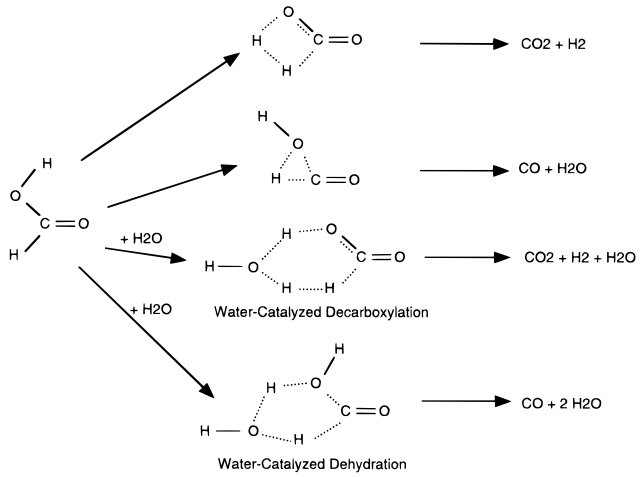


**Figure 3.** Illustration of molecular elimination mechanisms for formic acid decomposition.

that involved a water molecule in the transition state was about 20−25 kcal/mol lower than the activation energy of the competing unimolecular decomposition reactions. Therefore, we reassessed the experimental kinetics by exploring the possibility of the decomposition reaction being catalyzed by water and thereby being second order overall. The second-order rate constants, which also appear in Table 3, were calculated as the first-order rate constants divided by the water concentration (which was essentially constant) at reaction conditions. A linear regression of these second-order rate constants as ln $k$ vs $1/T$ led to Arrhenius parameters of log $A$ (L/mol·s) = 9.3 and $E$ = 33.6 kcal/mol. This experimental activation energy of 33.6 ± 17.2 kcal/mol is similar to the activation energies of 48.7 kcal/mol, 45.3 and 47.9 kcal/mol, and 21.5 and 37.3 kcal/mol that Ruelle et al. (1986), Akiya and Savage (1998), and Melius et al. (1990) obtained from ab initio quantum chemical calculations for the water-catalyzed decarboxylation reaction. Moreover, the experimental pre-exponential factor is of the same order of magnitude as one would expect for a bimolecular reaction. Note, however, the uncertainty in the individual Arrhenius parameters is high because of the strong correlation between $A$ and $E$, so one must exercise caution in assigning chemical significance to their numerical values.

To test further the effect of water on the decarboxylation reaction kinetics, we consider the sets of experi-

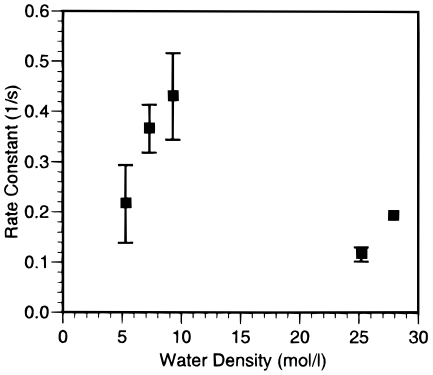


**Figure 4.** Effect of water density on first-order rate constants at 380 °C.

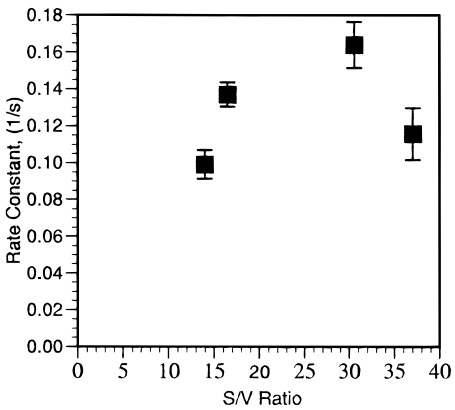


**Figure 5.** Effect of reactor surface/volume ratio on first-order rate constant at 380 °C and 250 atm.

ments conducted at a nominally constant temperature of 380 °C and at different pressures and hence different water densities. The results of these experiments appear in Table 2, the first-order rate constants at each pressure appear in Table 3, and the rate constant as a function of the water density at the reaction conditions appears in Figure 4. If the decarboxylation reaction occurs in a single elementary step that is catalyzed by a single water molecule, the kinetics of this reaction would be first order in water, which implies that a straight line through the data in Figure 4 would possess a slope of unity. The first three data points at the low water concentrations display precisely this trend, but the last two data points at the higher pressures clearly do not. The rate constant at the highest water density was calculated from a single experimental run, so it was not possible to calculate the 95% confidence interval for this rate constant. Given that the rate constant is an estimate based on a single point, however, we expect its uncertainty to exceed the uncertainties associated with the other rate constants in Figure 4.

A factor that complicates the proper discernment of the effect of pressure (or water density) on the decomposition kinetics is the possibility that the dominant decomposition mechanism might be density dependent. The calculations of Melius et al. (1990) revealed that, for the dehydration path, the unimolecular mechanism would be expected to be the fastest step at 700 K and 1 atm whereas a mechanism with one or two water molecules in the transition state would be expected to be the fastest step at 700 K and 300 atm. Even with this possible shift in mechanism as the density increases, however, one would expect the pseudo-first-order rate constant to increase with isothermal increases in the water density if the primary role of water is to catalyze the decomposition in a single elementary step. This expected monotonic increase is clearly not apparent in Figure 4.

Rice and co-workers (1996) at the Combustion Research Facility in Sandia National Laboratory have performed similar experiments to determine the effect of the water density on the kinetics of the water−gas shift reaction ($CO + H_2O = CO_2 + H_2$). Their experiments were motivated by Melius et al. (1990) proposing a formic acid intermediate for this reaction and, as noted above, predicting that high water densities would reduce the energy barriers and accelerate the reaction rate. The group at Sandia confirmed this prediction by observing that a 3-fold increase in the water density (from 9.4 to 30.8 mol/L) at 410 °C resulted in a 40-fold increase in the rate of CO disappearance. Our data in Figure 4 show, at most, a 4-fold difference in rate over roughly the same range of water densities. Integrating these two sets of data suggests that the rate of formation of formic acid from CO and $H_2O$ is slow and strongly dependent on the water density, whereas the decomposition of formic acid to $CO_2$ and $H_2$ is much faster and the decomposition kinetics are much less sensitive to the water density.

The previous reports (Bjerre and Sørensen, 1992; Brill et al., 1996) on the hydrothermal decomposition of formic acid have either identified or intimated that the reactor surface might influence the reaction kinetics. We conducted a set of experiments at identical nominal reaction conditions (380 °C, 250 atm) but with reactors with different inner diameters and therefore different surface area to volume (S/V) ratios to explore the effect of the S/V ratio on the decomposition kinetics. The results from these experiments appear in Figure 5, which displays the first-order rate constant for formic acid disappearance as a function of the S/V ratio. The two data points at the higher S/V ratios correspond to the rate constants already reported in Table 3, and the two data points at the lower S/V ratios were obtained in a reactor with a larger inner diameter of 4.8 mm. In one experiment, a smaller Hastelloy tube was placed inside the 4.8 mm i.d. reactor to give a slightly higher S/V ratio than that of the empty reactor system itself. The results in Figure 5 show that decreasing the reactor S/V ratio had very little effect on the rate constant. This observation leads us to conclude that the kinetics data derived from the experimental data in Tables 1 and 2 are largely insensitive to the reactor S/V ratio (within the range of values explored experimentally). Thus, it appears that random error and not surface-catalyzed reactions is the main contributor to the 40% difference between the rate constants obtained from different reactors at 380 °C and 250 atm as reported in Table 3.

## Reaction Network

Studies of formic acid decomposition in the gas phase (Blake and Hinshelwood, 1960; Blake et al., 1971; Saito et al., 1984; Hsu et al., 1982) showed that the main reaction was dehydration, which formed CO and $H_2O$, and that decarboxylation, which forms $CO_2$ and $H_2$, occurred to a lesser extent. The results in Tables 1 and 2, on the other hand, show that the main reaction under hydrothermal conditions is decarboxylation and that dehydration is much less important. Results from reactions both in the gas phase and in a hydrothermal

medium are consistent, however, in showing that at least two parallel paths are available for formic acid decomposition.

The discussion above suggests that the reaction network below can describe the main reaction paths for formic acid decomposition under hydrothermal conditions.

$$HCOOH \rightarrow CO_2 + H_2 \quad (1)$$

$$HCOOH \rightarrow CO + H_2O \quad (2)$$

This network includes parallel primary reactions for formic acid decomposition. The main route is reaction 1, which is the decarboxylation pathway. The minor route is reaction 2, which is the dehydration pathway.

As noted in the previous section, one possible explanation for the significant difference in the relative amounts of CO and $CO_2$ formed in the gas phase and in aqueous solution is that water enhances the rate of decarboxylation, as Ruelle et al. (1986) propose. The results of Melius et al. (1990), on the other hand, show that water is also a catalyst for the dehydration path. Their computational study showed that the inclusion of a single water molecule in the transition states for decarboxylation and dehydration reduced the respective energy barriers by roughly equal amounts. Likewise, including a second water molecule in the transition state further reduced the energy barriers, but again by roughly equal amounts. The Melius et al. calculations also showed that the energy barrier for dehydration exceeds that for decarboxylation, in both the absence and presence of water molecules. Therefore, these electronic-structure calculations do not anticipate the experimental observation that CO is the major decomposition product in the gas phase whereas $CO_2$ is the major product from formic acid decomposition under hydrothermal conditions. This observed inconsistency points out that the quantitative details of the current mechanistic understanding of formic acid decomposition are incomplete and that additional theoretical work is in order. Our efforts in this area are described by Akiya and Savage (1998).

Having proposed a reaction network, we next focus attention on obtaining quantitative estimates for the rate constants for the two parallel reaction paths for formic acid decomposition. These estimates were obtained by fitting the molar yield profiles calculated from numerical solution of the governing differential equations to the experimental data. The differential equations are

$$\frac{d}{d\tau}(MY_{HCOOH}) = -(k_1 + k_2)MY_{HCOOH}$$

$$\frac{d}{d\tau}(MY_{CO_2}) = k_1 MY_{HCOOH}$$

$$\frac{d}{d\tau}(MY_{CO}) = k_2 MY_{HCOOH}$$

where $\tau$ is the residence time in the plug-flow reactor and $MY_i$ is the molar yield of compound $i$. These equations were solved numerically using Euler's method. The objective function that was minimized during the parameter estimation was the sum of the squared differences between the calculated and experimental molar yields of formic acid, CO, and $CO_2$. This simultaneous differential equation solution and parameter estimation was performed by using the Solver option in a Microsoft Excel spreadsheet. Table 4 displays the estimated first-order rate constants, and Figure 1 compares the calculated and experimental temporal variations of the products' molar yields. It is clear that the use of first-order kinetics for each of the parallel primary paths provides a good quantitative description of these experimental data. The rate constants in Table 4 differ from those in Table 3 because different objective functions were employed in the parameter estimation. The rate constants in Table 3 were calculated by using only the formic acid disappearance data. The rate constants in Table 4, on the other hand, were calculated by using the data for formic acid, CO, and $CO_2$.

**Table 4. First-Order Rate Constants for a Formic Acid Reaction Network**

| temp (°C) | pressure (atm) | $k_1$ (1/s) | $k_2$ (1/s) |
|---|---|---|---|
| 320 | 250 | 0.053 | 0.004 |
| 340 | 250 | 0.093 | 0.004 |
| 360 | 250 | 0.070 | 0.003 |
| 380 | 250 | 0.143 | 0.006 |
| 420 | 250 | 0.470 | 0.048 |
| 380 | 178 | 0.296 | 0.029 |
| 380 | 205 | 0.352 | 0.016 |
| 380 | 219 | 0.459 | 0.018 |
| 380 | 250 | 0.107 | 0.002 |

## Mechanisms

The literature describes several different mechanisms for formic acid decomposition that can potentially occur under the hydrothermal conditions used in the present experiments. As previously discussed, molecular elimination is generally regarded as the most important mechanism for formic acid decomposition in the gas phase (Goddard et al., 1992; Francisco, 1992) and in the presence of water (Ruelle et al., 1986; Melius et al., 1990). Our experimental observations regarding the effect of the water density on the decomposition kinetics and regarding the relative amounts of CO and $CO_2$ produced, however, are not fully consistent with the quantitative details of the molecular mechanisms proposed in the literature. This inconsistency suggests that either the current concept of the molecular mechanisms is incomplete or some other mechanism might be operative under the hydrothermal conditions of our experiments. Alternative mechanisms include free-radical, ionic, and surface-catalyzed reactions. Each of these mechanistic possibilities is described and discussed in this section.

**Free-Radical Reaction.** Decomposition of formic acid via free-radical reactions is a possible mechanism under the conditions of our experiments. For example, a reactive COOH radical (or more commonly HOCO) can be formed by removing the hydrogen atom from the C−H bond in formic acid. This formyl C−H bond is weaker than the O−H bond (Singleton et al., 1988). This bond cleavage process could occur through homolytic dissociation or by hydrogen abstraction. The COOH radical can then decompose to form either $CO_2$ or CO. The set of reactions is as follows.

$$HCOOH = H + COOH$$

$$COOH = H + CO_2$$

$$COOH = OH + CO$$

The H and OH radicals formed in the latter two steps can attack formic acid, abstract hydrogen, and thereby possibly generate additional COOH radicals. Thus, the opportunity might exist for a free-radical chain reaction. Gorden and Ausloos (1961) found it necessary to invoke free-radical chain reactions to explain fully results from the vapor-phase photolysis of formic acid above 200 °C.

The reaction of OH with formic acid has been studied (Singleton et al., 1988; Wine et al., 1985; Jolly et al., 1986), but only near ambient temperature and pressure, which is the region of interest in atmospheric chemistry. Under these conditions, the reaction is complex, and the mechanism has not been established unambiguously. It does appear clear though that OH prefers to attack the O−H bond in formic acid rather than the weaker formyl C−H bond under atmospheric chemistry conditions. At higher temperatures, however, abstraction from the formyl group is expected to make a larger contribution to the overall reaction (Singleton et al., 1988). Nevertheless, a free-radical chain with OH as the chain carrier does not appear to be likely. A chain with H as the chain carrier remains a possibility.

Although a free-radical chain appears to be feasible for formic acid decomposition, it does not appear to be the prevalent mechanism. There is both experimental and computational evidence against a free-radical mechanism being important. Blake and Hinshelwood (1960) found that the addition of propylene and isobutene, which are good free-radical scavengers, had no effect on the rate of formic acid decomposition in the gas phase at temperatures around 500 °C. Hsu et al. (1982) considered the possibility of a radical process for the gas-phase decomposition of formic acid in a shock tube but ruled it out because the kinetics it predicted were not consistent with all of their experimental data. Finally, Goddard et al. (1992) and Francisco (1992) compared the energetics of the molecular mechanisms and the competing free-radical initiation steps and concluded that neither dehydration nor decarboxylation involve free-radical chains.

**Ionic Reaction.** Because some of the hydrothermal conditions used in the present experiments can support the formation of ions, it is possible that ionic reactions occur during the decomposition of formic acid. For example, formic acid can dissociate according to

$$HCOOH = HCOO^- + H^+$$

and then subsequent decomposition of the anion could produce $CO_2$. Maiella and Brill (1996) included this type of ionic decomposition mechanism in their analysis of malonic acid decomposition under hydrothermal conditions. They found that only a small amount of the malonate anion was produced (less than 1% yield) and that the rate constant for production of $CO_2$ from the anion was about 30% lower than the rate constant for production of $CO_2$ directly from malonic acid. If these results are generally true for other carboxylic acids, one would expect the contribution of ionic reactions to the overall hydrothermal decomposition kinetics of organic acids to be small.

**Surface-Catalyzed Reaction.** One final potential mechanism that we consider for the decomposition of formic acid under hydrothermal conditions involves surface-catalyzed reactions. There have been numerous studies of formic acid decomposition on the surfaces of well-characterized single crystals at very low pressures, and it is clear that surfaces promote the decomposition. Moreover, surface effects have also been observed or implicated under hydrothermal conditions. For example, Bjerre and Sørensen (1992) obtained different results from formic acid decomposition experiments at 260 °C in new and used reactors. The used reactor led to a higher formic acid conversion, higher yields of $CO_2$ and $H_2$, and a lower yield of CO. They attributed the difference to the older reactor surface being rough and corroded. Brill et al. (1996) noted that the temporal variation of the $CO_2$ profile from formic acid decomposition under hydrothermal conditions was strikingly similar to that observed from decomposition on a Ni(110) surface under ultrahigh-vacuum conditions (Falconer and Madix, 1974). Of course, one must recognize that the reaction conditions are very different in these two studies. One involved pressures of $10^{-7}$ Torr, whereas the other involved 275 bar.

As noted in a previous section, our experimental results do not show the same behavior as the data reported by Brill et al. (1996). Rather, our data exhibit temporal variations that are consistent with a first-order rate expression, which could describe a homogeneous fluid-phase reaction. Moreover, we did not observe any significant changes in the decomposition kinetics as the reactor S/V ratio was varied.

To summarize this discussion of mechanistic issues and review of the literature, we find that formic acid decomposition under hydrothermal conditions probably proceeds through molecular reaction steps, with the reactions possibly being water catalyzed. Free-radical, ionic, and surface-catalyzed reactions are not expected to be as significant. In closing, we note that the quantitative details of the mechanism for the gas-phase decomposition of formic acid have not yet been fully resolved, so these suggestions regarding the hydrothermal decomposition mechanisms necessarily remain speculative. It is clear that additional experimental work is warranted to resolve issues such as the role of water and metal surfaces in the decomposition reaction.

## Summary and Conclusions

Formic acid decomposition under hydrothermal conditions leads to high yields of $CO_2$ and $H_2$. The rates of formic acid disappearance and product formation at temperatures above 320 °C are consistent with first-order kinetics. Experiments were conducted to probe the effect of the water density on the decomposition kinetics at 380 °C, but no monotonic trend was apparent. A comparison of the present experimental results with the results one would expect based on the molecular decomposition mechanisms in the literature revealed some inconsistencies in the effect of density on the rate and in the selectivities to CO and $CO_2$. These inconsistencies lead us to conclude that either physical phenomena are confounding the chemical mechanisms or the quantitative details regarding the mechanism of formic acid decomposition in the presence of water and under hydrothermal conditions have not been fully resolved. Thus, the physical and chemical behavior of this simple organic acid under hydrothermal conditions is both interesting and complex. Additional experimental and computational research that determines the effect of the water density on the kinetics and product yields and that distinguishes between the effects of homogeneous and heterogeneous reactions is warranted.

## Acknowledgment

This work was supported, in part, by the National Science Foundation (CTS-9521698, CTS-9311300).

## Literature Cited

Akiya, N.; Savage, P. E. The Role of Water in Formic Acid Decomposition. *AIChE J.* **1998** (accepted).

Bjerre, A. B.; Sørensen, E. Thermal Decomposition of Dilute Aqueous Formic Acid Solutions. *Ind. Eng. Chem. Res.* **1992**, *31*, 1574−1577.

Blake, P. G.; Hinshelwood, C. The Homogeneous Decomposition Reactions of Gaseous Formic Acid. *Proc. R. Soc. London, A* **1960**, *255*, 444−455.

Blake, P. G.; Davies, H. H.; Jackson, G. E. Dehydration Mechanisms in the Thermal Decomposition of Gaseous Formic Acid. *J. Chem. Soc. B* **1971**, 1923−1925.

Brill, T. B.; Schoppelrei, J. W.; Maiella, P. G.; Belsky, A. Spectrokinetics of Solvo-Thermal Reactions. *Proc. 2nd Int. Conf. Solvotherm. Reactions*, **1996**, 5−8.

Copa, W. M.; Gitchel, W. B. in *Standard Handbook of Hazardous Waste Treatment and Disposal*; Freeman, H. M., Ed.; McGraw-Hill: New York, 1989; pp 8.77−8.90.

Falconer, J. L.; Madix, R. J. The Kinetics and Mechanism of the Autocatalytic Decomposition of HCOOH on Clean Ni(110). *Surf. Sci.* **1974**, *46*, 473−504.

Francisco, J. S. A Comprehensive Theoretical Examination of Primary Dissociation Pathways of Formic Acid. *J. Chem. Phys.* **1992**, *96*, 1167−1175.

Goddard, J. D.; Yamaguchi, Y.; Schaefer, H. F. The Decarboxylation and Dehydration Reactions of Monomeric Formic Acid. *J. Chem. Phys.* **1992**, *96*, 1158−1166.

Gorden, R.; Ausloos, P. Vapor-Phase Photolysis of Formic Acid. *J. Phys. Chem.* **1961**, *65*, 1033−1037.

Holgate, H. R.; Webley, P. A.; Tester, J. W.; Helling, R. K. Carbon Monoxide Oxidation in Supercritical Water: The Effects of Heat Transfer and the Water−Gas Shift Reaction on Observed Kinetics. *Energy Fuels* **1992**, *6*, 586−597.

Hsu, D. S. Y.; Shaub, W. M.; Blackburn, M.; Lin, M. C. Thermal Decomposition of Formic Acid at High Temperatures in Shock Waves. *Proc. 19th Int. Symp. Combust.* **1982**, 89−96.

Jolly, G. S.; McKenney, D. J.; Singleton, D. L.; Paraskevopoulos, G.; Bossard, A. R. Rate Constant and Mechanism for the Reaction of Hydroxyl Radical with Formic Acid. *J. Phys. Chem.* **1986**, *90*, 6557−6562.

Katritzky, A. R.; Allin, S. M.; Siskin, M. Aquathermolysis: Reactions of Organic Compounds with Superheated Water. *Acc. Chem. Res.* **1996**, *29*, 399−406.

Maiella, P. G.; Brill, T. B. Spectroscopy of Hydrothermal Reactions. 5. Decarboxylation and Kinetics of Malonic Acid and Monosodium Malonate. *J. Phys. Chem.* **1996**, *100*, 14352−14355.

Melius, C. F.; Bergan, N. E.; Shepherd, J. E. Effects of Water on Combustion Kinetics at High Pressure. *Proc. 23rd Int. Symp. Combust.* **1990**, 217−223.

Mishra, V. S.; Mahajuni, V. V.; Joshi, J. B. Wet Air Oxidation. *Ind. Eng. Chem. Res.* **1995**, *34*, 2−48.

Moore, J. W.; Pearson, R. G. *Kinetics and Mechanism*, 3rd ed.; John Wiley & Sons: New York, 1981.

Rice, S. F. Kinetics of Supercritical Water Oxidation. Sandia National Laboratories Combustion Research Facility Quarterly Report (Case 8610.000) for July 1−Sept 30, 1996.

Ruelle, P. Ab Initio Study of the Unimolecular Pyrolysis Mechanisms of Formic Acid: Additional Comments Based on Refined Calculations. *J. Am. Chem. Soc.* **1987**, *109*, 1722−1725.

Ruelle, P.; Kesselring, U. W.; Nam-Tran, H. Ab Initio Quantum-Chemical Study of the Unimolecular Pyrolysis Mechanisms of Formic Acid. *J. Am. Chem. Soc.* **1986**, *108*, 371−375.

Saito, K.; Kakumoto, T.; Kuroda, H.; Torii, S.; Imamura, A. Thermal Unimolecular Decomposition of Formic Acid. *J. Chem. Phys.* **1984**, *80*, 4989−4996.

Savage, P. E.; Gopalan, S.; Mizan, T. I.; Martino, C. J.; Brock, E. E. Reactions at Supercritical Conditions: Fundamentals and Applications. *AIChE J.* **1995**, *41*, 1723−1778.

Singleton, D. L.; Paraskevopoulos, G.; Irwin, R. S.; Jolly, G. S.; McKenney, D. J. Rate and Mechanism of the Reaction of Hydroxyl Radicals with Formic and Deuteriated Formic Acids. *J. Am. Chem. Soc.* **1988**, *110*, 7786−7790.

Thornton, T. D.; Savage, P. E. Phenol Oxidation in Supercritical Water. *J. Supercrit. Fluids* **1990**, *3*, 240−248.

Wightman, T. J. M.S. Thesis, University of California, Berkeley, CA, 1981.

Wine, P. H.; Astalos, R. J.; Mauldin, R. L. Kinetics and Mechanistic Study of the OH + HCOOH Reaction. *J. Phys. Chem.* **1985**, *89*, 2620−2624.

*Received for review* February 28, 1997
*Revised manuscript received* October 14, 1997
*Accepted* October 16, 1997[⊗]

IE970182E

[⊗] Abstract published in *Advance ACS Abstracts*, December 1, 1997.